DESIGN OF CMOS TRANSCEIVER FOR MICRO-NMR SPECTROMETER

A DISSERTATION

SUBMITTED TO THE FACULTY OF THE GRADUATE SCHOOL

OF THE UNIVERSITY OF MINNESOTA

BY

JAEHYUP KIM

IN PARTIAL FULFILLMENT OF THE REQUIREMENTS

FOR THE DEGREE OF

DOCTOR OF PHILOSOPHY

RAMESH HARJANI, ADVISOR

July 2012

Acknowledgments

To begin with, I would like to give my sincere thank to my advisor, Professor Ramesh Harjani, for giving me the chance to work with him and not hesitating the countless number of discussions that helped to complete my Ph.D. Additionally, he and his wife, Savita Harjani, have been with me as great friends and parents for the past five years. My Ph.D would not have been possible without his incredible technical guidance and inspiration.

I am also grateful to Professor Anand Gopinath, Sanghyun Oh and Bruce Hammer for reviewing my thesis manuscript and serving on my final defense committee. Furthermore, I would like to acknowledge Phil Williams in Professor Hammer's Lab for helping me NMR tests to prepare several conferences.

The members of Harjani's Analog Group have made my Ph.D. experience fun and stimulating. I look forward to working in the lab everyday because of the people in this group. I am especially indebted to Martin Sturm for assisting me on my tape-outs and testing. He is always patient and collaborated with me on all my research endeavors. I would not have finished my Ph.D. without his help. I am also grateful to Bodhisatwa Sadhu, Taehyoun Oh, Sudhir Kudva, Mohammad Elbadry, Sriharsha Vadlamani, Ashutosh Mehra, Sachin Kalia, Mustafijur Rahman and lab alumni (Narasimha Lanka, Satwik Patnaik, and Kin-Joe Sham), who have all made suggestions regarding my work and assisted me in designing and laying out my chips.

My deepest gratitude to my friends from near and far for their unequivocal support

and understanding. In particular, ECE Korean community have all taken the time out of their lives to enjoy with me during my Ph.D. and given me inspiration to complete my research in a timely manner.

Finally, I must thank my wife, Soohyun Ryoo and my daughter, Danna Seohyung Kim as well as my parents supporting. They were also the ones who encouraged me to study for my Ph.D. Without my family, I would not be where I am today.

Abstract

Previously, the primary challenging issues in nuclear magnetic resonance (NMR) spectroscopy and magnetic resonance imaging (MRI) have been building coils with high quality factor (Q), or getting a strong magnetic field from the static magnet to increase the signal to noise ratio (SNR). Current techniques have enabled the development of palm-size to room-size of high-strength magnets magnetic field as well as high Q NMR coils. However, there still remains a strong effort to scale down NMR and MRI systems because RF transceivers built with discrete components leave the entire NMR system bulky. With the aid of modern RF CMOS technology, it is possible to integrate all RF blocks into one chip and significantly reduce the size of current NMR system.

In this thesis, we will verify that miniaturization is possible with CMOS technologies and allows for the design of compact portable medical and chemical systems, and even implantable bio-sensors. To acquire NMR spectra from small objects, we will take advantage of the proximity between the sample and the sensor coil to make the system simpler. Three different chips were developed to show the possibilities of micro-NMR systems. In the first chip, a simple one-channel receiver was designed for sensing the ^{31}P spectrum (around 86 MHz) from an adenosine triphosphate (ATP) sample at 5T. It uses a LNA-mixer hybrid circuit and a ring-type based frequency synthesizer with low power consumption. To do signal processing efficiently, a simple 2^{nd} order $\Sigma\Delta$ analog-to-digital converter (ADC) for I and Q channels was added in the second chip. Like the first chip, we verified our design with the ATP sample. Based on experience gained from the first

two designs, we extended the circuit and built an entire NMR transceiver to sense diverse NMR chemicals with a variety of frequencies. In the third chip. We designed a 5-300MHz multi-nuclei NMR transceiver designed with spectroscopy for drug discovery in mind. It includes a LNA, Mixer, VGA, fractional-N PLL, ADC and transmitter PA. Through these works, we will show the feasibility of micro NMR and MRI systems with low power and low cost CMOS integrated RF transceivers.

Contents

List of Tables

List of Figures

Chapter 1

Introduction

Nuclear magnetic resonance (NMR) is a powerful tool used in NMR spectroscopy and magnetic resonance imaging (MRI). Its applications have been bounded to chemistry and medicine for a long time but recently is being extended to other fields .

NMR is a physical phenomenon in which magnetic nuclei in a magnetic field absorb and re-emit electromagnetic radiation. It simply means the electromagnetic energy exchange between RF magnetic field and the atomic nucleus. This energy comes out at a specific resonance frequency (called the Larmor frequency) which depends on the magnetic field strength and the magnetic properties (called gyro-magnetic ratio) of the isotope of the atoms. With the received energy level, we can analyze the spectrum or construct a 2-dimensional or 3-dimensional image using the . In this thesis, NMR spectroscopy is the main focus of the research.

Nuclear magnetic resonance spectroscopy, commonly known as NMR spectroscopy,

is a research technique that uses the magnetic properties of certain atomic nuclei to determine physical and chemical properties of atoms or the molecules in which they are contained. The phenomenon of nuclear magnetic resonance can provide detailed information about the structure, dynamics, reaction state, and chemical environment of molecules.

Most frequently, NMR spectroscopy is used by chemists and biochemists to investigate the properties of organic molecules, though it is applicable to any sample that contains nuclei possessing spin. Suitable samples range from small compounds analyzed with 1-dimensional proton or carbon-13 NMR spectroscopy to large proteins or nucleic acids using 3 or 4-dimensional techniques. The impact of NMR spectroscopy on the sciences has been substantial because of the range of information and the diversity of samples, including solutions and solids that can be accessed.

For spectroscopy applications, it is common to find large magnetization setups, typically of the super-conducting type, which are able to create up to 10-20T to analyze the NMR spectrum of small objects. Such approaches are clearly impractical and costly for any portable applications even though SNR is proportional to the strength of the magnetic field. For a portable NMR system, it is more appropriate to use small-scale permanent rare-earth magnets which can produce up to 1.5T peak magnetic field. Their successful implementation has been previously reported for NMR spectroscopy and surface MR tomography applications [2, 3]

In Chapter 2, we will study NMR fundamentals needed to design a NMR system.

Based on this basics, some critical considerations will discussed in Chapter 3. Circuits used to build NMR receivers (1^{st} and 2^{nd} chips) and NMR transceiver (3^{rd} chip) and the design methodology will be explained individually in Chapter 4. Some measurement results with chemical samples will be shown in Chapter 5. Final conclusions and future directions will be described in Chapter 6.

Chapter 2

Fundamentals of NMR

2.1 Nuclear Magnetic Resonance (NMR)

In this chapter, we will discuss the fundamentals of NMR. In modern chemistry and medical fields, technologies using nuclear magnetic resonance (NMR) spectroscopy and magnetic resonance imaging (MRI) are powerful and indispensable tools for acquiring valuable information from unknown objects, and diagnosing the disease of patients and for non-invasive monitoring. Both NMR and MRI are based on the magnetic resonance of nuclei within a magnetic field. To understand magnetic resonance, the concept of spin should be discussed first. Imagine a spinning charged particle. This spinning induces an electro-magnetic field as shown in Fig. 2.1 (a). This particle can be considered as a bar magnet as shown in Fig. 2.1 (b). As an example, the spinning hydrogen nucleus (also called as the proton ^{1}H) is shown because it is broadly exploited in both NMR and MRI applications.

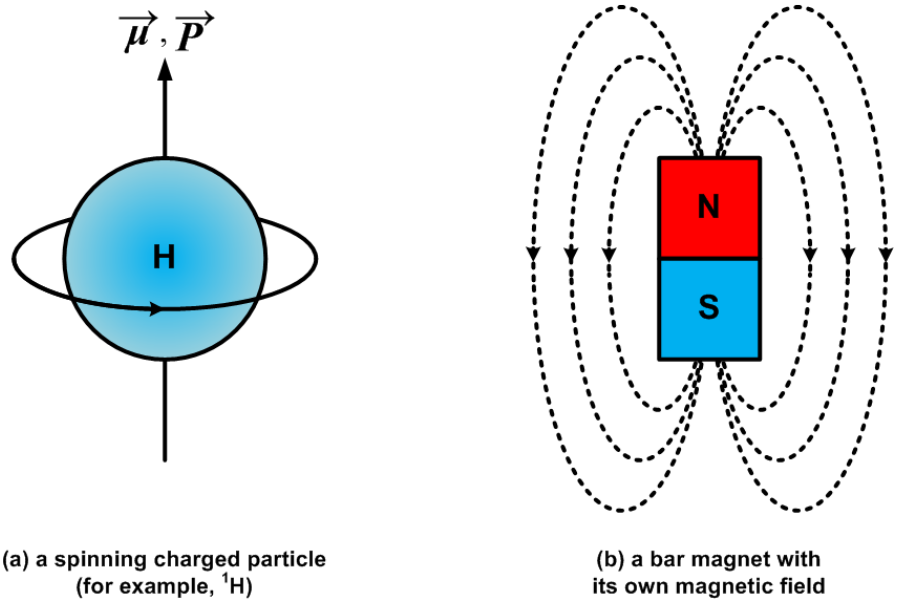

Figure 2.1: Similarity between a spinning charged particle and a bar magnet

Like the proton, nuclei with an odd atomic weight and/or an odd atomic number can have an intrinsic quantum mechanical property called "spin". This spin property can be viewed as a nucleus spinning around its own axis with a magnetic momentum ($\overrightarrow{\mu}$) and an angular momentum ($\overrightarrow{P}$). Each nucleus has some specific energy levels according to the spin quantum number (I). For instance, a proton (^{1}H) has a spin quantum number (I) of 1/2. The number of energy states a proton can have is determined by the following equation.

$$N_{energy\ states} = 2 \cdot I + 1 \tag{2.1}$$

Therefore, a proton can have two energy states: a $+1/2$, or a $-1/2$ energy state as shown in Fig. 2.2. This means that each proton can have a spin about its own axis with different energy states. In free space (when the external magnetic field B_0 is 0), the vectors of

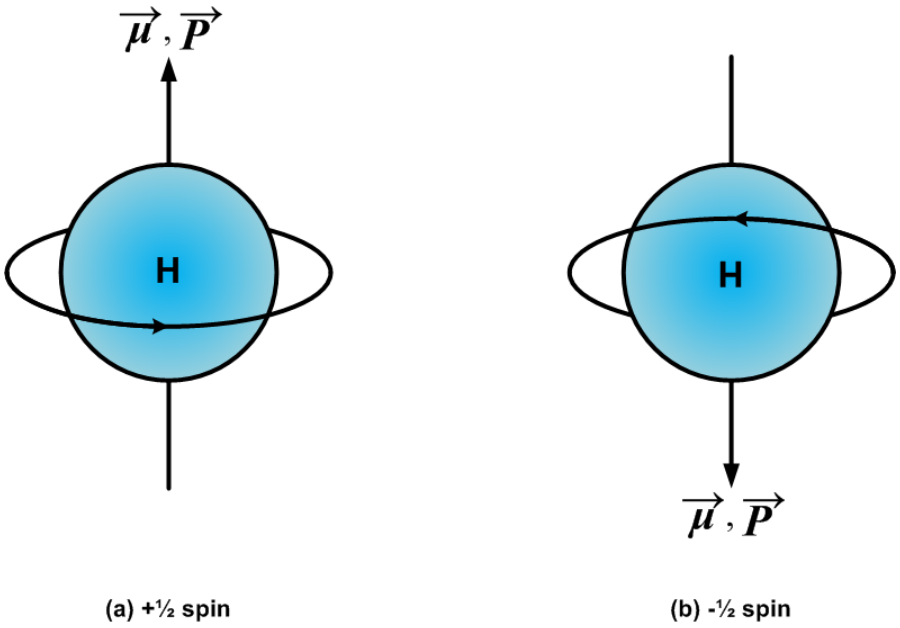

Figure 2.2: Conceptual direction for magnetic momentum of spins

all protons in the sample are randomly distributed, as in Fig. 2.3 (a). The total net magnetization ($\overrightarrow{M} = (M_x, M_y, M_z)$) of the protons is zero. The total magnetization (M) is defined as,

$$\overrightarrow{M} = \sum_{n=1}^{N_s} \overrightarrow{\mu}_n \tag{2.2}$$

$$\overrightarrow{M_x} = \sum_{n=1}^{N_s} \overrightarrow{\mu_x}_{,n} \tag{2.3}$$

$$\overrightarrow{M_y} = \sum_{n=1}^{N_s} \overrightarrow{\mu_y}_{,n} \tag{2.4}$$

$$\overrightarrow{M_x} = \sum_{n=1}^{N_s} \overrightarrow{\mu_z}_{,n} \tag{2.5}$$

where μ is the magnetic momentum of each proton and N_s is the total number of protons in the sample. When the external magnetic field ($B_0 \neq 0$) is applied to the sample in

Fig. 2.3 (b), all the protons are rearranged with the direction of B_0. There is no energy difference between $-1/2$ spin and $+1/2$ spin at $B_0 = 0$ since the same number of protons have $-1/2$ spin and $+1/2$ spin. The energy difference between two spins is proportional to the strength of B_0 and the number of the protons between each spin is not equal under a magnetic field of increasing strength as shown in Fig. 2.4. The proton having an magnetic momentum parallel with B_0 has lower energy states and the proton having an magnetic momentum anti-parallel with B_0 has a higher energy state. The number of protons having the higher state energy gets smaller as the external magnetic field strengthens.

Now we will look at the energy levels and the total magnetization in detail. According to [4], when a proton is in a magnetic field, the angular and magnetic momentum ($\overrightarrow{\mu}$, $\overrightarrow{P}$) are aligned with a special angle of 54.7° (called a magic angle) to the axis of B_0 in Fig. 2.5. This field, B_0, tries to make the magnetic momentum of a proton parallel or anti-parallel with B_0 on its own axis, in the process generating a torque ($\overrightarrow{C}$)

$$\overrightarrow{C} = \overrightarrow{\mu} \times \overrightarrow{B_0} \tag{2.6}$$

$$= \mid \mu \mid \cdot \mid B_0 \mid \cdot \sin\theta \tag{2.7}$$

Due to this torque, a proton precesses around the axis of B_0, staying at the magic angle relative to B_0. Most NMR books equates this process to a spinning gyroscope. To calculate the precession frequency of a proton in B_0, use the above torque defined as the time rate of change of the angular momentum ($\overrightarrow{P}$)

$$\overrightarrow{C} = \frac{d\overrightarrow{P}}{dt} = \overrightarrow{\mu} \times \overrightarrow{B_0} \tag{2.8}$$

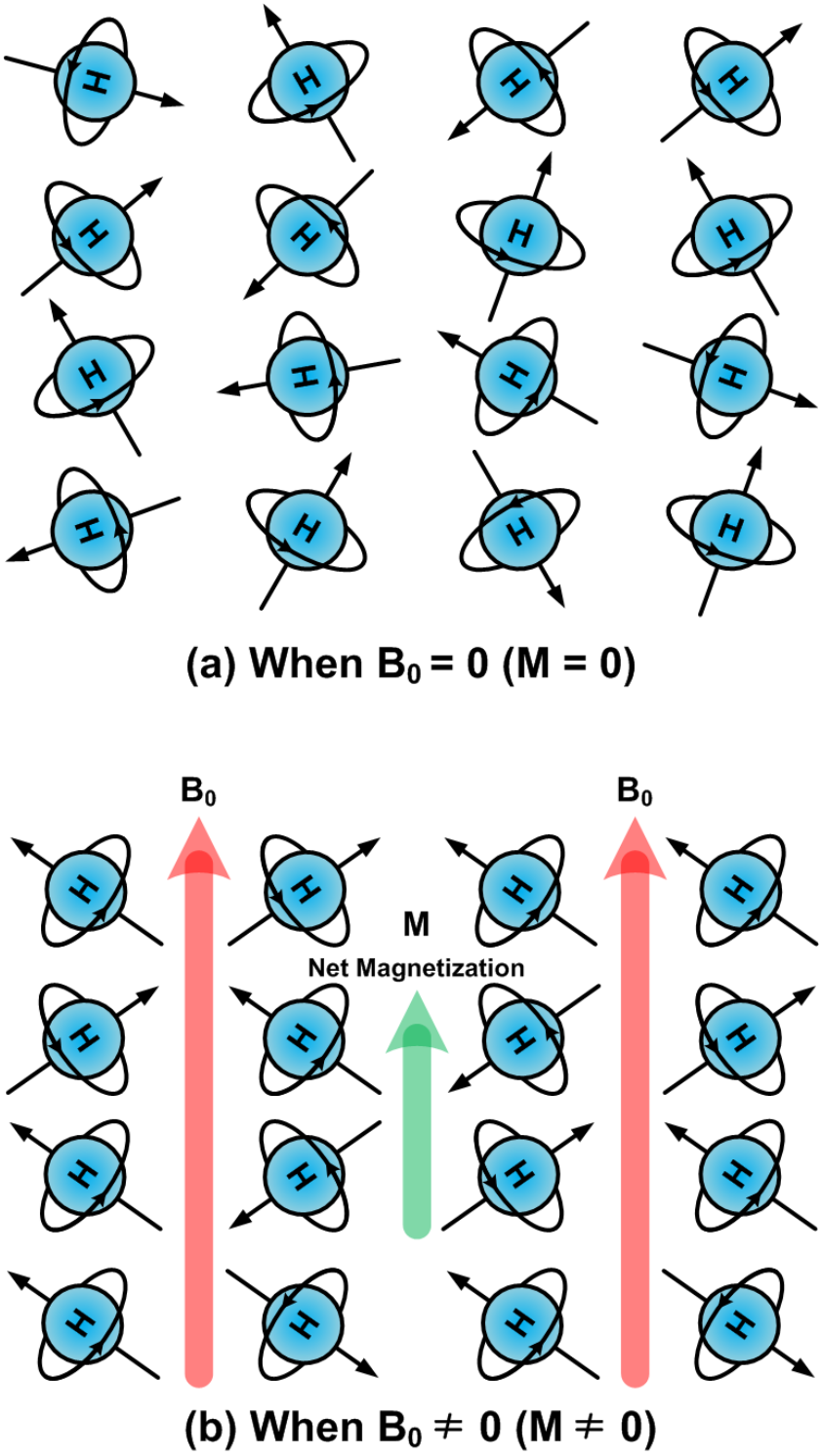

Figure 2.3: Total net magnetization for external magnetic fields (B_0)

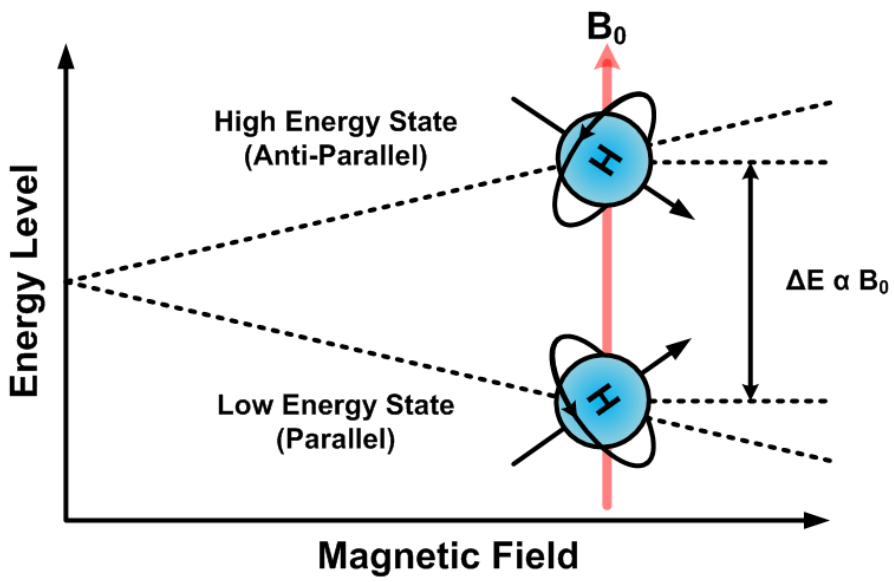

(a) Energy difference vs B_0

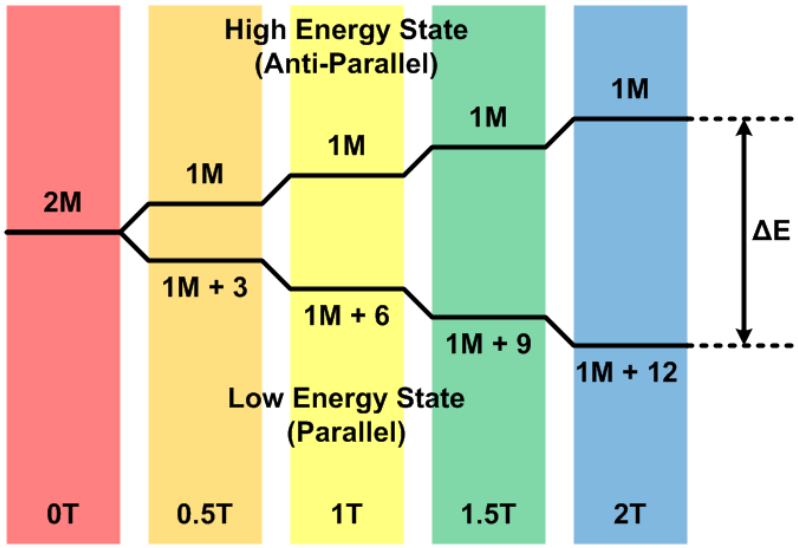

(b) Population difference vs B_0

Figure 2.4: Spin energy level (a) and population difference (b) for external magnetic fields (B_0)

During a time interval dt, the magnetic momentum precesses up to the angle $d\phi$ producing a change $d\overrightarrow{P}$ in the angular magnetic momentum. We derive this relationship.

$$\sin d\phi = \frac{d\overrightarrow{P}}{\mid P \mid \cdot \sin\theta} = \frac{\overrightarrow{C}\, dt}{\mid P \mid \cdot \sin\theta} \tag{2.9}$$

We can assume $\sin(x) \sim x$ when x is very small. Therefore, we can derive the precession frequency (ω) as

$$\omega = \frac{d\phi}{dt} = \frac{\overrightarrow{C}}{\mid P \mid \cdot \sin\theta} \tag{2.10}$$

$$= \frac{\overrightarrow{\mu} \times \overrightarrow{B_0}}{\mid P \mid \cdot \sin\theta} \tag{2.11}$$

$$= \frac{\gamma \overrightarrow{P} \times \overrightarrow{B_0}}{\mid P \mid \cdot \sin\theta} \tag{2.12}$$

$$= \frac{\gamma \mid P \mid \cdot \mid B_0 \mid \cdot \sin\theta}{\mid P \mid \cdot \sin\theta} \tag{2.13}$$

$$= \gamma \mid B_0 \mid \tag{2.14}$$

where the relation between $\overrightarrow{\mu}$ and $\overrightarrow{P}$ is

$$\overrightarrow{\mu} = \gamma \overrightarrow{P} \tag{2.15}$$

$$\mid P \mid = \frac{h}{2\pi} \left[I(I+1)\right]^{\frac{1}{2}} \tag{2.16}$$

The term γ is the gyro-magnetic ratio of the nucleus and is a distinct value for different nuclei such as proton, phosphorus and carbon. I is the quantum spin number. The final precession frequency is given by $\gamma \cdot B_0$. It is called the Larmor frequency. The Larmor frequency is linearly proportional to the external magnetic field (B_0). Because all protons are aligned with the axis of B_0 when a sample is in B_0 having a direction

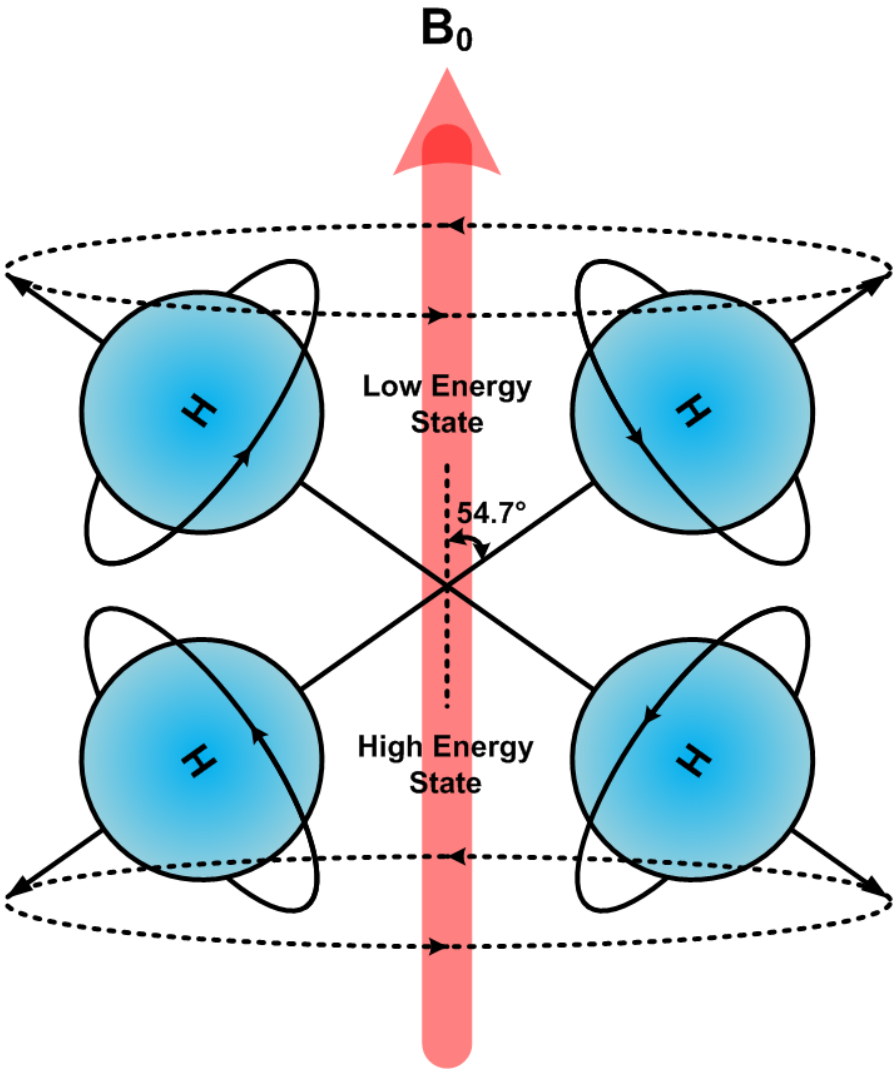

Figure 2.5: Precession for higher and lower enersgy states

defined as the z-axis, M_x and M_y components of total magnetization (M) are canceled out and only M_z has a value. The magnetic momentum (μ_z) of a proton is given by

$$| \mu | = \frac{\gamma h \sqrt{3}}{4\pi} \qquad \text{when } I = 1/2 \tag{2.17}$$

$$\mu_z = \frac{\gamma h}{4\pi} \tag{2.18}$$

At B_0, the energy level of a proton with different spin is

$$E = -\mu_z B_0 \tag{2.19}$$

$$= \mp \frac{\gamma h B_0}{4\pi} \tag{2.20}$$

Then, the energy difference between the two energy states ($+1/2$ and $-1/2$ spin) is

$$\Delta E = \frac{\gamma h B_0}{2\pi} \tag{2.21}$$

As the number of protons in the two states is determined by the Boltzmann equation, the ratio of the number of protons between two energy states is given by

$$\frac{N_{anti-parallel}}{N_{parallel}} = \exp\left(-\frac{\Delta E}{kT}\right) = \exp\left(-\frac{\gamma h B_0}{2\pi k T}\right) \tag{2.22}$$

where k is the Boltzmann constant and T is the absolute temperature (Kelvin). According to Fig. 2.4, the anti-parallel state has a higher energy than the parallel state. Using the first order approximation,

$$\exp(-x) \simeq 1 - x \quad \text{if x} \ll 1 \tag{2.23}$$

$$\frac{N_{anti-parallel}}{N_{parallel}} \simeq 1 - \frac{\gamma h B_0}{2\pi k T} \tag{2.24}$$

The difference of the number of protons between two energy states is

$$N_{parallel} - N_{anti-parallel} = N_s \frac{\gamma h B_0}{4\pi kT} \tag{2.25}$$

$$N_s = N_{parallel} + N_{anti-parallel} \tag{2.26}$$

where N_s is the total number of protons in the unit volume. We revisit the total net magnetization (M) of protons at B_0 of Equation (2.2),

$$\overrightarrow{M} = \sum_{n=1}^{N_s} \overrightarrow{\mu}_n \tag{2.27}$$

$$= \sum_{n=1}^{N_s} \overrightarrow{\mu_{z,n}} \tag{2.28}$$

$$= \frac{\gamma h}{4\pi} \left(N_{parallel} - N_{anti-parallel} \right) \tag{2.29}$$

$$= \frac{\gamma^2 h^2 B_0 N_s}{16\pi^2 kT} \tag{2.30}$$

As seen in Equation (2.30), we have now calculated the total net magnetization of protons in the sample. This value is important to estimate the NMR signal level and it will be revisited later.

Next to consider is how to obtain the NMR signal from the sample. When the total net magnetization of protons is aligned with the magnetic field (B_0) in Fig. 2.6 (1), there is no emitted NMR signal to detect. So, an RF signal with the same Larmor frequency must be applied to excite the total net magnetization (M) of the sample through an RF coil which is perpendicular to the axis of B_0 (in other words, this RF coil generates a new B_1 magnetic field orthogonal to B_0). By observing the energy from the coil, total net magnetization (M) starts to flip over the transverse plane (x-y). As illustrated in

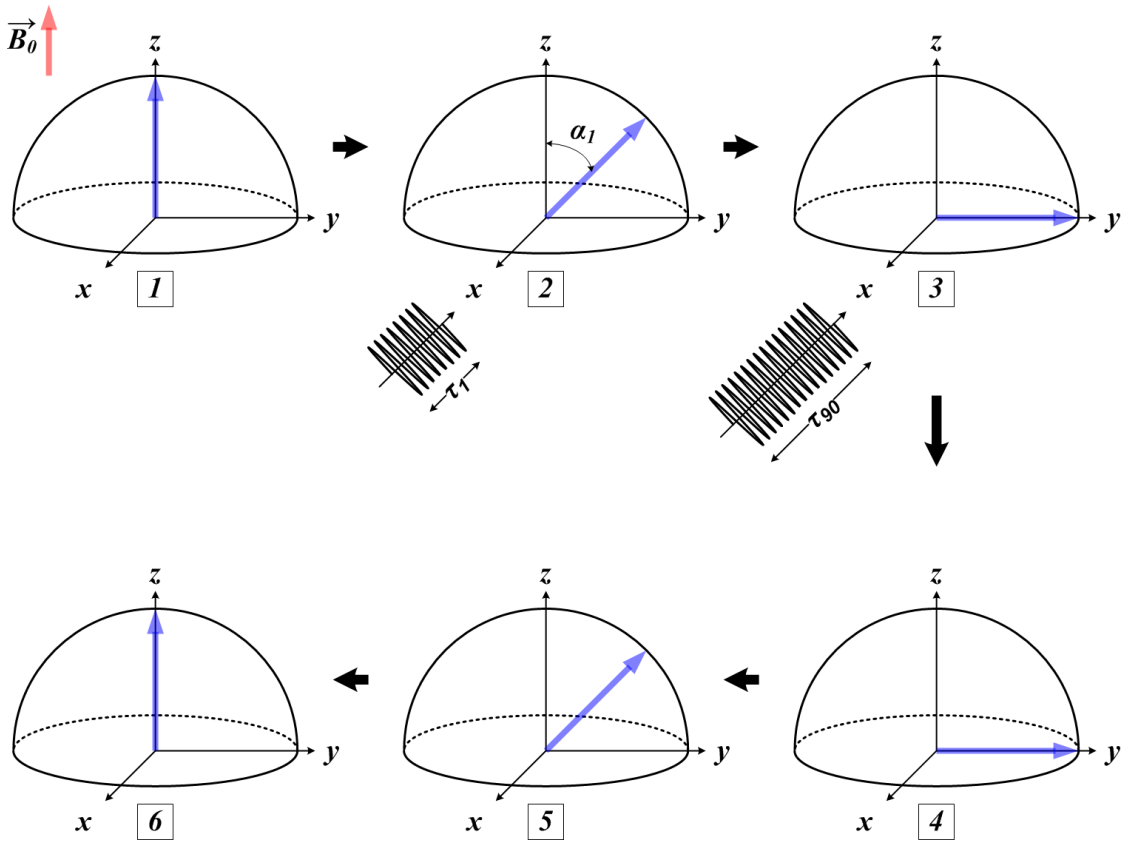

Figure 2.6: Conceptual excitation and relaxation of total net magnetization

Fig. 2.6 (2), an incoming RF excitation with time duration (τ_1) changes the proton's axis of spin by the angle (α_1) based on this formula

$$\alpha_1 = \gamma B_1 \tau_1 \tag{2.31}$$

As an effect of the external stimulus provided by the RF energy, the total net magnetization vector now has values for all x, y and z components. With RF pulses of longer time duration, the flip angle can approach 90 degree. This specific time duration giving a 90 degree flip is called τ_{90}. The total magnetization vector's (M) z-component is zero and the x and y components are as shown in Fig. 2.6 (3). When the RF signal is turned off, the total net magnetization attempts to go back to the original states ($M_x = M_y = 0$, $M_z \neq 0$). Fig. 2.6 (4), (5) and (6) shows the transition to the initial total net magnetization after the RF signal is off. A more realistic diagram of excitation and relaxation of total net magnetization is shown in Fig. 2.7

When the NMR signal emitted during relaxation is picked up at the NMR coil, it looks like a decaying sinusoid with a time constant (T_1 or T_2) and a specific frequency (ω_0 = Larmor frequency). This is called a free induction decay (FID). T_1 represents the time constant of relaxation of the NMR signal on the z-axis and T_2 represents the time constant of relaxation of NMR signal on x-y plane shown in Fig. 2.8. Fig. 2.9 shows an example of NMR signals on the z axis and the x-y plane.

The NMR signal on the z-axis is just recovering amplitude without a Larmor frequency component. The NMR signal picked up on the x-y plane precesses and is decaying with Larmor frequency. Both $T1$ and T_2 are measured after the NMR signals

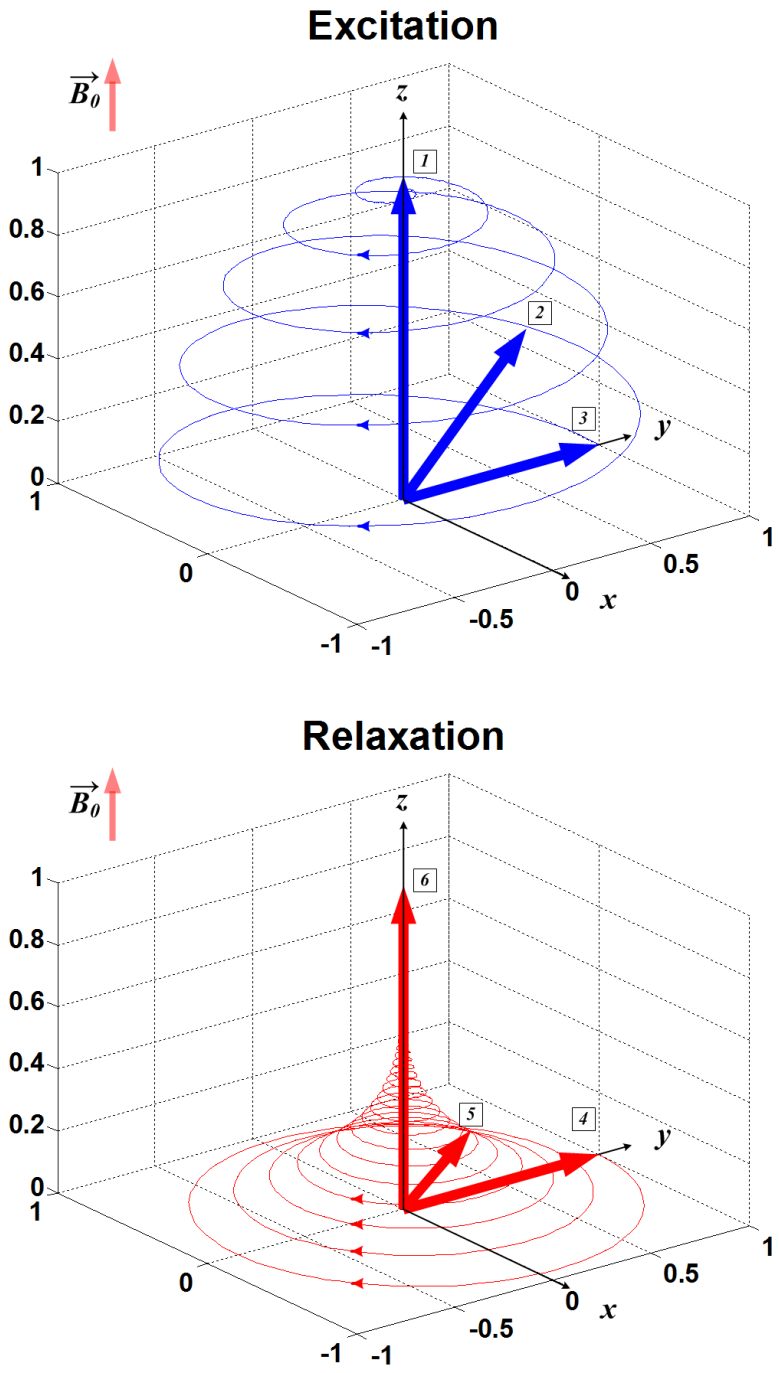

Figure 2.7: Realistic excitation and relaxation of total net magnetization

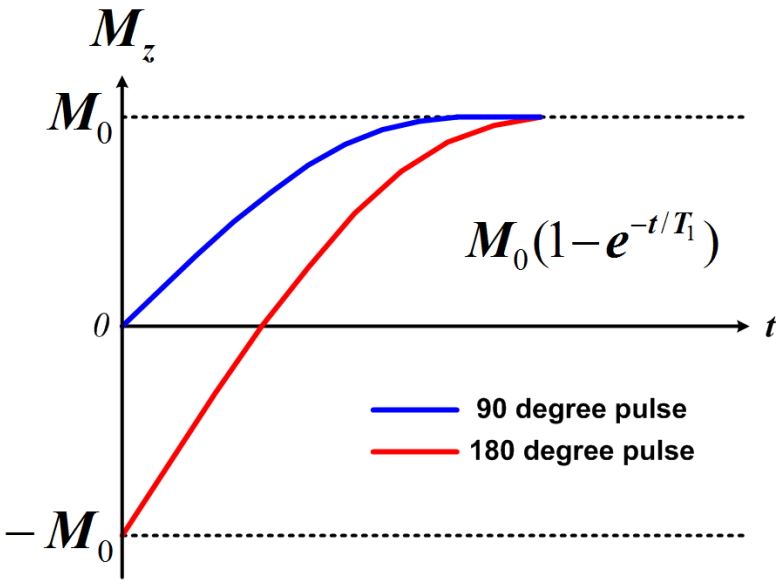

(a) NMR relaxation on z-axis (T1 based)

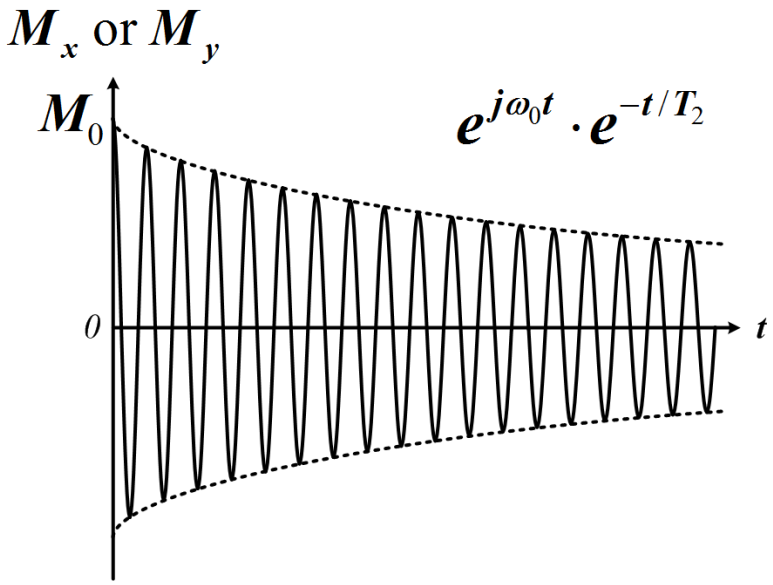

(a) NMR relaxation on x-y plane (T2 based)

Figure 2.8: T1 and T2 of NMR signal relaxation

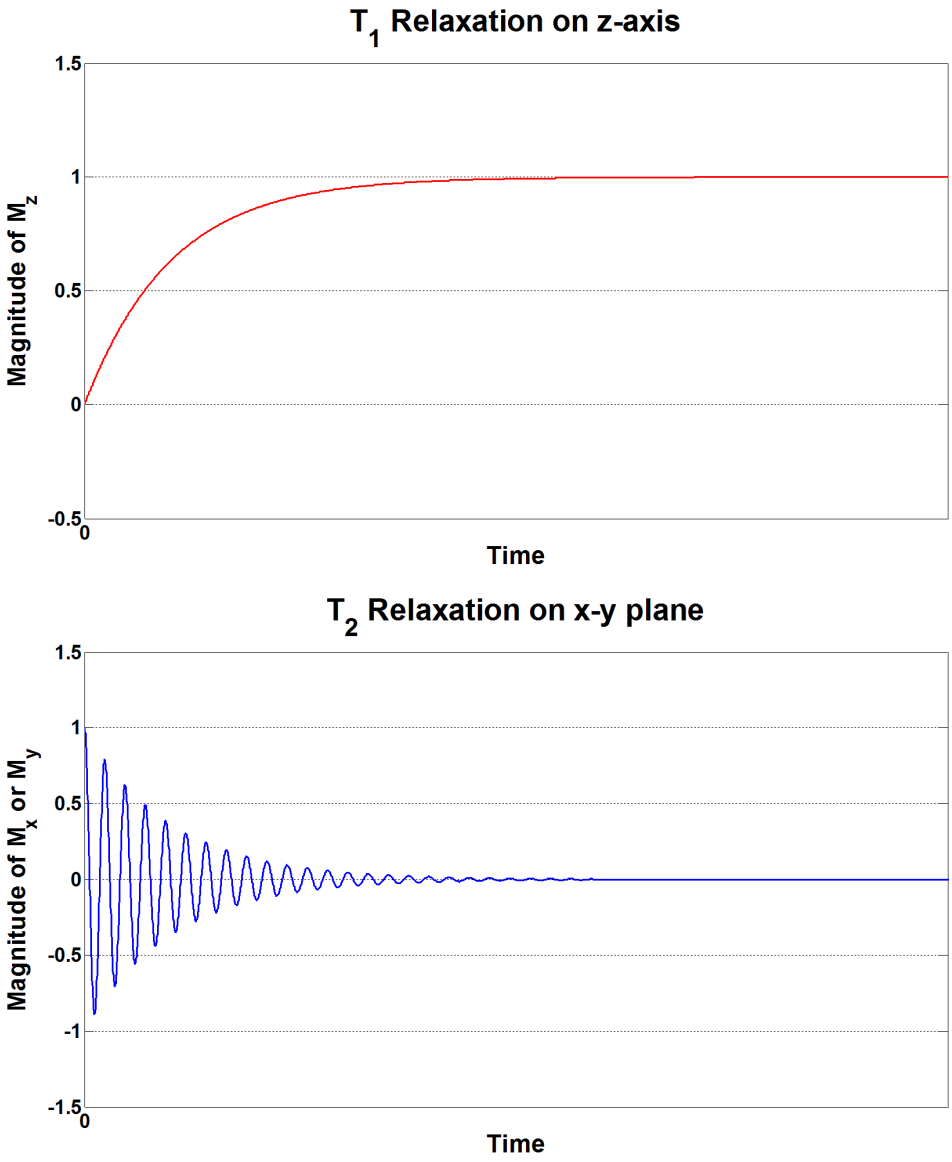

Figure 2.9: Example of T1 and T2 of NMR signal relaxation after τ_{90}

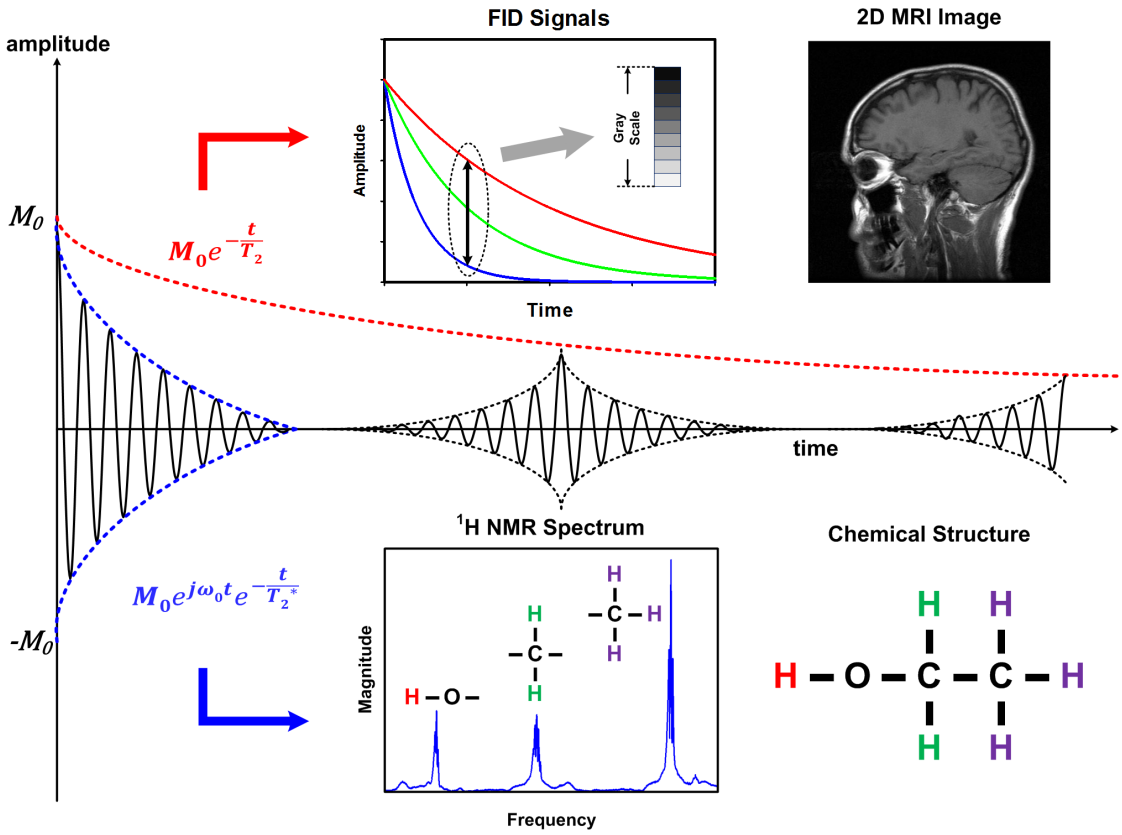

Figure 2.10: Applications of NMR signals

are obtained at the coil only on the x-y plane not z-axis with different specific pulse sequencing. T_1 is based on spin-lattice interaction (in other words, surrounding environment) and T_2 is based on spin-spin interaction (interactions between individual spins). In an MRI image, both T_1 and T_2 are used to build an image with the aid of complex pulse sequencing and k-space. In NMR spectroscopy, only T_2 and NMR frequency are considered. A useful fact is that T_1 has 5 to 10 times longer time duration than T_2. Fig. 2.10 shows applications of both T_1 and T_2. From now, we will focus on T_2, and not T_1 because the focus of our NMR transceiver is spectroscopy.

2.2 Signal to Noise Ratio

With this basic understanding of NMR fundamentals, we need to estimate the received signal level to design the NMR system. Based on the analysis of [5–8], we will re-derive the NMR signal level and NMR signal to noise ratio. A B_1 field generated from an NMR coil carrying unit current introduces the electro motive force (EMF) on the total magnetization (M) of the sample. This EMF (ξ_{dV}) is given by

$$\xi_{dV} = -\frac{\partial}{\partial t}\{\mathbf{B_1} \cdot \mathbf{m}\} \tag{2.32}$$

where $\mathbf{m}$ is the total magnetization vector of the unit volume (dV). After the RF signal is applied to the sample during τ_{90}, $\mathbf{m}$ is

$$\mathbf{m} = jM_0 e^{j\omega_0 t} e^{-t/T_2} dV = jM_0 e^{\left(j\omega_0 - \frac{1}{T_2}\right)t} dV \tag{2.33}$$

Thus, the EMF (ξ_{dV}) is expressed as

$$\xi_{dV} = -\omega_0 B_1 M_0 e^{\left(j\omega_0 - \frac{1}{T_2}\right)t} dV \tag{2.34}$$

where the magnitude of total magnetization (M_0) is

$$M_0 = N_s \gamma^2 \left(\frac{h}{2\pi}\right)^2 I(I+1) B_0 \frac{1}{3kT} = \frac{N_s \gamma^2 h^2 I(I+1) B_0}{12\pi^2 kT} \tag{2.35}$$

From the unit volume (dV), the maximum EMF ($\xi_{max,dV}$) which is obtained at time t = 0 is

$$\xi_{max,dV} = \frac{N_s \gamma^2 h^2 I(I+1) B_0 \omega_0 B_1 dV}{12\pi^2 kT} \tag{2.36}$$

Integrating the EMF from the unit volume in the sample volume (V_s), EMF (ξ_{max,V_s}) is given by

$$\xi_{max,V_s} = \frac{N_s \gamma^2 h^2 I(I+1) B_0 \omega_0 B_1 V_s}{12\pi^2 kT} \tag{2.37}$$

$$= \frac{N_s \gamma^3 h^2 I(I+1) B_0^2 B_1 V_s}{12\pi^2 kT} \tag{2.38}$$

Equation. (2.38) gives us important insights for improving the NMR signal level. To increase the NMR signal, we need

1. Higher B_0 (dependent on the quality of a magnet)
2. Larger N_s and V_s (spin density per unit volume and total sample volume)
3. Higher B_1 (sometimes, replaced with $\frac{B_1}{i}$, described as coil sensitivity)

With the derived EMF, SNR is defined as the ratio of the rms of the NMR signal and the rms noise with the aid of previous works [5, 6, 9]

$$SNR = \frac{rms\ NMR\ Signal}{rms\ Noise}$$

$$= \left(\frac{\eta k_0 \gamma^3 B_0^2 N_s}{3\sqrt{2}kT}\right)\left(\frac{B_1}{i}\right)\left(\frac{V_s}{v_{rms-noise}}\right)\left(\frac{h}{2\pi}\right)^2 I(I+1)F \tag{2.39}$$

$$= \left(\frac{\eta k_0 \gamma \omega_0^2 N_s}{3\sqrt{2}kT}\right)\left(\frac{B_1}{i}\right)\left(\frac{V_s}{v_{rms-noise}}\right)\left(\frac{h}{2\pi}\right)^2 I(I+1)F \tag{2.40}$$

where η is the ratio of the sample volume to the coil volume (i.e., the filling factor), k_0 is a constant that accounts for any spatial inhomogeneity in the B_1 field, V_s is the sample volume, N_s is the spin density per unit volume, γ is the gyro-magnetic ratio, h is Planck's constant, I is the spin angular momentum quantum number of the sample, ω_0 (= γB_0) is the Larmor frequency, k is Boltzmann's constant, T is the absolute temperature measured in Kelvin, and F is the input referred noise factor of the entire NMR receiver

path. The total root-mean-square noise from coil and sample is $v_{rms-noise}$ and the factor of $\sqrt{2}$ is introduced since the received signal is sinusoidal. The magnetic flux density per unit current, shown as B_1/i, describes the excitation RF coil sensitivity. The noise ($v_{rms-noise}$) through an NMR experiment is mostly thermal noise generated in the receiver coil and sample and is described as

$$v_{rms-noise} = \sqrt{4kTR_{noise}\Delta f} \tag{2.41}$$

In Eq. (2.41), a resistance R_{noise} represents the conductive losses of the coil itself as well as magnetic (eddy current) and dielectric losses in the sample and surrounding structures [5]. Δf is the bandwidth (in Hz) of the receiver. The mathematical definition of filling factor (η) above Equation. (2.40) is given by

$$\eta = \frac{V_s}{2V_c} \tag{2.42}$$

where V_c is the volume of the coil. This term is satisfactory for a solenoid coil, but its validity for other types of coils is questionable [5]. Now look for a RF coil sensitivity. In [5], Hoult and Richards introduces the principle of reciprocity for calculating the sensitivity of an RF coil. The signal received from a sample by a coil is proportional to the magnetic field which would have been created in the sample if a unit current passes through the coil. Therefore, the SNR is directly proportional to the previously defined sensitivity of the RF coil.

Chapter 3

Design Considerations

3.1 Water Suppression and Phase Noise

In the previous chapter, we studied the fundamentals of NMR and calculated the NMR signal level and NMR signal-to-noise ratio. However, it is still not enough to design the circuits for an NMR system. Before starting the NMR receiver design, there are some important parameters to be considered. They are listed below.

1. Nuclei of interest (for example, ^{1}H, ^{13}C and ^{31}P)
2. Magnetic field range (B_0)
3. Larmor frequency range (ω_0 or f_0 according to B_0 range)
4. Input signal voltage level (ξ_{max,V_s})

The set of nuclei of interest and the static magnetic field (B_0) range are chosen carefully first. If both of them are selected, the Larmor frequency range for nuclei is determined, as the Larmor frequency is proportional to the magnetic field (B_0) and the gyro-magnetic

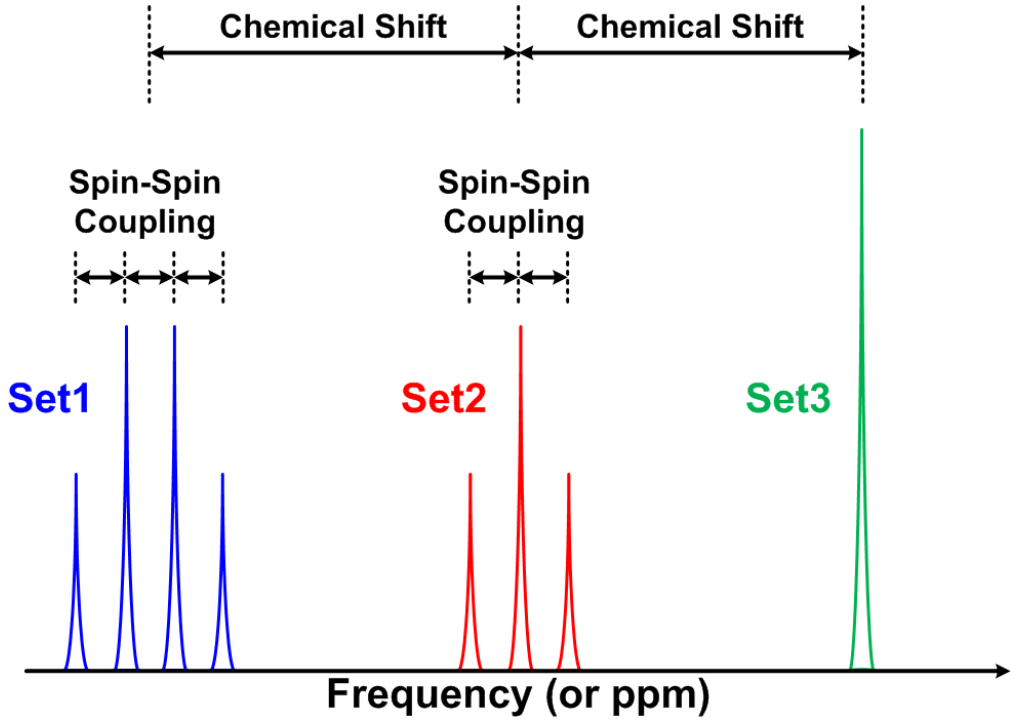

Figure 3.1: Typical NMR spectrum example

ratio (γ). According to previous NMR analysis [5, 6, 9] based on this information, NMR signal levels received by the NMR coil is simply calculated and estimated reasonably. Also the signal level is very important to decide the total gain of receiver chain.

Some of the nuclei used primarily in NMR spectroscopy applications are shown in the first column of Table. 3.1. The second column shows the spin number (I), the third column shows the natural abundance, the fourth column shows the gyro-magnetic ratio (γ), the fifth and sixth columns show the Larmor frequency at 0.5T and 5T, and the last column shows the relative sensitivity. In fact, our NMR receiver attempts to cover the frequency range from a palm-sized magnet having 0.5T used recently in mini

Table 3.1: NMR properties of commonly used in nuclei in NMR [10]

Isotope	Spin (I)	Natural Abundance (%)	Gyromagentic ratio (MHz/T)	Frequency (MHz)		Relative Sensitivity
				0.5T	5T	
^{1}H	1/2	99.985	42.577	21.28	212.88	1
^{2}H	1	0.015	6.536	3.26	32.68	1.45×10^{-6}
^{3}He	1/2	1.4×10^{-4}	32.435	16.21	162.17	5.75×10^{-7}
^{7}Li	3/2	92.58	16.548	8.27	82.74	0.272
^{13}C	1/2	1.108	10.707	5.35	53.53	1.76×10^{-4}
^{14}N	1	99.630	3.078	1.53	15.39	1.00×10^{-3}
^{15}N	1/2	0.370	4.316	2.15	21.58	3.86×10^{-6}
^{17}O	5/2	0.037	5.774	2.88	28.87	1.08×10^{-5}
^{19}F	1/2	100	40.076	20.03	200.38	0.834
^{23}Na	3/2	100	11.268	5.63	56.34	9.27×10^{-2}
^{31}P	1/2	100	17.254	8.62	86.26	6.65×10^{-2}
^{39}K	3/2	93.1	1.989	0.99	9.94	4.75×10^{-4}
^{128}Xe	1/2	26.44	11.860	5.93	59.30	5.71×10^{-3}

bio-sensor MRI applications [11, 12] up to large cylinder type magnets having a few fixed tesla which are commonly used in medical and chemical applications. We limit the maximum magnetic field up to 5T as the broad frequency range is too difficult to design if we include very high magnetic fields (recently up to 17T). The minimum and maximum values of column five and six specify the frequency range of interest between 0.5T and 5T. The 5MHz $\sim$ 300MHz frequency range is selected for the input signal band in our NMR receiver. In the NMR analysis of [5, 6, 9], as NMR signal voltage is highly dependent on the natural abundance and the Larmor frequency, the proton(^{1}H) has the highest sensitivity among nuclei shown in Table. 3.1. This is the reason why it is common to see ^{1}H spectrum in NMR spectroscopy applications. Even though other nuclei are used in NMR spectroscopy, their abundance are so much lower that it is very difficult to detect them. Also, their applications are limited as higher magnetic field and larger volume are needed. In drug discovery, one of our applications, we are interested in identifying the molecular structure and bonds that are formed by these nuclei in Table 3.1 with others. A Typical NMR spectrum example is shown in Fig. 3.1, where there are a number of frequency sets. One set is away from the others and each set has some frequency peaks with tiny frequency differences. The distance between sets represents a chemical shift highly sensitive to the environment surrounding the nuclei. The distance of frequency peak to peaks within each set shows spin-spin coupling which is dependent to a degree on the proximity of the spins to each other. From these chemical shift and spin-spin coupling, we can obtain molecular structural information. The efficacy of NMR

spectroscopy is highly dependent on the spectral resolution and the minimum detectable signal level only a few Hz away from a strong signal.

Revisiting the equation for the free-induction decay (FID) of NMR signal in detail, the signal $r(t)$ is expressed as

$$r(t) = M_0 \cdot e^{j\omega_0 t} \cdot e^{-\frac{t}{T_2}} \tag{3.1}$$

where M_0 is the maximum amplitude of NMR signal and T_2 is the time constant of the NMR signal on the x-y plane. The time constant of the signal is T_2 and is determined by interactions between individual spins. However, if the inhomogeneity of the magnetic field (B_0) is considered, This signal $r(t)$ is expressed as

$$r(t) = M_0^* \cdot e^{j\omega_0 t} \cdot e^{-\frac{t}{T_2^*}} \quad \text{, where} \quad \frac{1}{T_2^*} = \frac{1}{T_2} + \gamma \cdot \Delta B_0 \tag{3.2}$$

where M_0^* is the maximum amplitude of NMR signal (smaller than M_0) and T_2^* ($\ll T_2$) is a new time constant of the NMR signal on the x-y plane when the magnetic field has an inhomogeneity. T_2^* decay depends on both external magnetic field and spin-spin interactions. Taking the Laplace transform of the T_2^* decay, results in

$$\mathcal{L}\{r(t)\} = R(s) = \frac{M_0^*}{s - j\omega_0 + \frac{1}{T_2^*}} \tag{3.3}$$

In Equation. (3.3), if a magnet has no inhomogeneity (equal to ΔB_0=0), the magnitude of $R(s)$ is T_2 and the 3dB-bandwidth offset from Larmor frequency is $\frac{1}{T_2}$. However, if a magnet has inhomogeneity (equal to $\Delta B_0 \neq 0$), the magnitude of $R(s)$ is T_2^* and the 3dB bandwidth offset from Larmor frequency is $\frac{1}{T_2^*}$. Thus, as the inhomogeneity increases, the magnitude decreases and the 3-dB-bandwidth increases. Typical measured values for

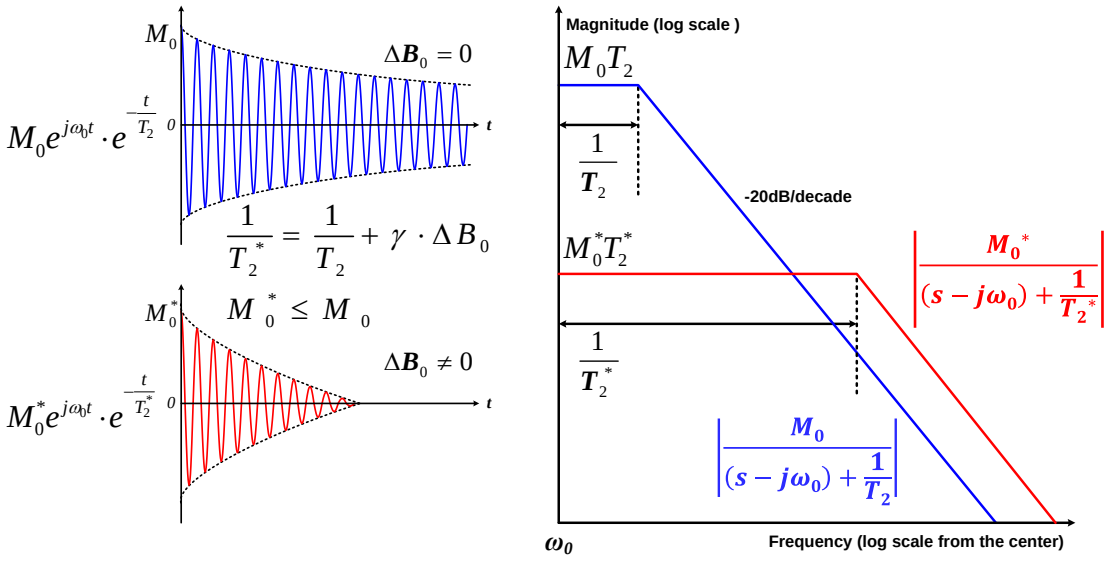

Figure 3.2: Comparison with T_2 and T_2^* decay

T_2^* for ^{1}H in water range within ($\sim$100μs$\leq T_2^* \leq \sim$10s) where the larger number is only approached in the ideal case. For NMR spectroscopy applications, good homogeneity of the magnet is needed to get larger T_2^* (narrow spectral line width). As the magnet is not perfect inherently, its magnetic field has inhomogeneity that it will be improved through the shimming process that adds additional coils surrounding a magnet to compensate for the nonlinearity of a magnetic field (B_0). T_2^* approaches to T_2 as inhomogeneity decreases. To maximize T_2^*, T_2 also has to be maximized. For T_2, the effect of spin-spin interaction depends to a degree on the proximity of the spins to each other. For example, in water (H_2O), the protons are separated more widely than they are in a solid tissue. Hence, the de-phasing effect of spin-spin interaction might not be as prominent in H_2O as it is in a solid tissue. Fig. 3.2 shows comparison with T_2 and T_2^* decay.

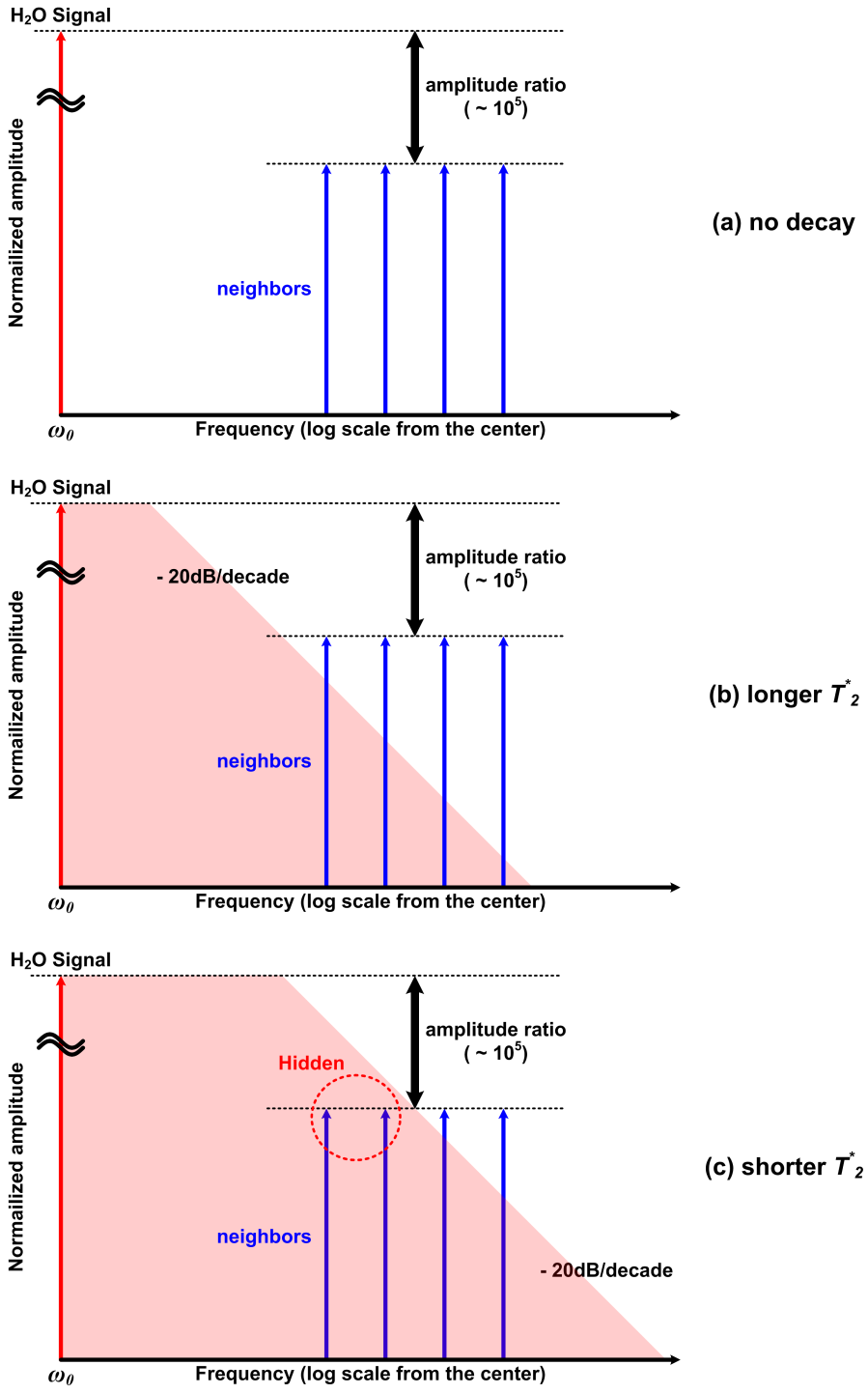

Figure 3.3: Signal masking effect due to T_2^* (example, H_2O and its metabolites)

Line width broadening due to T_2^* has severe effect on NMR spectroscopy when meaningful frequency components are so close to each other and there exists a large magnitude ratio among them. In particular, there is 10^5 (= 100dB) ratio between H_2O and its near metabolites in the ^{1}H NMR spectrum from the NMR sample containg water (H_2O). Fig. 3.3 shows the ^{1}H NMR spectrum for H_2O and its metabolites as an example. Fig. 3.3 (a) is the desired spectrum corresponding to the infinite T_2^*. Line widths of all frequency peaks are extremely narrow. But, when finite T_2^* is considered, they have broad line widths. Longer T_2^* makes H_2O neighbors (metabolites) to be distinguished even though H_2O has a broad line width shown in Fig. 3.3 (b). Shorter T_2^*, due to inhomogeneity of B_0, hides some of metabolites shown in Fig. 3.3 (c). To detect hidden metabolites in this situation, the easiest way is to increase the magnetic field (B_0) because the distance (chemical shift) between H_2O and its metabolites is proportional to B_0. This method assumes that T_2^* is independent of B_0. In reality, T_2^* has a slight dependency on B_0.

We studied the T_2^* masking effect on NMR spectrum due to inhomogeneous magnetic field. Along with the phase noise contribution of the frequency synthesizer used in wireless communication systems, this effect should be discussed carefully. Frequency synthesizers are used to down convert the high frequency input signals to lower frequencies to simplify further signal processing. The basic function of down conversion is shown in Fig. 3.4. If the NMR signal input is assumed to be an ideal tone, the phase noise of the frequency synthesizer is present at the IF frequency after the down conversion process. Now, consider the ^{1}H NMR spectrum again with this down conversion process. As shown

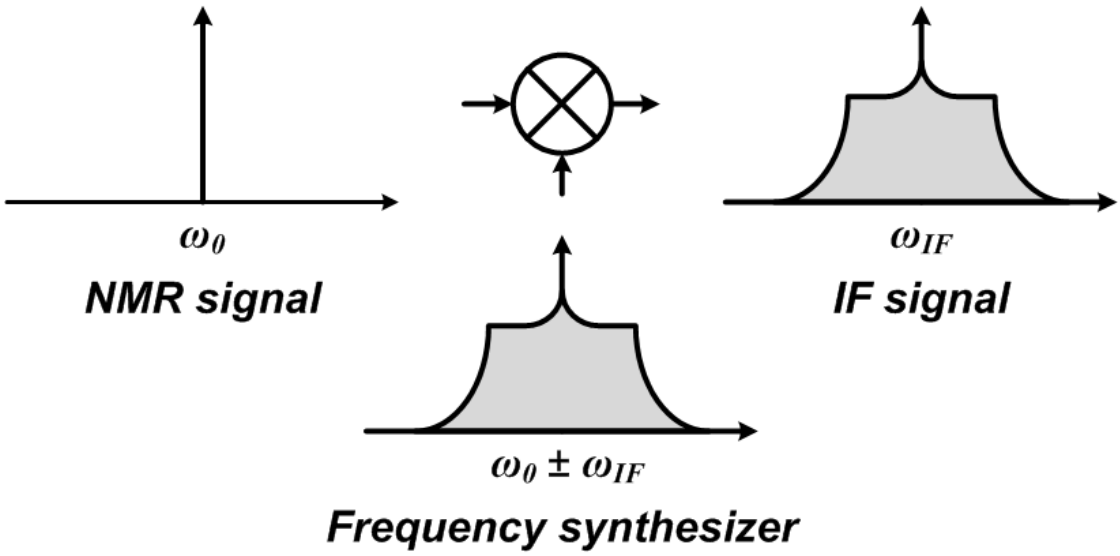

Figure 3.4: Down conversion process

in Fig. 3.3, identifying molecules with hydrogen (^{1}H) in a water solution is some of the most interesting but are also the most difficult. Due to its natural abundance and the high gyro-magnetic ratio (42.58 MHz/T), the water signal is very large, while the signals of interest (called metabolites) are small ($\sim 10^{-5}$ smaller) and very close (10s to 100s of Hz away) to the water (H_2O) signal as shown in the leftmost diagram in Fig. 3.5(a). Ideally we would expect the same spectrum at the IF frequency band without any frequency contamination when only phase noise of the frequency synthesizer is considered. Including the Lorentizian shape due to the FID characteristic of the NMR signal shown in Fig. 3.5(b), the spectrum is a little bit broadened according to the homogeneity of B_0. However, the constraints on the shimming process to improve the homogeneity of B_0 are extremely severe even if the phase noise effect of the frequency synthesizer is ingnored. At the receiver, the down-conversion process from the mixer convolves the close-in phase

noise of the local oscillator with the large H_2O signal. The convolved spectrum hides the tiny meaningful neighboring signals substantially. In other words, magnetic field inhomogeneity results in a faster FID decay, i.e, a wider Lorentzian line width. A larger line width hides the neighboring metabolites even if the receiver has good phase noise performance.

Practical NMR systems utilize magnetic sequence based water suppression techniques (e.g., pre-saturation, watergate, flipback, jump and return [13–15]) to try to mitigate the problem of the shadowing by the FID Lorentzian. Water suppression also reduces the dynamic range of signals the system needs to handle and consequently the phase noise requirements. However, aggressive use of water suppression methods introduce spectrum baseline distortion which limits their usefulness [16]. However, some amount of water suppression (40-80dB) is unavoidable in order to suppress the Lorentzian sufficiently. At the receiver the downconversion process convolves the close-in phase noise of the local oscillator with the large residual ^1H signal masking the small neighboring signals if one is not careful. By reducing the LO phase noise we are able to reduce the amount of water suppression that is needed, thus reducing nonlinear artifacts such as baseline distortion. Additionally, it should be noted that though water suppression reduces the phase noise requirements for the RX, the phase noise of the TX is critical during water suppression to avoid suppressing the metabolites as well. By reducing the LO phase noise and increasing the dynamic range of the system we reduce the need for water suppression as shown in Fig. 3.5(c).

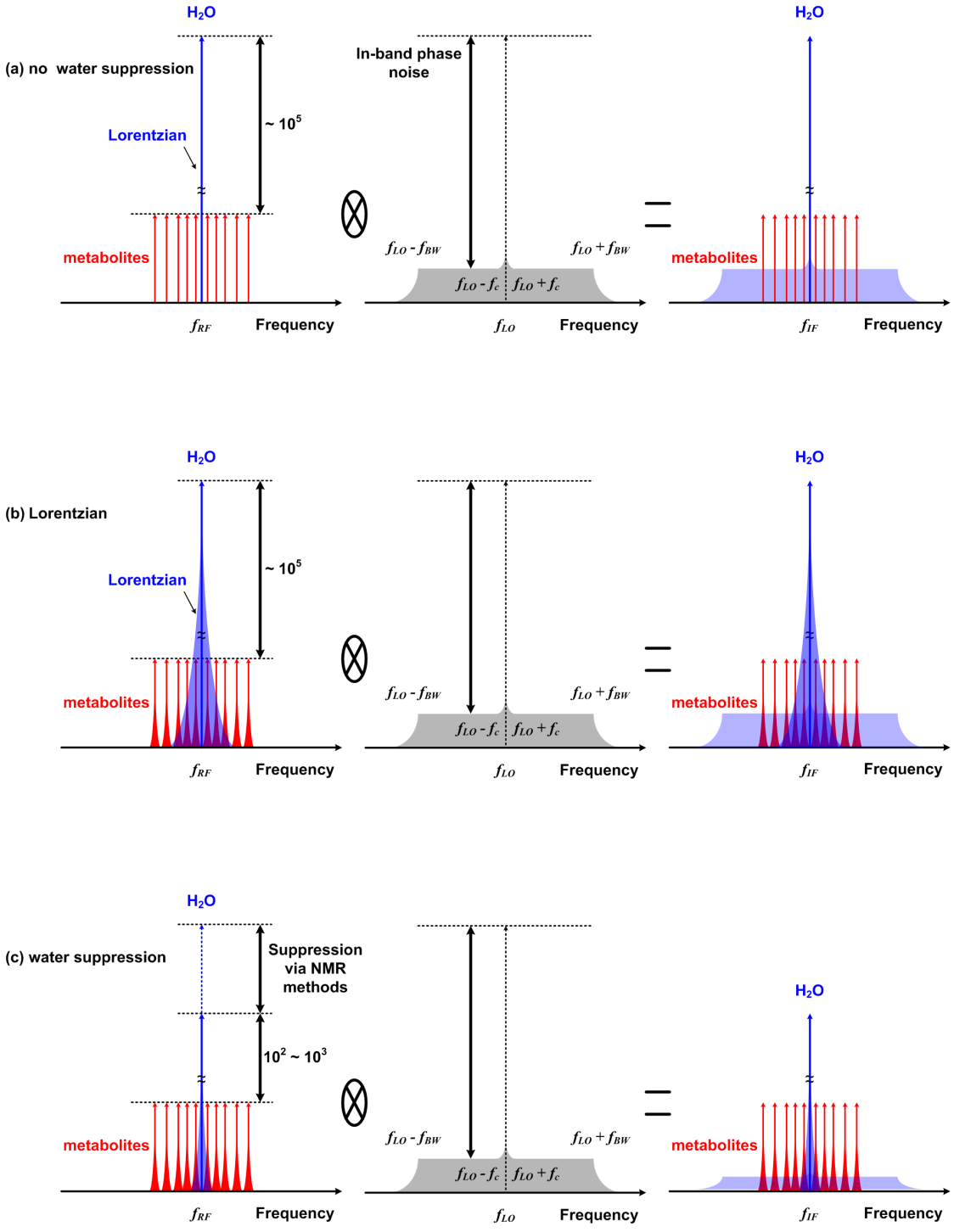

Figure 3.5: Typical NMR spectrum example

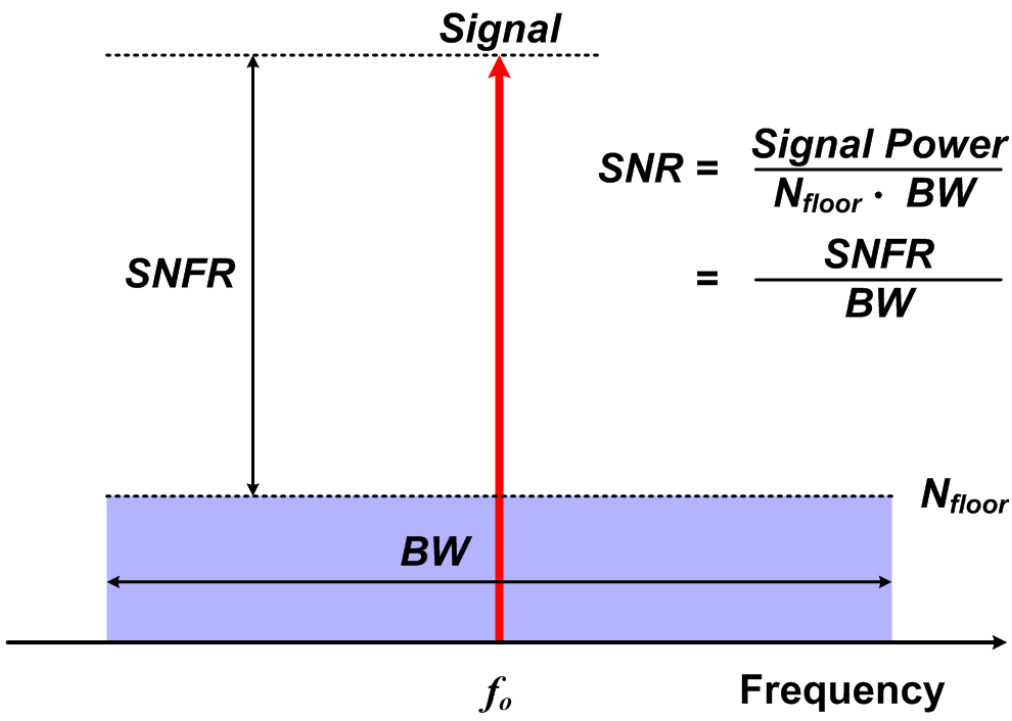

Figure 3.6: Relationship between SNR and SNFR

To calculate the dynamic range of the NMR system, we need to define SNFR (signal to noise floor ratio) as a new parameter different from the typical SNR (signal to noise ratio).

$$SNR = \frac{P_S}{P_N} \tag{3.4}$$

$$= \frac{P_S}{N_{floor} \cdot BW} \tag{3.5}$$

$$SNFR = \frac{P_S}{N_{floor}} \tag{3.6}$$

$$= SNR \cdot BW \tag{3.7}$$

Fig. 3.6 depicts this relationships between SNR and SNFR. To allow for a 20dB SNFR

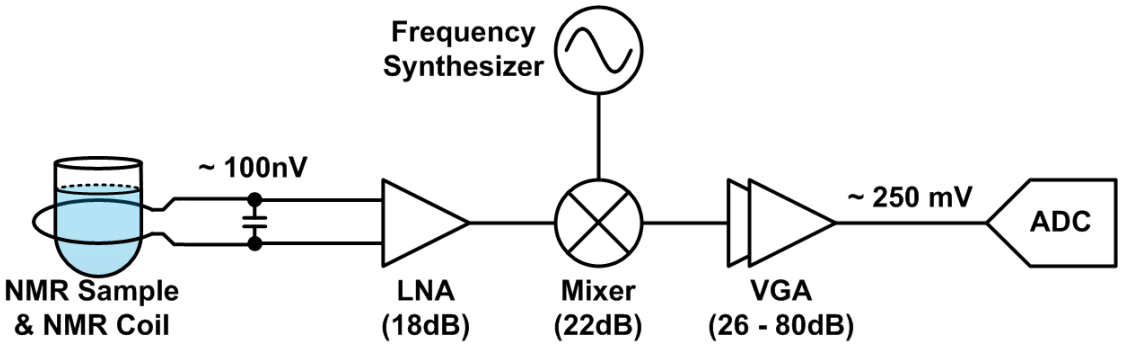

Figure 3.7: Receiver chain gain distribution

for the signals at the output, the close-in phase noise (at 10Hz from carrier) of the LO has to be better than 120dB because there is a 100dB difference between the H_2O signal and its neighbors when no Lorentzian is considered. The constraint on the dynamic range of the receiver is even larger if we include a 10dB AGC slack, 6dB of offset slack and etc, resulting in a ADC dynamic range close to 140dB, i.e., extremely difficult to design.

The induced NMR signal level at the receiver coil from small samples varies from 100nV to 40uV, requiring a AGC range of 50dB and a maximum receiver chain voltage gain of 120dB as shown in Fig. 3.7.

3.2 Phase Noise Requirement

In the previous section, conceptually we understood the effects from the T_2^* and the phase noise of the frequency synthesizer. A frequency synthesizer is definitely needed to build a NMR transceiver. How do we decide the phase noise of it? Assume that there is

Table 3.2: Lorentzian magnitude of strong NMR FID signal

T_2^*	Lorentzian magnitude at offset (dB)			
	$1Hz$	$10Hz$	$100Hz$	$1000Hz$
16 s	-40	-60	-80	-100
1.6 s	-20	-40	-60	-80
160 ms	X	-20	-40	-60
16 ms	X	X	-20	-40
1.6 ms	X	X	X	-20
160 μs	X	X	X	X

one strong signal and there are a few of its neighbors at 10Hz, 100Hz and 1000Hz offsets, and that no Lorentzian due to FID exists. Also we define $SNFR_{min}$ for all frequency peaks to be able to distinguish them. As the in-band phase noise floor of the frequency synthesizer is flat, we can derive the required phase noise of it to guarantee $SNFR_{min}$. The maximum of the required phase noise of the frequency synthesizer is expressed as

$$PN_{max,in-band} = -max\{dB1, dB2, dB3\} - SNFR_{min} \tag{3.8}$$

where $dB1$ is the dB difference between the magnitude of strong signal and the neighbors at 10Hz offset from the strong signal, $dB2$ is for the neighbors at 100Hz offset from the strong signal and $dB3$ is for the neighbors at 1000Hz offset from the strong signal.

Comparing them, choose the maximum and subtract $SNFR_{min}$ from it to calculate the allowable maximum in-band phase noise of the frequency synthesizer. The Table. 3.2 lists the relative Lorentzian magnitude of strong signal at 1, 10, 100 and 1000 Hz offset for different values of T_2^*. X means the flat amplitude at offsets.

Assume that we obtained a T_2^* of 1.6 s from the shimming process. If the neighbor signals are 10^5 (=100dB) times smaller than a strong signal and is 100Hz away from it, we cannot see its neighbors since the Lorentzian FID is only 60 dB down from the signal peak . The question then becomes, is the phase noise of frequency synthesizer not important? In the receiver, the answer is yes. But we still need to see them. Look at the Fig. 3.9 that shows an example of suppression of a strong signal. When RF signal with lower power and longer time duration ($\tau_{90,1}$) is applied to the sample at frequency a strong signal has, only a net magnetization of a strong signal is flipped over the x-y plane. Then another RF signal with higher power and shorter time duration ($\tau_{90,2}$) is applied to the sample. All net magnetization in the sample experiences a 90 degree shift because the shorter pulse has a broader bandwidth in frequency domain and excites the entire sample. Net magnetization of all neighbors, except the strong signal are on the x-y plane. However, now a strong signal magnetization is aligned with the z-axis. When the RF signal is turned off, all neighbors induce their EMF on the NMR receiver coil, but the strong signal relaxes along the z-axis and does not induce EMF on the coil. Here the phase noise of frequency synthesizer is very important to excite only the strong signal without having an effect on its neighbors. If the amplitude ratio between

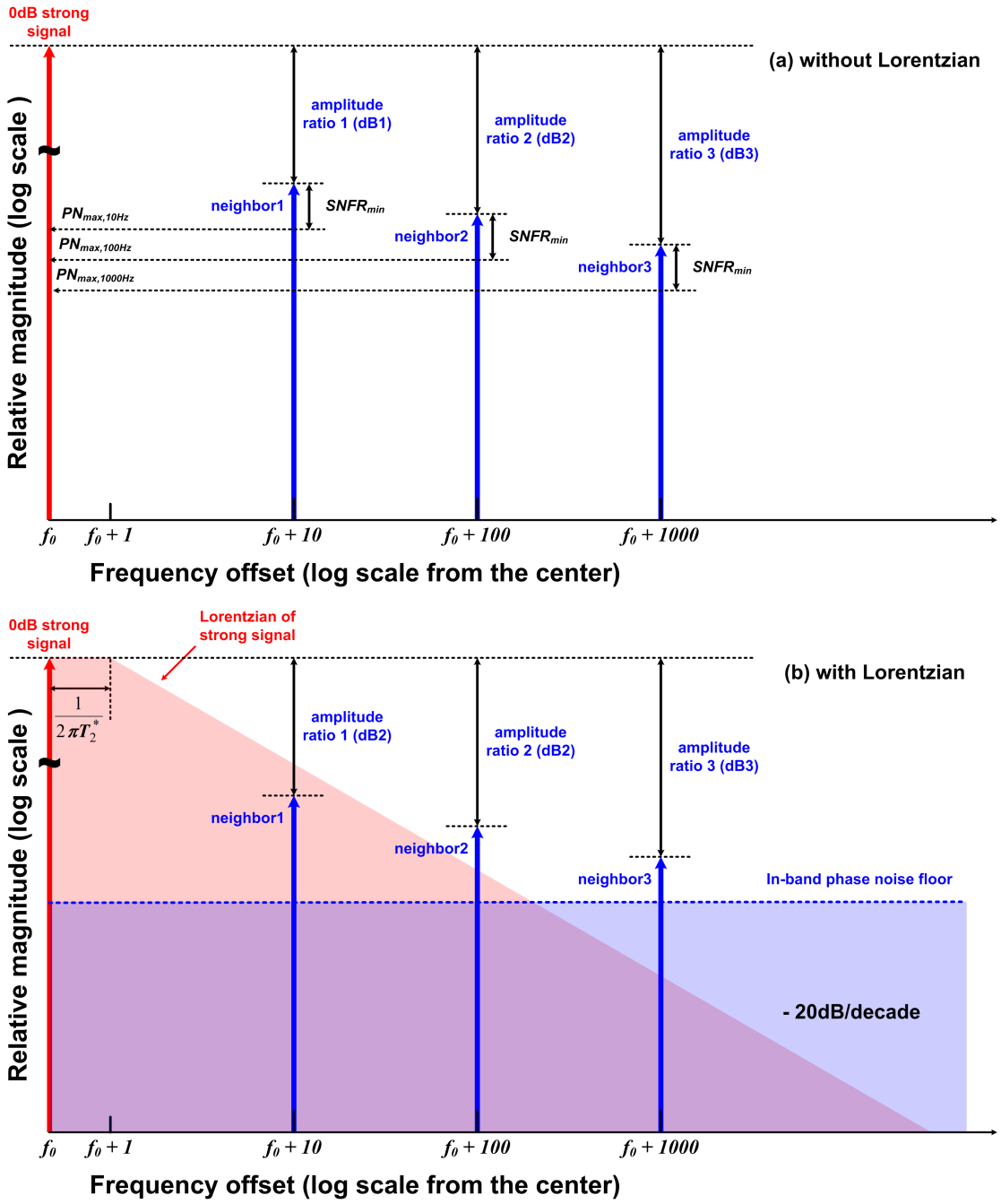

Figure 3.8: Consideration of phase noise requirement

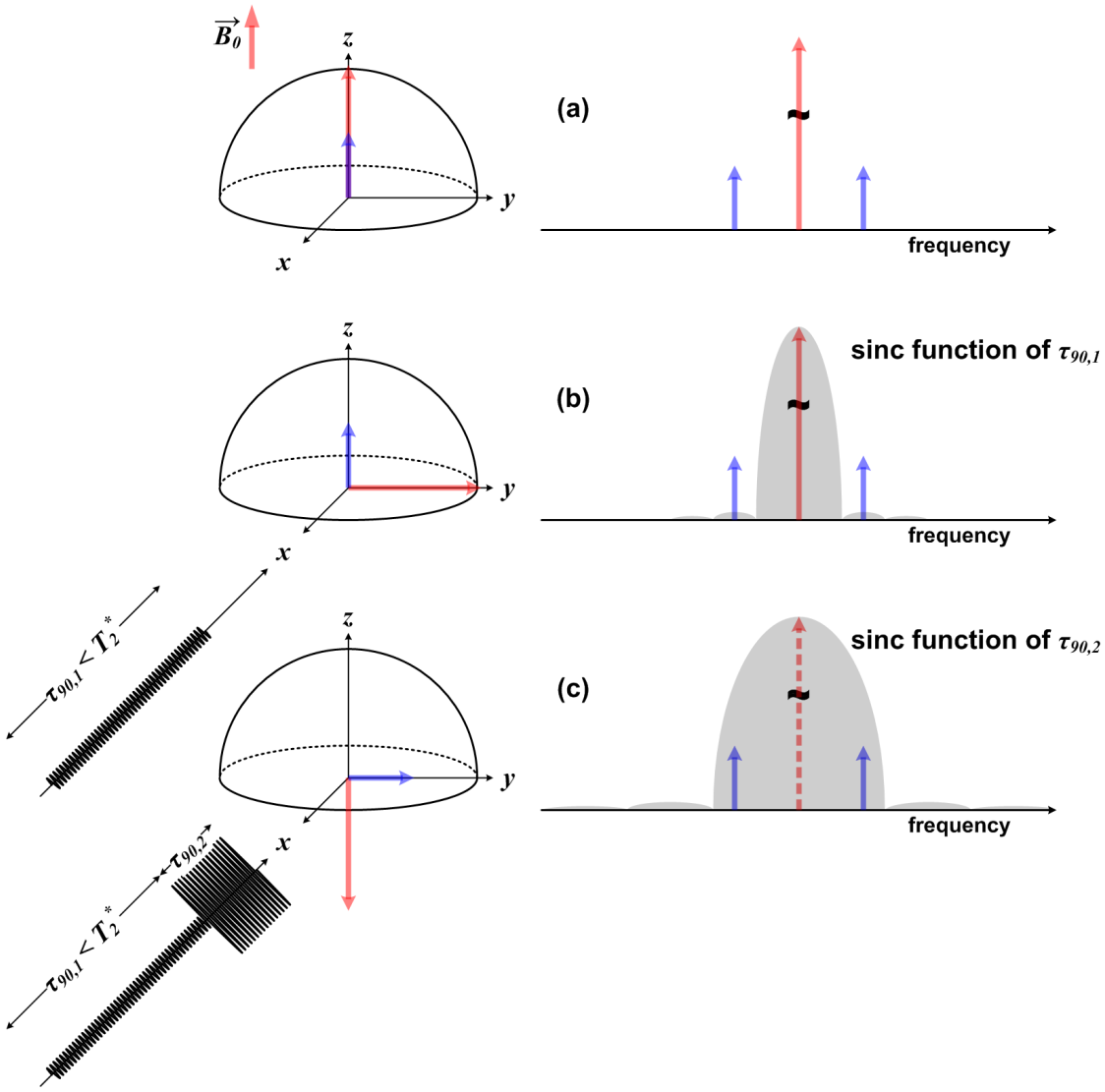

Figure 3.9: Water suppression

the strong signal and its neighbors is 10^5 (=100dB), the in-band phase noise floor of the frequency synthesizer should be less than -100 dBc. This is the reason why the frequency synthesizer of the NMR transceiver must have lower phase noise

3.3 Passive multiplication

According to NMR analysis [5], the NMR signal is proportional to the square of the Larmor frequency (ω_0) as well as the RF coil sensitivity linearly. Most previous efforts to increase the SNR have focused primarily on using a stronger magnet that increases the Larmor frequency [17, 18] and developing a coil with high quality factor. Despite these efforts, the signals received from conventional external RF coils in MRIs do not provide sufficient SNR for spectroscopy. The signal SNR increases dramatically when the sensor, i.e., the RF coil, is physically adjacent to the sample (or tissue) of interest due to the increase in the fill factor (η). Therefore, a small form-factor CMOS integrated spectrometer implanted within the human body provides sufficient SNR to track the location and health of tagged cells under therapy or follow the perfusion of tissue deep inside the body. (First and seconds chips were designed for implantable and portable NMR spectroscopy)

In a conventional NMR system, the receive coil is typically some distance away (usually more than a large fraction of the wavelength) from the receiver electronics and is therefore, connected via a shielded RF cable with a characteristic impedance (usually 50Ω). The NMR-receive coil is impedance matched to the connecting cable for maximum

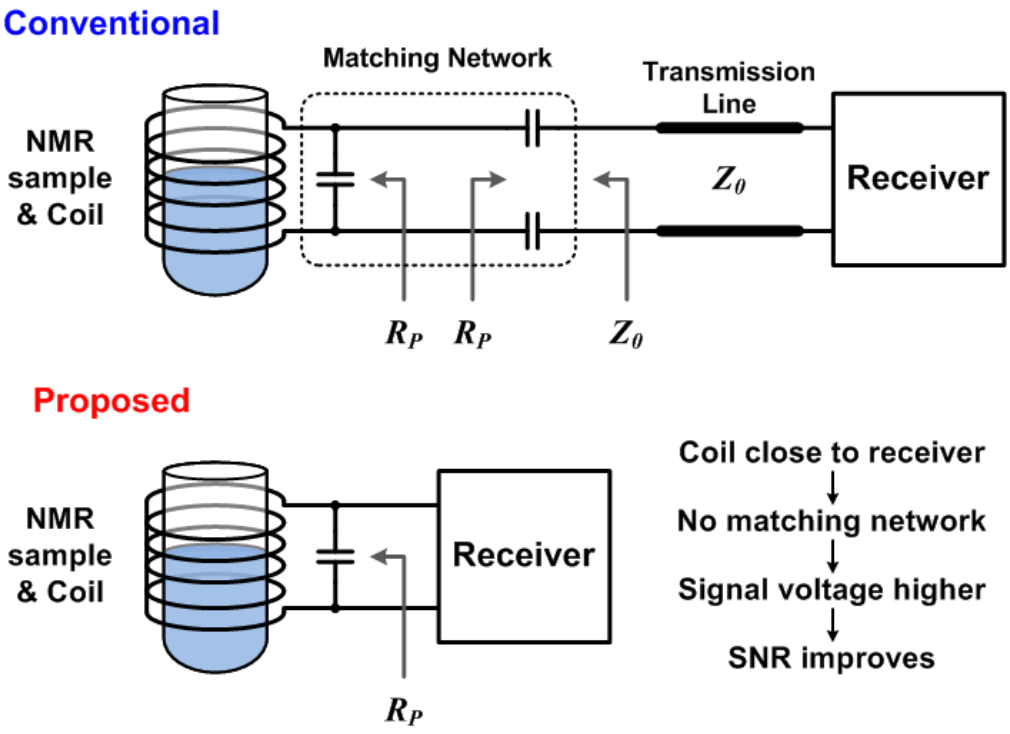

Figure 3.10: Comparison of the conventional and proposed schemes

power transfer. This conventional approach is shown on the top of Fig. 3.10. Our new approach of bringing the receiver close to the coil is shown on the bottom of Fig. 3.11. The difference between the conventional approach and the new approach results from the avoidance of the transmission line and the impedance matching network. To analyze the two separate cases, we draw the equivalent small-signal circuit models as shown in Fig. 3.11. The induced electro-motive force (EMF) (ε_{coil}) generated by the coil is the same for both cases. Further, let us assume that, at resonance, the parallel equivalent impedance caused by the finite Q of the coil alone is given by R'_P. Typically, this value is much larger than Z_0, the characteristic impedance of the transmission line. For example,

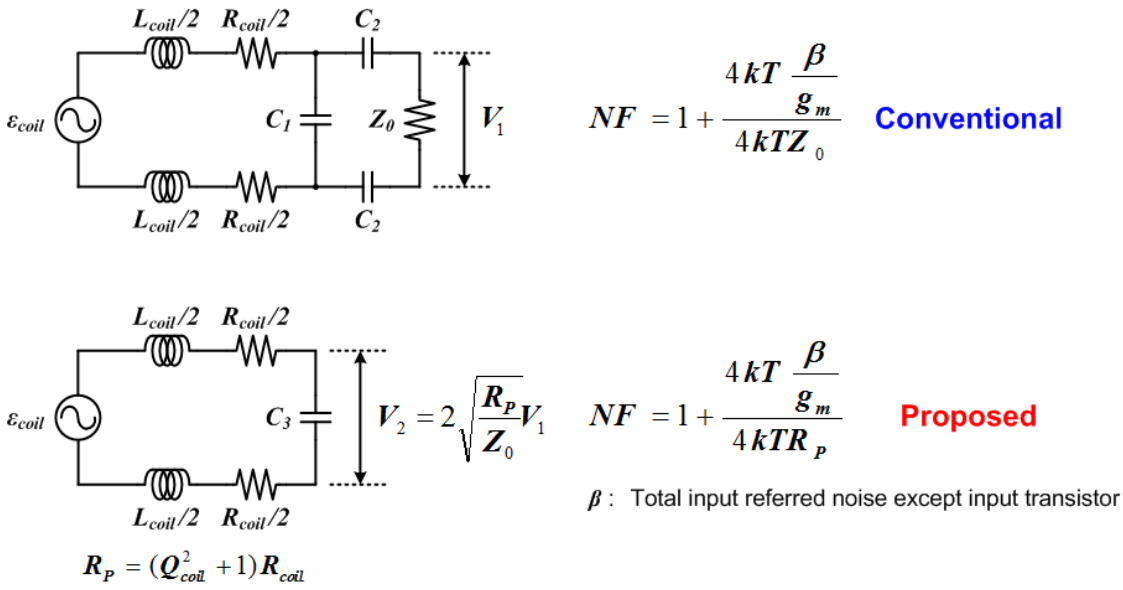

Figure 3.11: Small-signal equivalent models for the two schemes

in our first chip design focusing on Phosphorus, the Q for our calculated external coil of $353nH$ (f_{Larmor} for ^{31}P @ 5T = 86MHz) is 30, resulting in a $R'_P = 5600\Omega$. This open-circuit parallel tank resistance is loaded by the lossy nature of tissue ($\approx 1.2k\Omega$) resulting in a equivalent $R_P \approx 1k\Omega$. In the conventional circuit, when a matching network, transmission line and input match is inserted to connect the coil to the receiver input, the quality factor of resultant circuit is reduced to half of the original value. This is because the impedance seen by the coil due to the impedance match of the receiver is also R_P. The resulting voltage at the node before the matching circuit is given by $Q\varepsilon_{coil}/2$. Maximum power transfer occurs when the R_P is transformed to Z_0 and the resulting power at the receiver input is given by (3.9).

$$P_{signal} = \frac{(Q \cdot \varepsilon_{coil})^2}{8R_P} = \frac{V_1^2}{2Z_0} \tag{3.9}$$

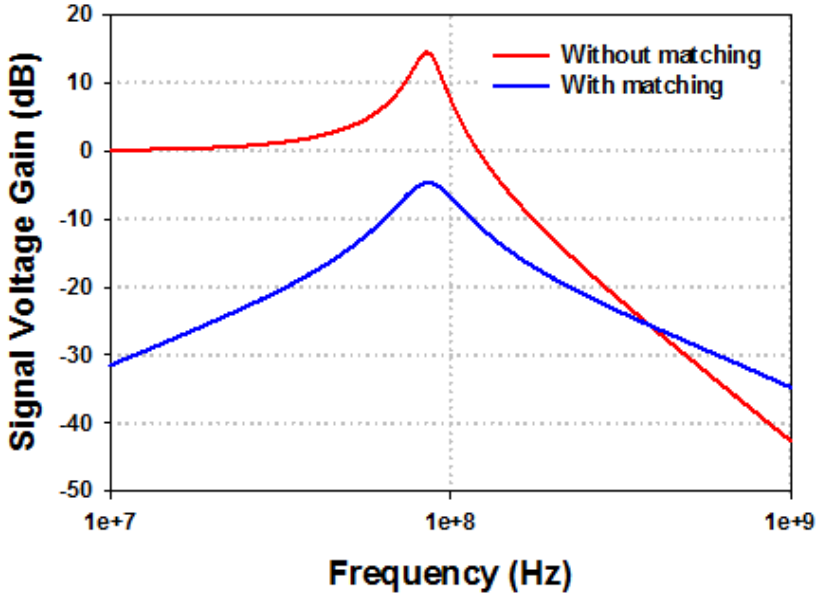

Figure 3.12: Signal transfer function for tradition vs. new approach

In CMOS circuits, in particular at these lower RF frequencies (f_{Larmor} for ^{31}P @ 5T = 86MHz), we are more interested in the input signal voltage than the input signal power. Therefore, more interestingly, the voltage seen at the receiver input for the new approach, without the impedance transform and the input match, V_2 is given by (3.10).

$$V_2 = Q\varepsilon_{coil} = 2\sqrt{\frac{R_P}{Z_0}}V_1 \tag{3.10}$$

We note that the signal is "voltage-boosted" by two times the ratio of the square-root of R_P/Z_0, which for our prototype design equals to 19dB. This is critical as it allows us to completely eliminate an active LNA stage in our prototype which is important in our power limited environment of an implantable system. However, it is important to note that there is no power gain in the passive network, there is only a voltage gain associated

with avoiding the matching network. The resulting voltage boost for our prototype design with and without the transmission line and matching networks is shown in Fig. 3.12. We see 19dB difference in the signal amplitude at the peak at 86MHz.

3.3.1 Coil Test

Theoretically, the passive multiplication is obtained at the coil from the close distance between the sensor and the sample. We confirmed these benefits from the real coil test as shown in Fig. 3.13(a). The coil placed at the center is a transmitter coil and the other two coils are receiver coils. The leftmost receiver coil has no matching network and the other one has a matching network. All coils are aligned with the same axis. Each receiver coil has the same distance away from the transmitter coil to experience same magnetic field. In the test, transmitter coil is sending a sinusoidal signal at RF frequencies (f_{Larmor} for ^{31}P @ 5T = 86MHz). The other two coils are receiving this signal. As we expected, Fig. 3.13(b) shows that a higher signal level is picked up at the coil with no matching network than at the coil with matching network. Left one was measured with a high impedance scope probe while right one was measured with a 50Ω scope input.

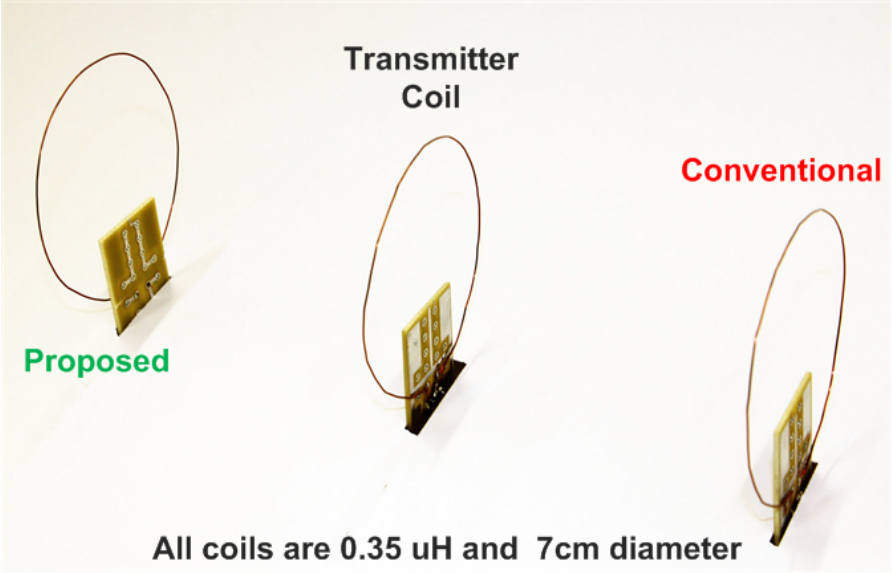

(a) Coil test setup

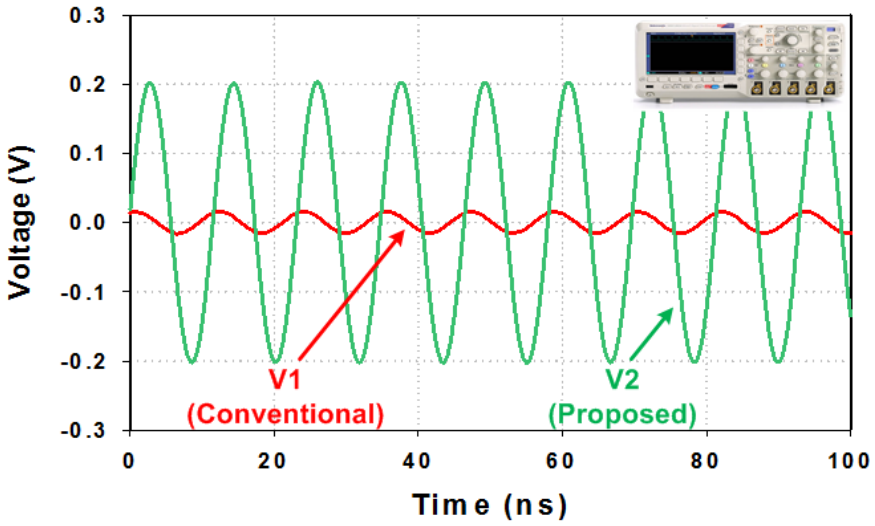

(b) Measurement results

Figure 3.13: Coil test setup for tradition vs. new approach

Chapter 4

Circuit and Architecture

In a step towards realizing a fully-integrated low-power NMR transceiver, we designed three different chips. The first chip, in Fig. 4.1, was primarily designed for measuring the ^{31}P spectrum from an ATP sample at 5T. It has just a LNA-mixer hybrid circuit and an integer-N type frequency synthesizer that makes the Larmor frequency ($\sim$ 86MHz) for phosphorus (^{31}P). The down converted NMR signal is fed into external ADCs in a digtal oscilloscope for signal processing. The digital oscilloscope stores the digitized data and MatLab® represents the NMR spectrum through the fast fourier transform (FFT). For self signal processing, an 1-bit 2nd order sigma delta ADC was implemented in the second chip shown in in Fig. 4.2. Like the first chip, it was designed for detecting phosphorus from ATP samples. In the third chip, a one-stage LNA with a bandwidth of 5-300MHz was added to sense various chemicals. Because of the wide range of Larmor frequency, fractional-N type frequency synthesizer replaced previous integer-N type. In

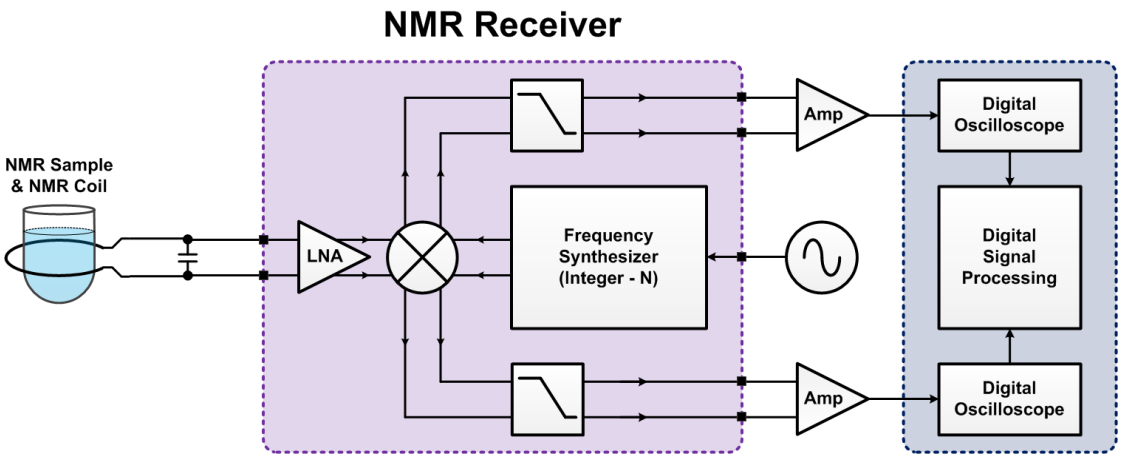

Figure 4.1: Block diagram of NMR Receiver in the first chip

the first and second chips, the 90 degree RF B_1 pulse was generated from an external coil. However, without using external 90 degree RF B1 field, the TX power amplifier was implemented in the third chip. Its simplified NMR transceiver block diagram is shown in Fig. 4.3. In this chapter, we will analyze the LNA-mixer hybrid circuit used in the first and second chip. Also the one stage LNA and double balanced I/Q mixer in the third chip will be reviewed.

4.1 Low Noise Amplifier (LNA) - Mixer Hybrid

The NMR signal picked up at the NMR coil is fed into the LNA. The LNA amplifies the NMR signal and tries to maintain the SNR without adding noise. But, inherently MOSFET devices have flicker noise (called $1/f$ noise) that generated from the interface between the gate oxide and the silicon substrate and thermal noise that generated from the channel resistance. One-sided power spectral density of these types of noise are

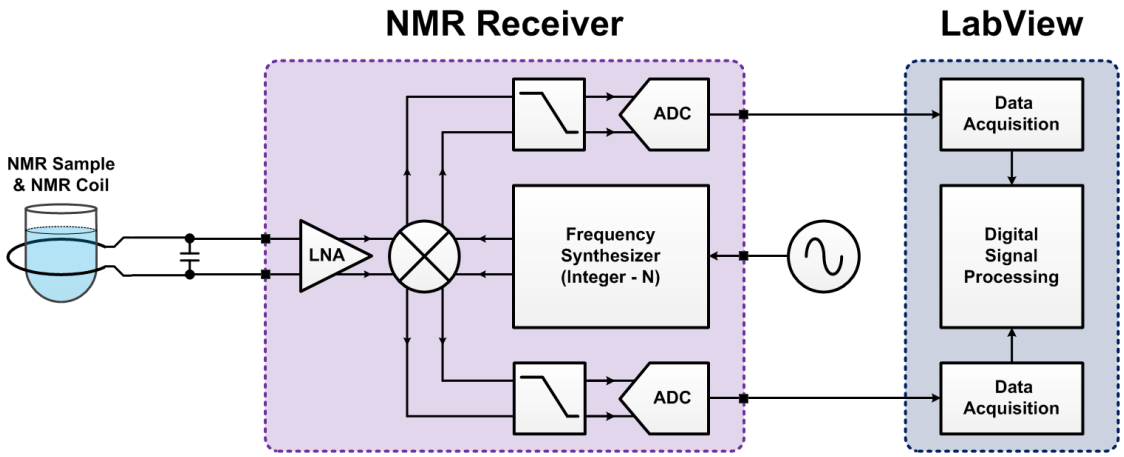

Figure 4.2: Block diagram of NMR Receiver in the second chip

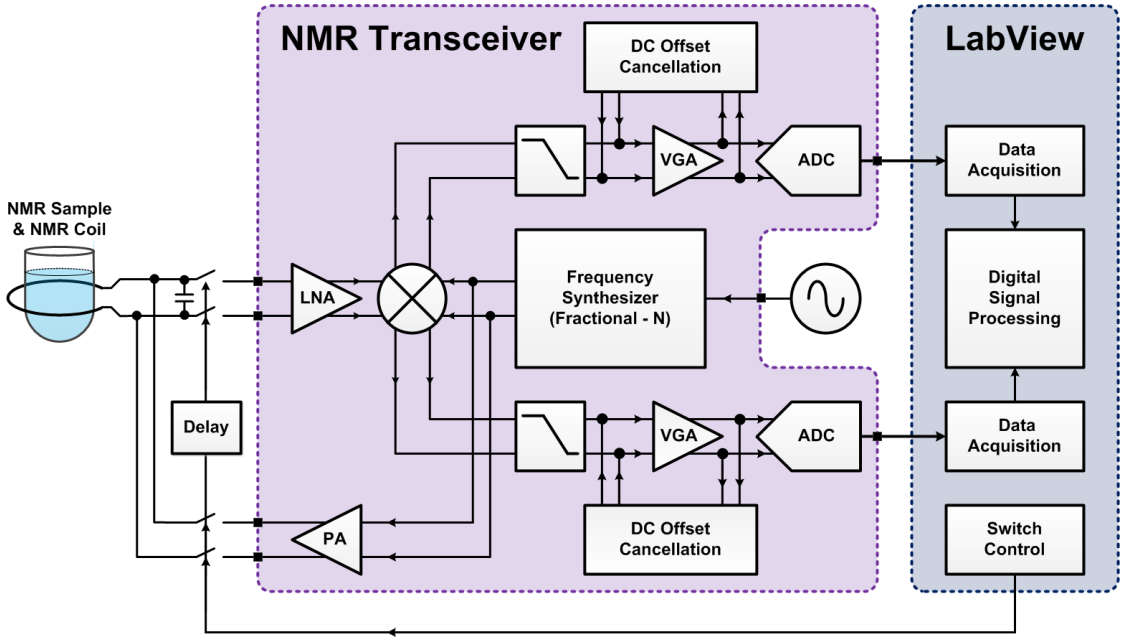

Figure 4.3: Block diagram of NMR Transceiver in the third chip

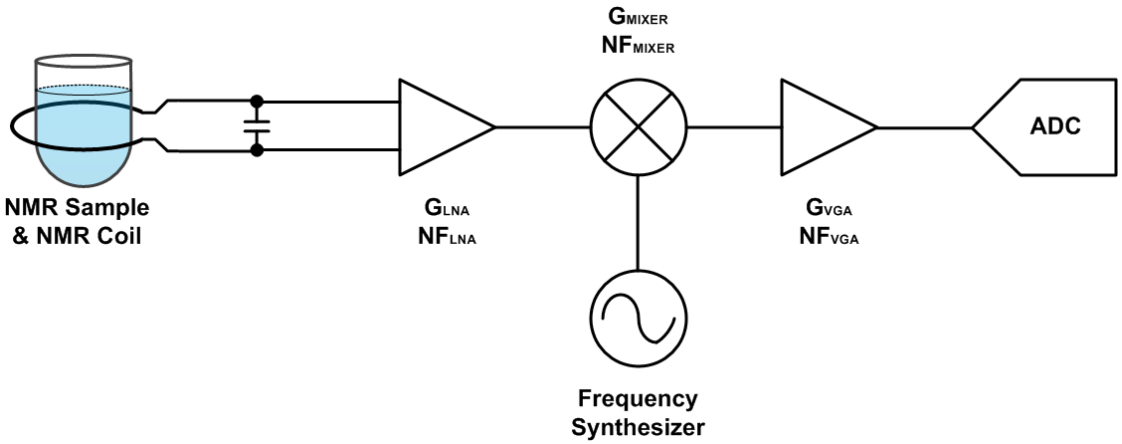

Figure 4.4: Simplified receiver chain for noise figure analysis

simply expressed as

$$\overline{V_{flicker}^2} = \frac{K}{C_{ox}WL} \cdot \frac{1}{f} \tag{4.1}$$

$$\overline{V_{thermal}^2} = 4k_0T\gamma\frac{1}{g_m} \tag{4.2}$$

where K is a process-dependent constant on the order of about 10^{-25} V^2F and C_{ox} is the gate oxide capacitance per unit area. The power spectral density of flicker noise is inversely proportional to the frequency. Thermal noise is also inversely proportional to the transconductance of the MOSFET. According to Eq. (4.1) and (4.2), increasing the size of the MOSFET helps reduce the noise effect because the channel resistance will decrease at a fixed current source.

Considering the receiver system performance, we must calculate the noise figure (NF) of the overall system as well as the noise performance from individual blocks. The simplified receiver chain is shown in Fig. 4.4. The total noise figure of the receiver

($NF_{receiver}$) is given by

$$NF_{receiver} = NF_{LNA} + \frac{NF_{MIXER} - 1}{G_{LNA}} + \frac{NF_{VGA} - 1}{G_{LNA} \cdot G_{MIXER}} \tag{4.3}$$

where G_{LNA} and NF_{LNA} are the gain and the noise figure of the LNA, G_{MIXER} and NF_{MIXER} are the conversion gain and the noise figure of the mixer and NF_{VGA} is the noise figure of the VGA. As we know, the receiver noise performance primarily depends on the noise figure of LNA because the LNA has gain which desensitizes the noise impact from the following blocks (Mixer and VGA). Previously, we analyzed the typical matching networks used in modern RF circuits. In the case of the non-matched coil, there is a passive voltage gain at resonance. This gain is equal to the quality factor (Q_{coil}) of the NMR receiver coil. Here we can modify Eq. (4.3) as

$$NF_{receiver} = NF_{coil} + \frac{NF_{LNA} - 1}{G_{coil}} + \frac{NF_{Mixer} - 1}{G_{coil} \cdot G_{LNA}} + \cdots \tag{4.4}$$

$$= 1 + \frac{NF_{LNA} - 1}{Q_{coil}} + \frac{NF_{Mixer} - 1}{Q_{coil} \cdot G_{LNA}} + \cdots \tag{4.5}$$

where Q_{coil} is the quality factor of the coil at resonance. The noise figure of the NMR coil is 1 (= 0dB) because the thermal noise from the series resistance of the coil is multiplied by Q_{coil} without adding additional noise. Therefore, the transfer functions of the NMR signal and thermal noise are the same at the coil. If the quality factor of the coil increases, the receiver noise figure improves [11, 19].

Based on this result Eq. (4.5) , we designed a LNA-Mixer hybrid circuit (there is no actual LNA circuit) in the first and second chips. When the external NMR coil with high quality factor is used, it reduces the noise by Q_{coil}, which is inherently about 50.

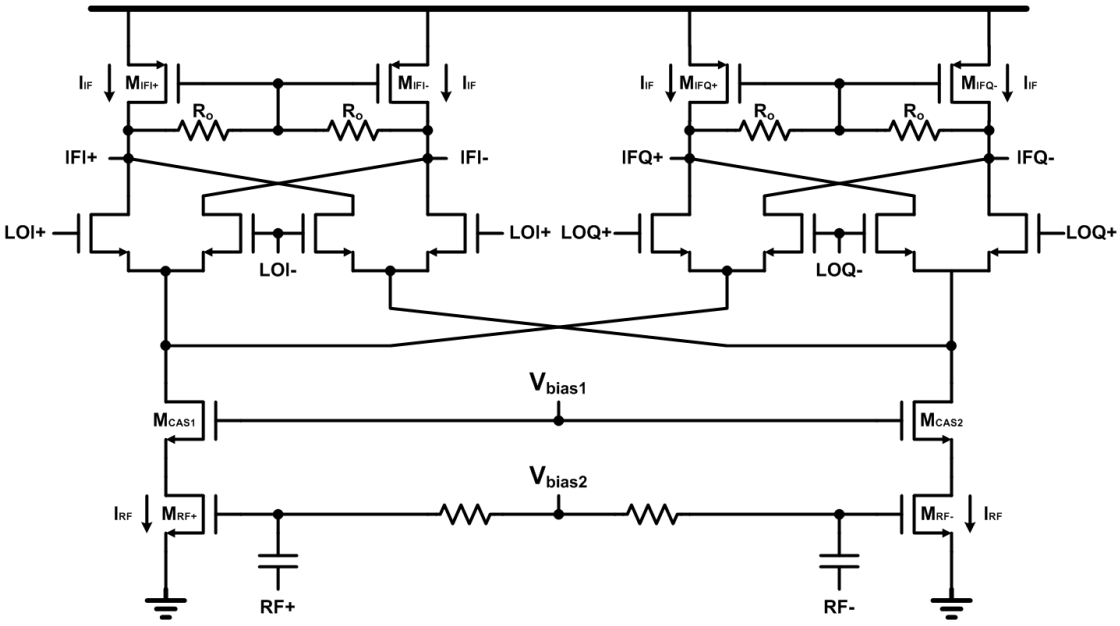

Figure 4.5: Simplified LNA-Mixer hybrid circuit

So, we can skip the one-stage LNA circuit before the mixer. The LNA-mixer hybrid circuit is shown in Fig. 4.5. It is a normal double balanced quadrature mixer [20].

In this LNA-Mixer hybrid circuit, the NMR signal at resonance in the coil drives the RF input transistors (M_{RF+}, M_{RF-}) at the bottom. Cascode transistors (M_{CAS1}, M_{CAS2}) are used for reducing current mismatch and blocking LO signal leakage from the LO inputs to the RF inputs. This LO signal leakage makes the output voltage saturate to desensitize the RF input signals because typically LO signals are generated by strong buffers to make it a rectangular pulse for reducing the noise figure. Output nodes are self-biased with the diode connection. This can easily set a stable and accurate output common mode output voltage without the aid of additional common mode feedback circuits that needs extra power. The conversion gain from RF to IF is easily determined

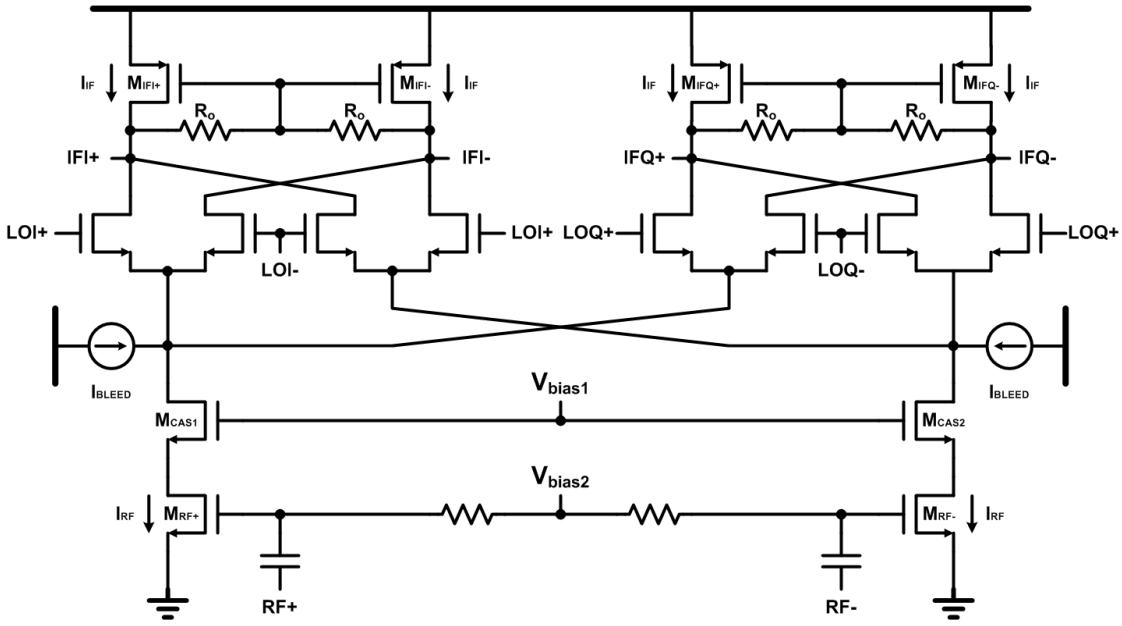

Figure 4.6: Simplified LNA-Mixer hybrid circuit with current bleeding

by the ratio of input and output transconductance in this circuit. The conversion gain is expressed as

$$Conversion\ Gain = \frac{2}{\pi} \cdot \frac{g_{RF}}{g_0} \tag{4.6}$$

$$= \frac{2}{\pi} \cdot \frac{\sqrt{2\mu_n C_{ox} \left(\frac{W}{L}\right)_n I_{RF}}}{g_0} \tag{4.7}$$

$$g_0 = \frac{1}{R_0} \tag{4.8}$$

$$I_{RF} = 2 \cdot I_{IF} \tag{4.9}$$

To increase the conversion gain, we need to increase the transconductance of input transistors or increase the output resistance (R_0), assuming that R_0 is smaller than the output impedance of the load transistors. When the bias current is fixed, sizing input transistors can easily change the conversion gain. Increasing the size of input

transistors, obviously transconductance will increase but the parasitic capacitance will also increase. This would be a heavy load for the coil. To reduce the loading effect from the parasitics, bigger bypass capacitor will be needed. We can increase the output resistance R_0. Maximum limit is determined by the output impedance of the output transistor. To increase this value, a longer length or small current are needed. When the size of output transistors drawing a fixed current is getting small, the over-drive voltage of output transistors increases and the output swing decreases. There is a special way to fix this problem [21, 22]. In Fig. 4.6, extra current bleeding sources are added to the common source node for LO differential inputs. The conversion gain is then expressed as

$$Conversion\ Gain = \frac{2}{\pi} \cdot \frac{g_{RF}}{g_0} \tag{4.10}$$

$$= \frac{2}{\pi} \cdot \frac{\sqrt{2\mu_n C_{ox} \left(\frac{W}{L}\right)_n I_{RF}}}{g_0} \tag{4.11}$$

$$g_0 = \frac{1}{R_0} \tag{4.12}$$

$$I_{RF} = 2 \cdot I_{IF} + I_{BLEED} \tag{4.13}$$

Typically I_{BLEED} takes 80 - 90 % of I_{RF} and I_{IF} just consumes 5 - 10 % of I_{RF}. Therefore, the transconductance of the output transistors is getting smaller and the conversion gain increases. Also the over-drive voltage of the output transistors reduces and the output voltage swing increases. Even though the added current sources are helpful for the conversion gain and the output swing, they have the noise. However, as mentioned earlier, the total noise figure is not getting degraded severely because the high

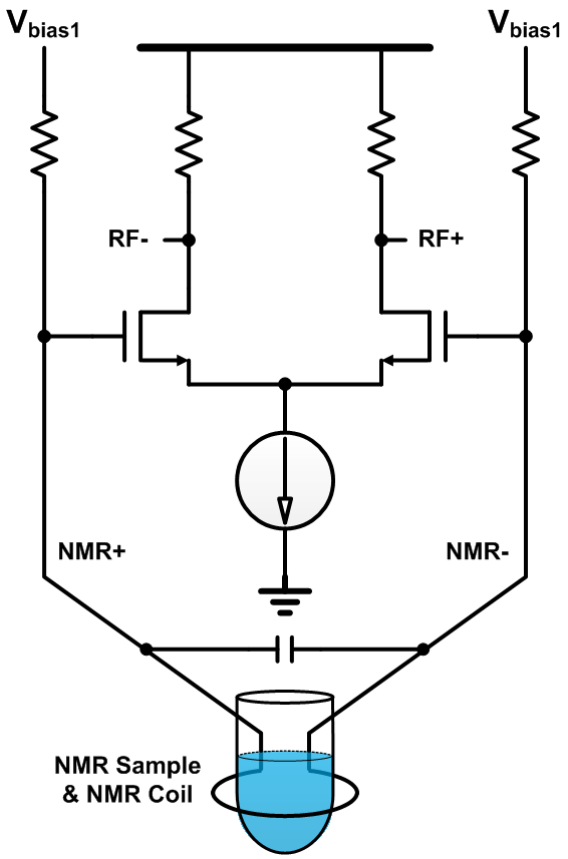

Figure 4.7: Simplified LNA Circuit

quality factor of the NMR coil will desensitize the noise effect from additional current sources. In fact, the mixer has inherently high noise figure ($>$ 10dB) because the flicker and thermal noise from the RF tail current source around the harmonic frequencies of LO frequency. In mixer design, LO signal as close to a rectangular pulse as possible reduces the flicker and thermal noise from LO input transistors. Specially, it is helpful to put the bias point of the switching as close as to the devices triode region to make the LO signal rectangular. More detail analysis on mixer design have been done in [23, 24].

In the third chip, we added the one stage LNA (in shown Fig. 4.7) to provide wide dynamic range. In fact, the proton (^{1}H) or the phosphorus (^{31}P) that has high abundance in nature (in other words, they are well ionized in the natural state) have much higher amplitude than other chemicals (Carbon or Florine) that have relatively low abundance. It is so difficult to detect chemicals having low amplitude that the additional LNA will reduce the minimum signal level detectable (in other words, to increase the sensitivity).

In Fig. 4.8, the source degenerated LNA (SD LNA) that is used in conventional RF circuits and the proposed simple differential LNA are shown. The SD LNA has two inductors (L_g and L_s) for impedance matching (typically 50Ω). The input impedance seen from the RF port is expressed as

$$Z_{in}(s) = sL_g + \frac{1}{sC_{gs}} + (1 + \beta(s))\, sL_s \tag{4.14}$$

$$= sL_g + \frac{1}{sC_{gs}} + \left(1 + \frac{g_m}{sC_{gs}}\right) sL_s \tag{4.15}$$

$$= s(L_g + L_s) + \frac{1}{sC_{gs}} + \frac{g_m L_s}{C_{gs}} \tag{4.16}$$

$$\beta(s) = \frac{g_m}{sC_{gs}} \tag{4.17}$$

$$Z_{in}(s) \mid_{s=j\omega_0} = \frac{g_m L_s}{C_{gs}} \tag{4.18}$$

$$\omega_0 = \frac{1}{\sqrt{(L_g + L_s)C_{gs}}} \tag{4.19}$$

where $\beta(s)$ is the current gain of MOSFET similar to that of the bipolar junction transistor (BJT). For the impedance matching, $\frac{g_m L_s}{C_{gs}}$ is the real impedance equivalent to 50Ω at the resonance frequency ($\omega_0 = \frac{1}{\sqrt{(L_g+L_s)C_{gs}}}$). Without using any passive resistors, just combination of an inductor and a transistor can make real impedance. Therefore, low

noise figure is obtained. This is the reason why this LNA is commonly used in RF circuits. Other than its low noise figure, this type of LNA is not efficient. First, this circuit is only valid for narrow band (around the resonance frequency) not wide band. Second, it needs impedance matching to 50Ω but our receiver uses the passive multiplication of the NMR coil resonance to avoid signal voltage loss from 50Ω impedance matching since the NMR receiver is right next to the sample. Third, two inductors (L_g and L_s) occupy big area, compared with the active circuit . Because of these problems., we proposed a simple differential CML type LNA to cover the frequency range from 5MHz to 300MHz. 5MHz comes from the gyro-magnetic ratio of the carbon (10.705MHz/T) at 0.5T. 300MHz comes from the gyro-magnetic ratio of the proton (42.576MHz/T) at 5T. Large transistors are used for minimizing the flicker noise and thermal noise from channel resistance at the strong inversion. Larger transconductance (larger current) means less thermal noise . To obtain flat and large voltage gain up to 300MHz, pure small resistive loads (differential 500Ω) are used instead of PMOS active loads and large current is used to compensate gain drop from a small resistor. Power consumption in this LNA is not avoidable for low noise and high gain. Bandwidth is simply determined by the resistor and total capacitance at output node. In the design requirement of the third chip, the width of the total input transistors are 980μm. It has a voltage gain of 18 dB within the bandwidth of interest and consumes 4 mA from a 1.5 V supply. The input referred thermal noise voltage is 1.8 nV/$\sqrt{Hz}$.

Next, we will revisit and summarize the LNA-Mixer hybrid circuit that is used in the

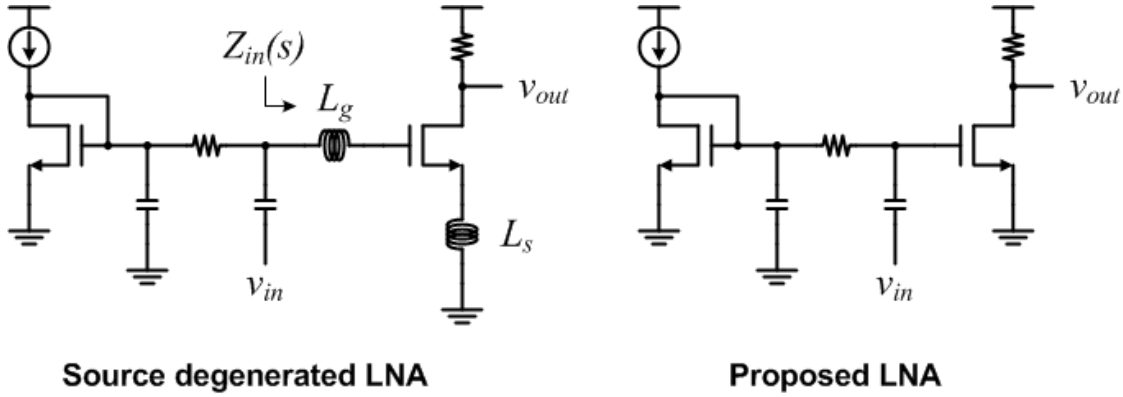

Figure 4.8: LNA Comparison

third chip. The amplified NMR signal from the LNA experiences down conversion from mixer. Cascode transistors shield the RF inputs (equivalent to the LNA output) from mixer local oscillator (LO) leakage. For reducing power consumption and improving I/Q mismatch, I and Q channels of the mixer share the RF transconductor current. This double balanced quadrature mixer down-converts the RF to a 10 KHz intermediate frequency (IF) for the next signal processing blocks. The IF frequency is selected to avoid 1/f noise issues. The LO signal with the IF frequency difference from the RF is generated from an on-chip phase locked loop (PLL). Because various NMR chemicals are of interest, a fractional type frequency synthesizer is preferred. This frequency synthesizer will be reviewed later. As well as resistively-loaded diode-connected PMOS loads with parallel capacitors providing a 100 KHz low-pass response, current bleeding to the RF transconductors provides high IF voltage gain and wider voltage swing at the IF output. The bleeding current takes 80 - 90% of RF tail currents. This mixer is designed for an RF-to-IF signal conversion gain of 22dB and draws 400uA current.

4.2 Variable Gain Amplifier (VGA)

Typically the induced NMR signal value at the coil is about tens of nanovolts [11]. In fact, the induced NMR signal voltage level can have a large range as discussed in Eq. (2.40) in that it depends on the magnetic field strength (B_0), volume density (V_s), Larmor frequency (ω_0), filling factor (η), the gyro-magnetic ratio (γ) and the spin angular momentum quantum number of the sample. However, we ignored the NMR coil characteristic and the inhomogeneity of B_0 and B_1. The inhomogeneity will be reduced by the special magnetic field calibration procedure, called shimming process. Modern NMR systems has their own special shimming coils inside the static magnet. However, in the proposed portable and implantable NMR systems, we assume that there are no shimming coils at this time. We have to consider the NMR signal voltage loss from them. So we estimated that the induced NMR signal is much lower than expected. Even though this NMR signal is amplified properly through the LNA and Mixer, the signal voltage level might not be enough because it has less voltage gain if the resonance frequency of the coil, with high Q, is shifted away from the Larmor frequency. An additional IF voltage gain amplifier (VGA) block compensates this signal voltage loss and increases the voltage level to maximize SNR at the input of the ADC. This allows us to measure the low level signals of chemicals having low abundance. This is the reason why we need a programmable gain block in the receiver path.

There are several types of VGAs with continuous and discontinuous gain ranges. Here we choose the simple folded cascode differential amplifiers with discrete gain step

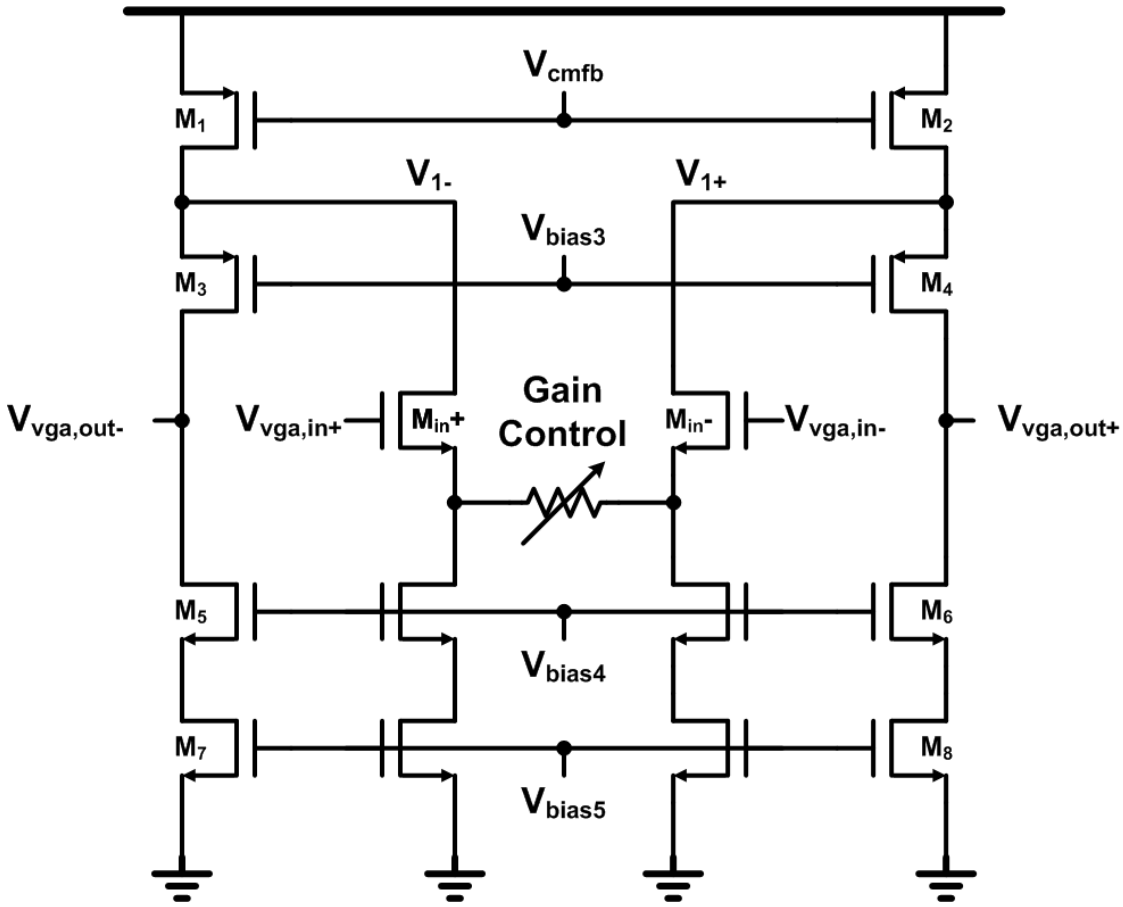

Figure 4.9: Simple folded cascode amplifier

(shown in Fig. 4.9) for this application. In this topology, the maximum gain (A_{max}) is expressed as

$$A_{max} = g_{m,in} R_{out} \tag{4.20}$$

$$R_{out} = R_{outp} \parallel R_{outn} \tag{4.21}$$

$$R_{outp} \simeq g_{m3} r_{o3} r_{o1} \tag{4.22}$$

$$R_{outn} \simeq g_{m5} r_{o5} r_{o7} \tag{4.23}$$

This maximum gain is reduced by adding the resistance at source node. The gain with resistance is expressed as

$$A = \frac{g_{m,in}}{1 + g_{m,in} R_s} R_{out} \tag{4.24}$$

where R_s is the variable resistance. When R_s is 0 Ω, the gain is the maximum. The larger R_s, the smaller the gain. Discrete variable gain steps are obtained by switching the resistor tree at the common source node of input transistors. Because this operational amplifier is fully differential, a common mode feed back circuit is needed for a stable bias point. In modern CMOS process, the maximum gain ($\sim g_m r_o$) of one stage is around 20 to 30. So the maximum gain ($\sim (g_m r_o)^2$) of a folded-cascode amplifier can be roughly 600 ($\sim$ 55dB). In our receiver, we choose 40dB maximum gain from one folded cascode amplifier. For more gain, each channel has two amplifiers in series with DC offset cancellation. Because the VGA has 80 dB maximum gain, the output of VGA will saturates for even small input offsets. To minimize this offset and mismatch, we used wider and longer transistors at the inputs. Also, each operational amplifier has its own DC offset calibration block utilizing low frequency negative feedback from the output to

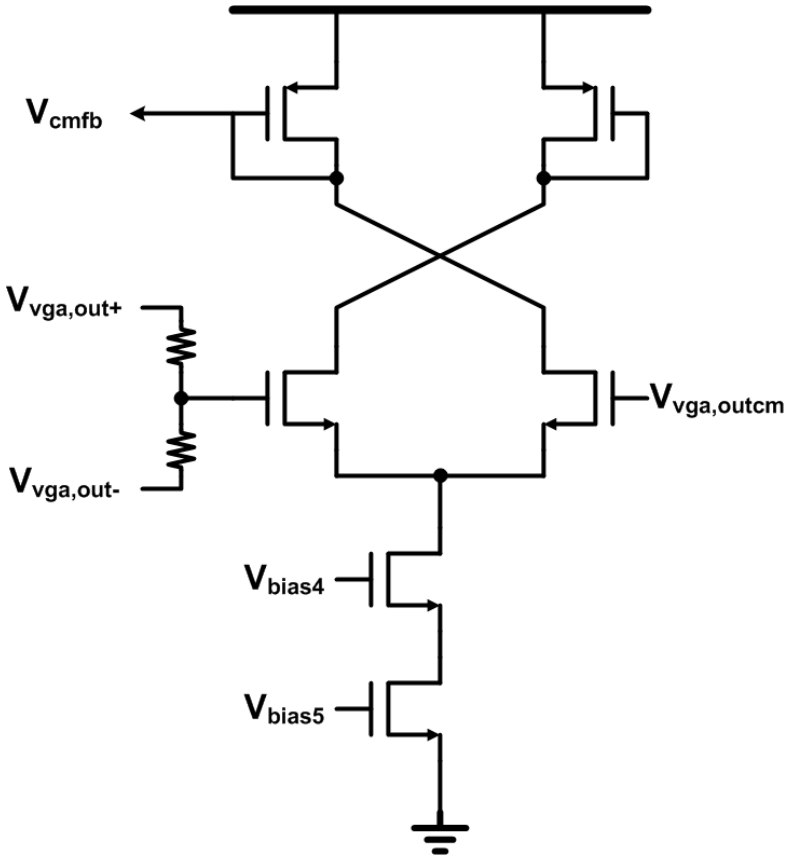

Figure 4.10: Common mode feedback circuit for simple folded cascode amplifier

the input. Therefore, the VGA block provides a total of five discrete gain steps, for a total receiver gain that varies between 26dB to 80dB, to accommodate a wide range of input signal levels.

4.3 Sigma Delta ADC

Through two stage VGAs, the properly amplified signals arrive at the ADC blocks which digitizes the NMR signals to facilitate further digital signal processing. There are many options to choose from for the ADC types. Here we choose an oversampling ADC using sigma delta modulation because just increasing sampling frequency can provides higher SNR even with 2 quantization levels. This ADC design is based on switched capacitor circuit since the process variation of capacitors is much smaller that of resistors. Typically the switch capacitor circuit uses the ratio of capacitors to obtain the closed loop gain. This is the reason why switched capacitor based ADC has better device matching. But we need to use well-defined capacitors (Metal-Insulator-Metal) and a well-defined clock. Recently, sigma delta ADCs are commonly used in low frequency high SNR applications. In this chapter, we will look at the sigma delta ADC in detail.

First, let's move to the quantization noise and oversampling. If we quantize the full scale voltage V_{FS} with N-bits, the unit difference (Δ) corresponding to the LSB size, is

given by

$$\Delta = \frac{V_{FS}}{2^N - 1} \simeq \frac{V_{FS}}{2^N} \tag{4.25}$$

Fig. 4.11 shows the quantized output according to the input and the quantization error, the difference between the input and the output. As shown in Fig. 4.11, this quantization error is bounded to $\pm\Delta/2$. If the quantization error is random and evenly distributed within this bound, the power of the quantization error (P_Q) is expressed as

$$P_Q = \frac{1}{\Delta}\int_{-\frac{\Delta}{2}}^{+\frac{\Delta}{2}} x^2 dx = \frac{\Delta^2}{12} \tag{4.26}$$

From this equation,we can see that the total quantization noise power is determined by only the quantization level not the sampling frequency. To calculate SNR (Signal-to-Noise Ratio) from the quantization procedure, if a sinusoidal signal with V_{FS} peak to peak voltage is applied to this quantizer, the average signal power (P_S) is

$$P_S = \frac{\left(\frac{V_{FS}}{2}\right)^2}{2} = \frac{(2^N\Delta)^2}{8} \tag{4.27}$$

Therefore, according to Eq. (4.26) and Eq. (4.27), SNR is given by

$$SNR = \frac{P_S}{P_Q} = 3 \cdot 2^{2N-1} \tag{4.28}$$

$$SNR_{dB} = \left(\frac{P_S}{P_Q}\right)_{dB} = 6.02N + 1.76 \tag{4.29}$$

Eg. (4.29) shows that SNR increases by 6 dB for every bit added to the quantizer.

In general, the quantization error is not correlated to the input signal and is approximately assumed to be random white noise [25]. Based on this characteristics, we can

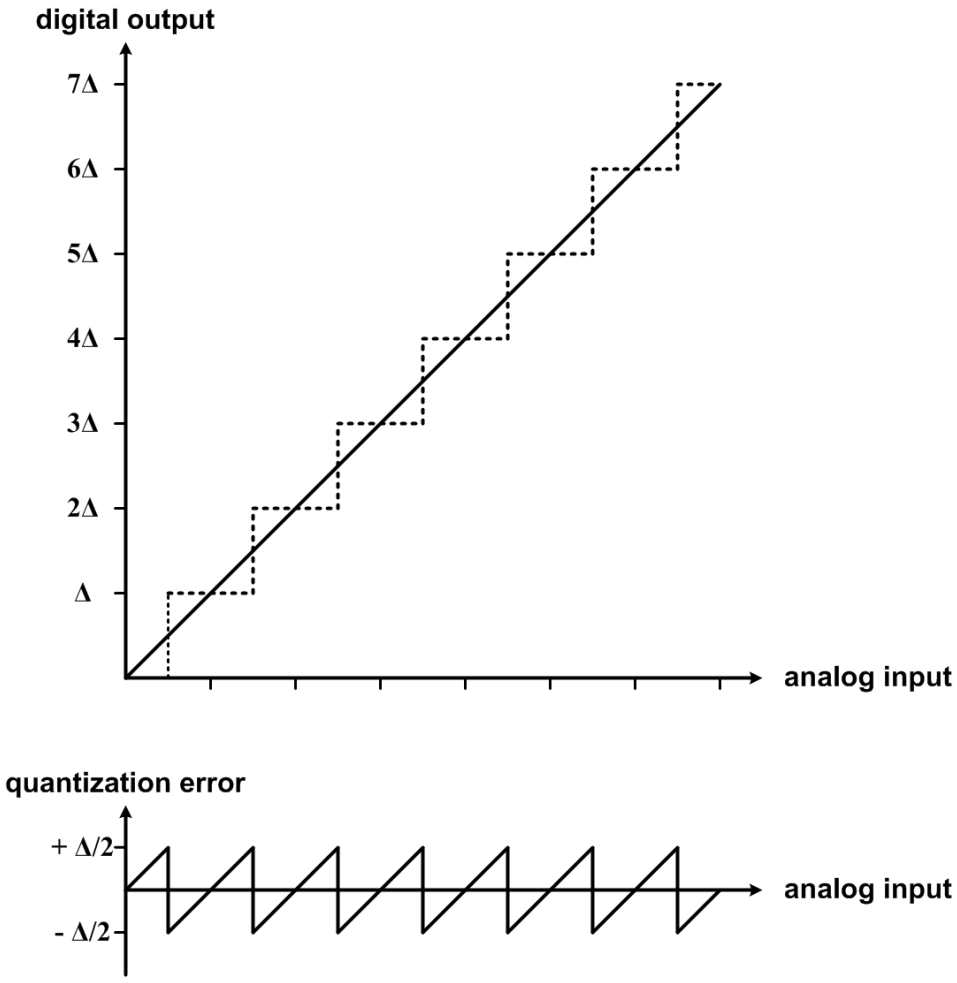

Figure 4.11: Quantization and quantization error for 3-bit ADC

replace the non-linearity from the quantization with a stochastically linear system. The power spectral density for the quantization error, assumed to be white noise, can be expressed as

$$S_{QN}(f) = \frac{P_Q}{f_s} = \frac{\frac{\Delta^2}{12}}{f_s} \tag{4.30}$$

from the sampling process. If the input signal frequency is band-limited to $\pm f_0$, the total quantization noise power with this bandwidth is

$$P_{QN} = \int_{-f_0}^{+f_0} S_{QN}(f)df = \frac{\frac{\Delta^2}{12}}{f_s} \cdot 2f_0 = \frac{1}{OSR} \cdot \frac{\Delta^2}{12} \tag{4.31}$$

where OSR is the oversampling ratio and is defined as

$$OSR = \frac{\frac{f_s}{2}}{f_0} \tag{4.32}$$

Note that even though we increase the oversampling ratio or the sampling frequency (f_s), the quantization noise power in Eq. (4.26) does not change but the quantization noise power within the band in Eq. (4.31) decreases as shown in Fig. 4.12. Now we can recalculate the SNR within $\pm f_0$ for the input signal with the power of P_s.

$$\begin{aligned} SNR_{dB} &= \left(\frac{P_S}{P_{QN}}\right)_{dB} \\ &= 10\log\left(\frac{P_s}{\frac{1}{OSR} \cdot \frac{\Delta^2}{12}}\right) \\ &= 10\log\left(\frac{P_s}{\frac{\Delta^2}{12}}\right) + 10\log(OSR) \end{aligned} \tag{4.33}$$

From Eq. (4.33), as the sampling frequency or the oversampling frequency increases by 2 times, 3 dB improvement in SNR can be obtained. Considering Eq. (4.33), this SNR improvement is equivalent to adding 0.5 bit to the quantizer. This is a basic concept for

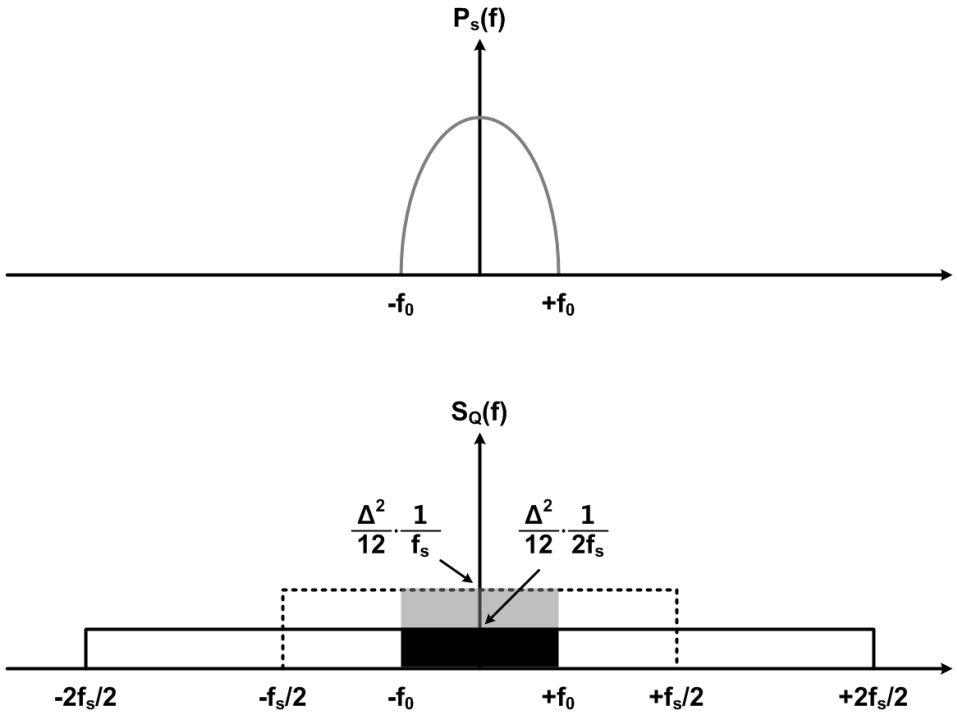

Figure 4.12: Quantization noise reduction from oversampling

oversampling data converters in that we can increase the effective number of bits of the quantizer as we increase the sampling frequency.

Now we move to noise shaping using oversampled sigma delta modulation. According to Eq. (4.33), 3dB SNR improvement (correspond to the increasing of 0.5 effective number of bits) is acquired when the sampling frequency increases by 2X. As well as this oversampling technique for SNR improvement, there is another technique, called noise shaping, to get higher SNR. This function is executed from the sigma delta modulator block shown in Fig. 4.13. This block consists of the filter having the transfer function of $H(z) = V(z)/U(z)$ and the quantizer. The output of the quantizer is used for a negative feedback signal. We use linear modeling to analyze the sigma delta converter because it can be approximated to be independent of the input even though the quantizer is nonlinear. Nonlinear quantizer error is modeled as $E(z)$ and is added with a linear summer.

Calculating transfer functions ($H_S(z)$ and $H_Q(z)$) for the input signal ($X(z)$) and the quantizer error ($E(z)$) in Fig. 4.13

$$H_S(z) = \frac{Y(z)}{X(z)} = \frac{H(z)}{1 + H(z)} \tag{4.34}$$

$$H_Q(z) = \frac{Y(z)}{E(z)} = \frac{1}{1 + H(z)} \tag{4.35}$$

Therefore, the output signal ($Y(z)$) is expressed as

$$Y(z) = H_S(z) \cdot X(z) + H_Q(z) \cdot E(z) \tag{4.36}$$

In Eq. (4.34) and (4.35), if $H(z)$ has the low pass filter characteristic, the transfer

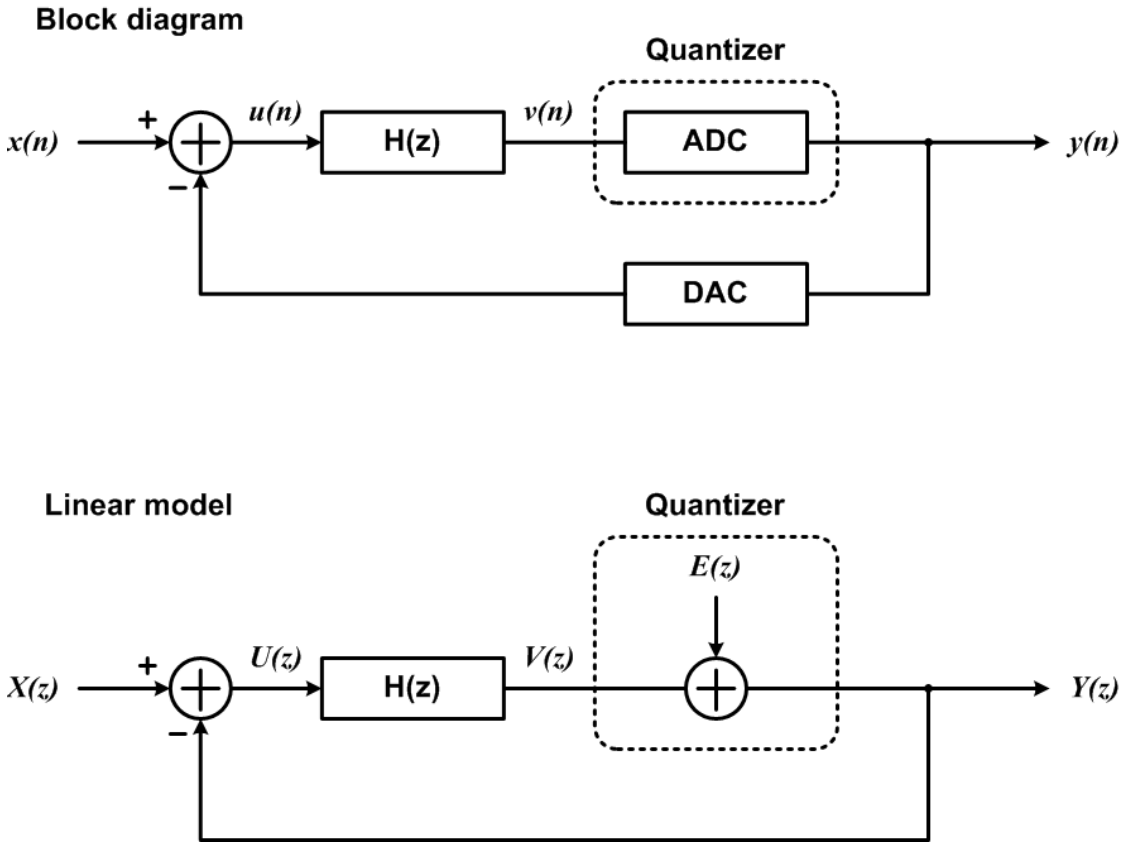

Figure 4.13: Noise shaping

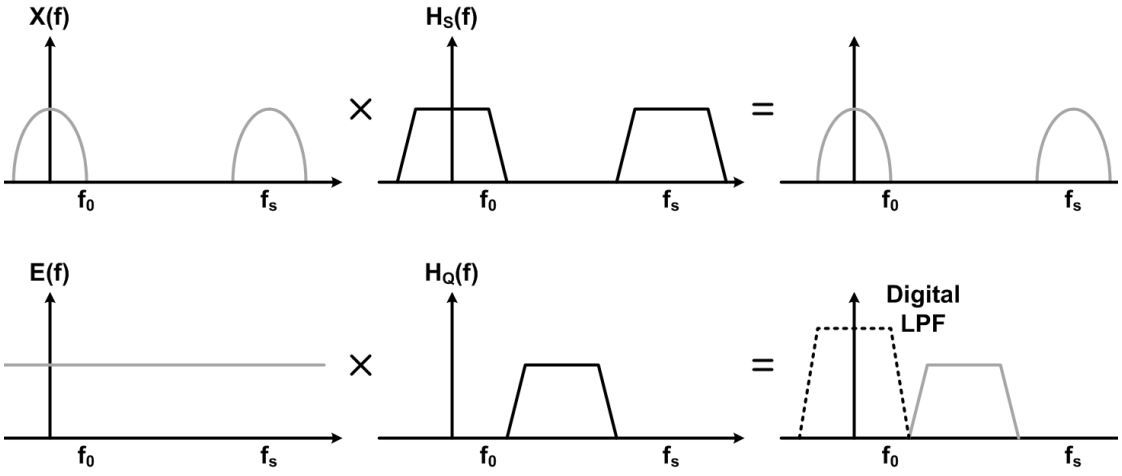

Figure 4.14: Frequency response of sigma delta modulator

function $H_S(z)$ of the input signal also has low pass filter characteristic but transfer function ($H_Q(z)$) of the quantizer error has high pass filter characteristic. Accordingly, the quantization error will increase at high frequency but will decrease within the low frequency signal bandwidth. Frequency response for noise shaping is explained graphically in Fig. 4.14. The input is not affected from the transfer function $H_S(f)$ while the white quantization noise experiences the noise-shaping due to transfer function $H_Q(f)$ in that the quantization noise is shifted and accumulated to high frequency. This high passed quantization noise around $f_s/2$ is reduced or removed though post digital low pass filter processing.

The low pass filter $H(z)$ used in a sigma delta modulation is simply implemented using first order discrete time integrator like below

$$H(z) = \frac{V(z)}{U(z)} = \frac{z^{-1}}{1 - z^{-1}} = \frac{1}{z - 1} \tag{4.37}$$

In the discrete time domain, this integral function is expressed as

$$v(n+1) - v(n) = u(n) \tag{4.38}$$

and the output $y(n)$ is

$$y(n) = x(n-1) + e(n) - e(n-1) \tag{4.39}$$

Using Eq. (4.37), we calculate each transfer function for the signal and the quantization error

$$H_S(z) = \frac{\frac{1}{z-1}}{1 + \frac{1}{z-1}} = z^{-1} \tag{4.40}$$

$$H_Q(z) = \frac{1}{1 + \frac{1}{z-1}} = 1 - z^{-1} \tag{4.41}$$

If we insert these into Eq. (4.36), the result is the same as what we get from Eq. (4.39) in the discrete time domain. As shown in Eq. (4.67) and (4.68), the input signal is one sample delayed at the output and the quantizer error is high pass filtered with first order. After noise shaping with 1st order sigma delta modulator, the power spectral density of the quantization noise is

$$S_N(f) = S_{QN}(f) \mid H_N(z) \mid^2 \tag{4.42}$$

$$= S_{QN}(f) \mid 1 - z^{-1} \mid^2_{at\ z=e^{j2\pi\frac{f}{f_s}}} \tag{4.43}$$

$$= \frac{\Delta^2}{12 f_s} \mid 1 - e^{-j2\pi\frac{f}{f_s}} \mid^2 \tag{4.44}$$

$$= \frac{\Delta^2}{12 f_s} 2^2 \sin^2\left(\frac{\pi f}{f_s}\right) \tag{4.45}$$

In Fig. 4.15, the shaped quantization noise power spectral density is shown. Now we calculate the noise power within the input signal band

$$P_N = \int_{-f_0}^{+f_0} S_{QN}(f) \mid H_N(z) \mid^2 df \tag{4.46}$$

$$= \int_{-f_0}^{+f_0} S_{QN}(f) \mid 1 - z^{-1} \mid^2_{at\ z=e^{j2\pi \frac{f}{f_s}}} df \tag{4.47}$$

$$= \frac{\Delta^2}{12 f_s} \int_{-f_0}^{+f_0} \mid 1 - e^{-j2\pi \frac{f}{f_s}} \mid^2 df \tag{4.48}$$

$$= \frac{\Delta^2}{12 f_s} \int_{-f_0}^{+f_0} 2^2 \sin^2 \left(\frac{\pi f}{f_s} \right) df \tag{4.49}$$

In this equation, if the oversampling frequency is much higher than the input signal band f_0, it can be approximated as

$$P_N \simeq \frac{\Delta^2}{12 f_s} \int_{-f_0}^{+f_0} 2^2 \left(\frac{\pi f}{f_s} \right)^2 df \tag{4.50}$$

$$\simeq \frac{\Delta^2 \pi^2}{36} \left(\frac{2 f_0}{f_s} \right)^3 \tag{4.51}$$

$$\simeq \frac{\Delta^2 \pi^2}{36} \left(\frac{1}{OSR} \right)^3 \tag{4.52}$$

If the oversampling frequency increases 2 times, SNR improves by 9 dB and it is equivalent to the increase of 1.5 bit effective number of bits in quantizer. Based on this analysis, we can get the first order sigma delta modulator shown in Fig. 4.16. The low pass filter $H(z)$ in Eq. (4.37) is simply implemented by switched capacitor integrator. $H(z)$ is given by

$$H(z) = \frac{C_1}{C_2} \cdot \frac{z^{-1}}{1 - z^{-1}} \tag{4.53}$$

and a 1-bit DAC is also implemented by a comparator that switches reference voltages ($+V_{ref}$ and $-V_{ref}$).

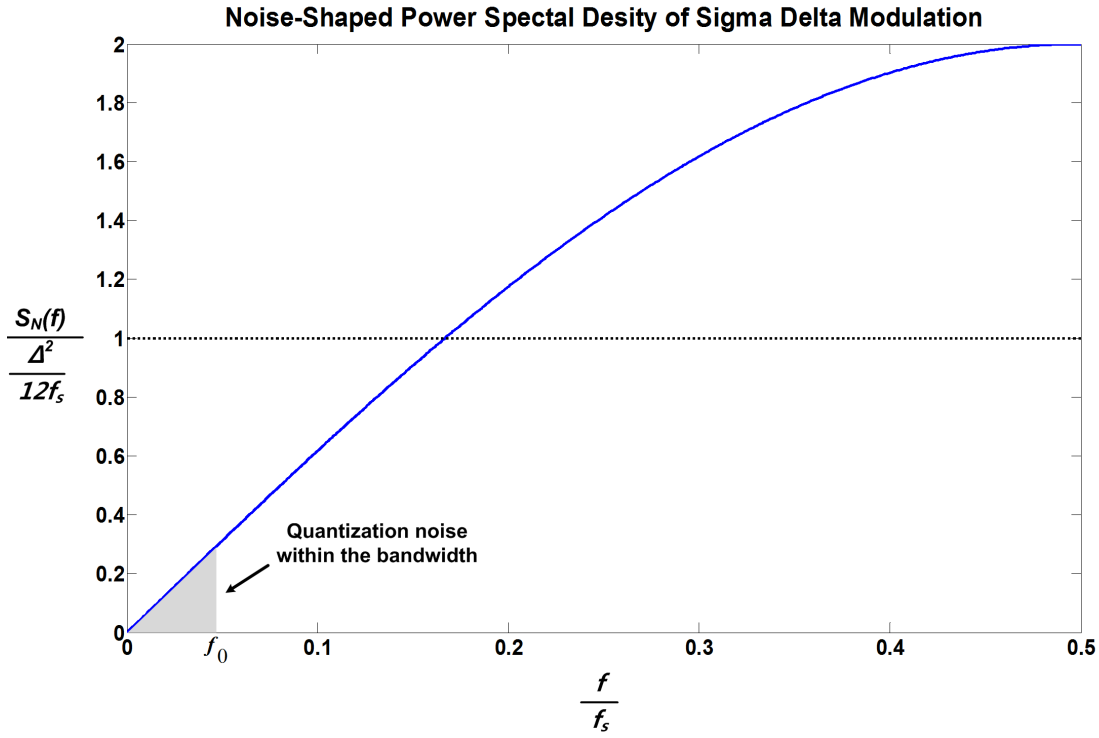

Figure 4.15: Noise shaped power spectral density of first order sigma delta modulator

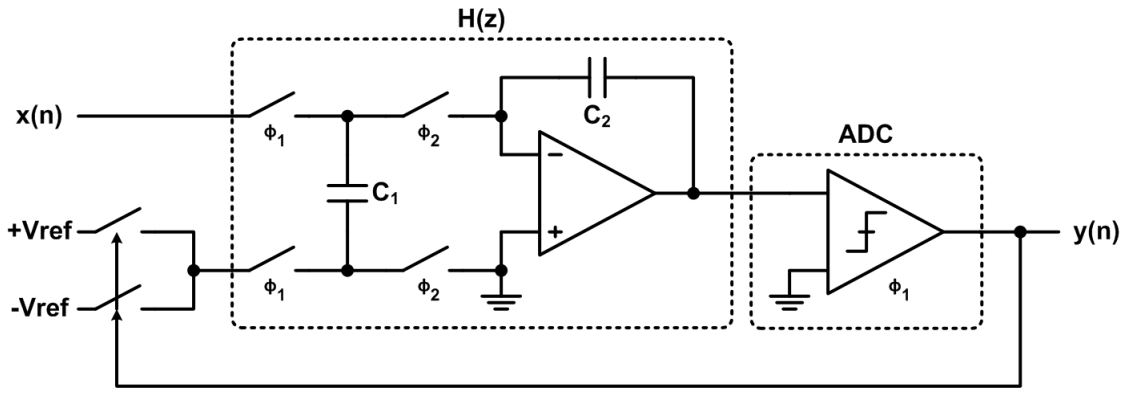

Figure 4.16: Simple first order sigma delta modulator

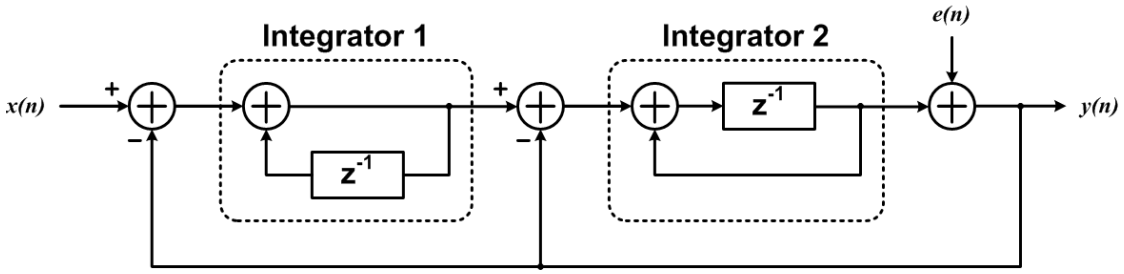

Figure 4.17: Block diagram of the second order sigma delta modulator

Next, we will look at higher order sigma delta modulators. In Eq. (4.35) and (4.36) , the quantization error noise is shaped by the filter $H(z)$ of the sigma delta modulator. The main goal of the sigma delta modulator is shaping the quantization noise and minimizing the quantity of it within the signal band. In Eq. (4.35), the quantizer error included in the feed back signal or output signal is first order shaped but is more efficiently shaped using higher order low pass filters. The output signal $y(n)$ of a second order sigma delta modulator in the Fig. 4.17 is given by

$$y(n) = x(n-1) + e(n) - 2e(n-1) + e(n-2) \tag{4.54}$$

This output signal is fed into the input and is used to modify the next input signal. The quantization noise is shaped with a second order transfer function expressed as

$$H_Q(z) = (1 - z^{-1})^2 \tag{4.55}$$

The total quantization noise power within the signal band is

$$P_N = \int_{-f_0}^{+f_0} S_{QN}(f) \mid H_N(z) \mid^2 df \tag{4.56}$$

$$= \int_{-f_0}^{+f_0} S_{QN}(f) \mid 1 - z^{-1} \mid^4_{at\ z=e^{j2\pi \frac{f}{f_s}}} df \tag{4.57}$$

$$= \frac{\Delta^2}{12 f_s} \int_{-f_0}^{+f_0} \mid 1 - e^{-j2\pi \frac{f}{f_s}} \mid^4 df \tag{4.58}$$

$$= \frac{\Delta^2}{12 f_s} \int_{-f_0}^{+f_0} 2^4 \sin^4 \left(\frac{\pi f}{f_s} \right) df \tag{4.59}$$

$$\simeq \frac{\Delta^2}{12 f_s} \int_{-f_0}^{+f_0} 2^4 \left(\frac{\pi f}{f_s} \right)^4 df \tag{4.60}$$

$$\simeq \frac{\Delta^2 \pi^4}{60 f_s} \left(\frac{1}{OSR} \right)^5 \tag{4.61}$$

In the second order sigma delta modulation, whenever the oversampling frequency increases by 2 times, the total quantization noise power within the band decreases by 15 dB (correspond to the increasing of 2.5 effective number of bits). In general, if the low pass filter $H(z)$ with L-th order is used, the transfer function is

$$H_Q(z) = (1 - z^{-1})^L \tag{4.62}$$

At dc or $z = 1$ there are L zeros. The quantization noise power spectral density with a L-th order sigma delta modulator is

$$S_N(f) = \frac{\Delta^2}{12 f_s} \left[2 \sin \left(\frac{\pi f}{f_s} \right) \right]^{2L} \tag{4.63}$$

and the noise-shaped power spectral density of the quantization noise for different L is shown in Fig. 4.18. As the order of the sigma delta modulator increases, the total quantization noise within the band decreases. From Eq. (4.63), the quantization noise

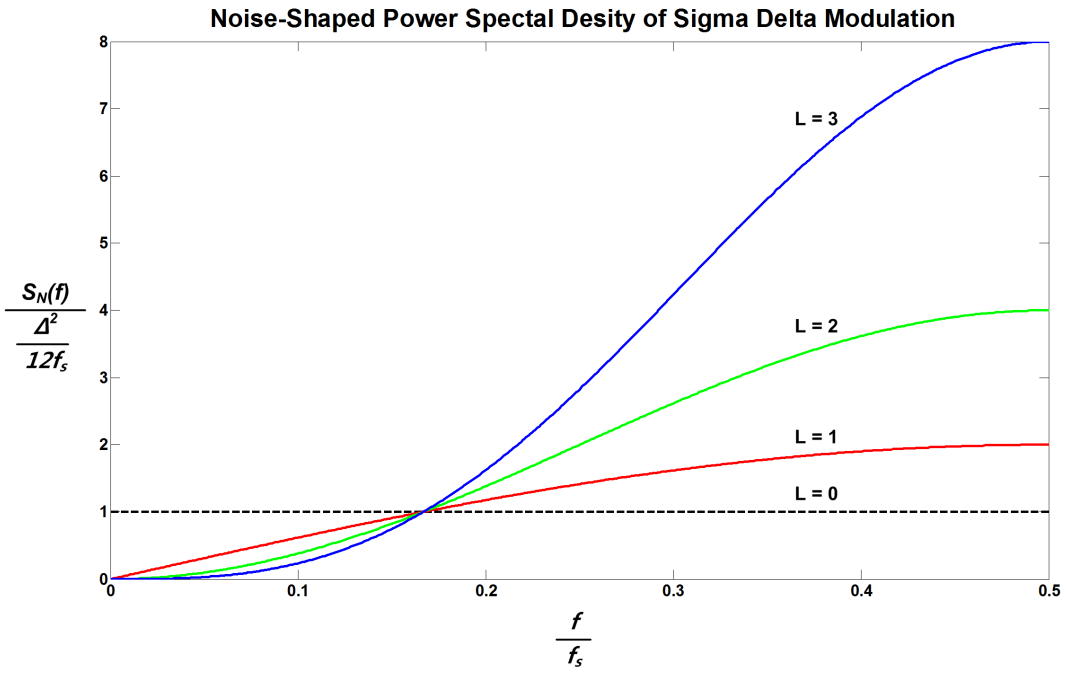

Figure 4.18: Noise shaped power spectral density of L-th order sigma delta modulator

within $\pm f_0$ is given by

$$P_N = \frac{\Delta^2}{12}\frac{\pi^{2L}}{2L+1}\left(\frac{1}{OSR}\right)^{2L+1} \tag{4.64}$$

The relationship between the quantization noise power and the oversampling ratio in Eq. (4.64) is graphically shown in Fig. 4.19. As the sampling frequency or OSR increases by 2 times, SNR improves by $3(2L+1)$ dB. It is equivalent to the increase of $0.5(2L+1)$ effective number of bits in quantizer.

Up to now, we have analyzed the SNR improvement from oversampling and sigma delta modulation. In fact, the noise floor is much more important than SNR in spectroscopy applications. Even though the total receiver SNR is below 0dB, the system function is fine as a spectrometer if the frequency components of interest are distin-

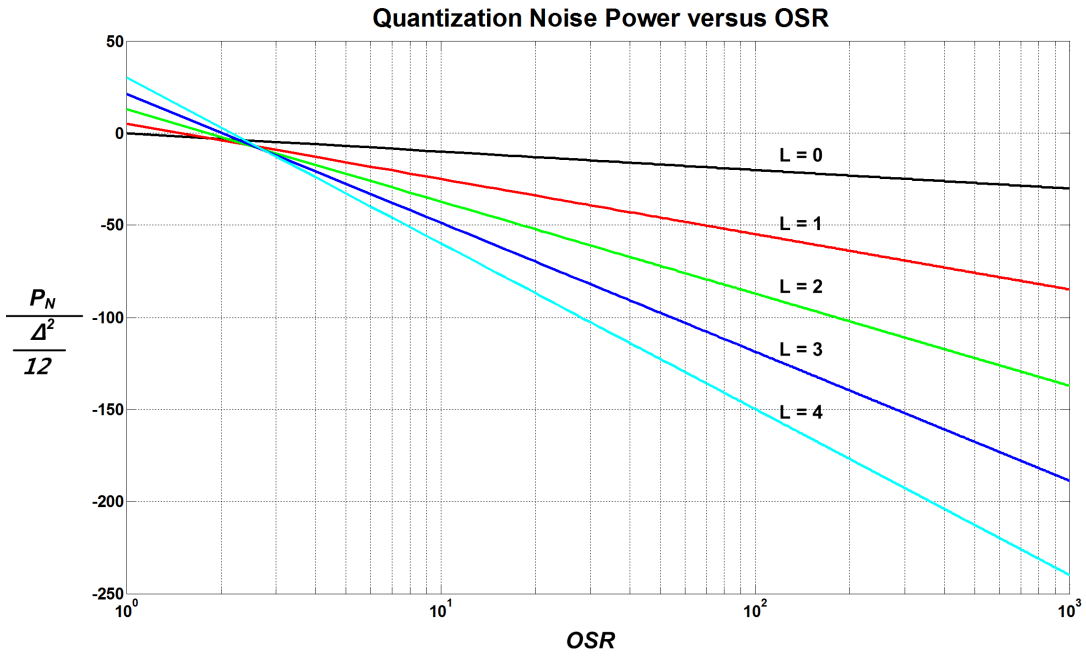

Figure 4.19: Quantization noise power of L-th order sigma delta modulator versus OSR

guished clearly in the frequency domain. For example, if the noise floor power spectral density is $2\text{nV}/\sqrt{\text{Hz}}$ within a 10KHz bandwidth and signal is 20nV_{rms}, SNR is

$$SNR_{dB} = 20\log\left(\frac{20nV}{\frac{2nV}{\sqrt{Hz}}\cdot\sqrt{10KHz}}\right)$$
$$= -20dB$$

The signal amplitude is 20dB below the noise floor, and is seen sharply and clearly in the spectrum even if the total SNR is -20dB. Like this example, spectroscopy applications do not emphasize on SNR but rather, the noise floor. As we know, the quantization noise floor of a L-th order sigma delta modulator is expressed in Eq. (4.63). If the sinusoidal signal has amplitude of $\frac{\Delta}{2}$ at f_0 (maximum signal amplitude), the difference between

and the noise floor is

$$
\begin{aligned}
Difference(f)_{at\ f=f_0} &= \frac{\frac{\Delta}{4}}{\sqrt{\frac{\Delta^2}{12f_s}\left[2\sin\left(\frac{\pi f}{f_s}\right)\right]^{2L}}}\ |_{at\ f=f_0} \\
&= \frac{1}{\sqrt{\frac{4}{3f_s}\left[2\sin\left(\frac{\pi f_0}{f_s}\right)\right]^{2L}}} \\
&\simeq \frac{1}{\sqrt{\frac{4}{3f_s}\left[2\left(\frac{\pi f_0}{f_s}\right)\right]^{2L}}} \\
&= \frac{1}{\sqrt{\frac{2}{3f_0}\frac{\pi^{2L}}{OSR^{2L+1}}}} \qquad (4.65) \\
Difference(f_0)_{dB} &= -10\log\left(\frac{2}{3f_0}\frac{\pi^{2L}}{OSR^{2L+1}}\right) \qquad (4.66)
\end{aligned}
$$

In Eq. (4.66), as the oversampling ratio (OSR) increases, the maximum difference between the signal and the noise floor increases. For the higher order sigma delta modulators, this difference is significantly increased.

We analyzed the benefits from oversampling and sigma delta modulation. Now, let's talk about signal range of the 1-bit second order sigma delta modulator in Fig. 4.17. Consider when we apply a sinusoidal signal with amplitude 3dB below full scale. Here the full scale value is Δ because just a 1-bit quantizer is used. The simulation in [1] reveals that the signal range required at the outputs of two integrators is several times the full scale-analog input range, $\pm\Delta/2$ as shown in Fig. 4.23. This requirement represents a severe problem in circuit technologies, such as CMOS VLSI, where the dynamic range is restricted. The second integrator's output is more easily saturating than the first output. Because the output voltage swing is determined by the supply voltage and the overdrive

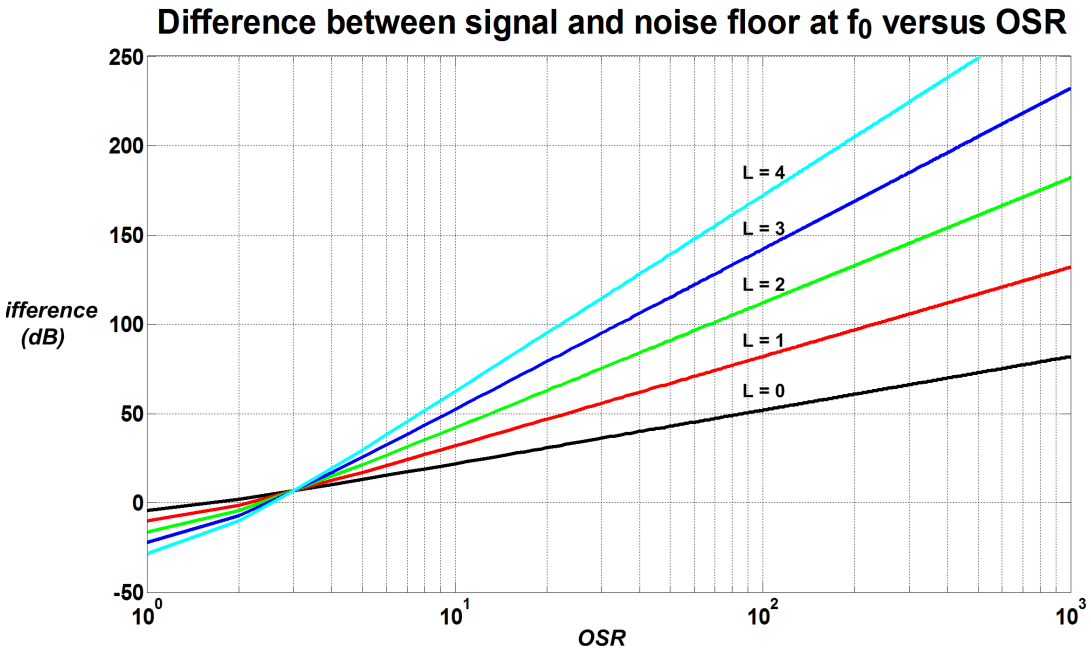

Figure 4.20: Difference between signal and noise floor at f_0 versus OSR

voltage of current source, the possible maximum input signal level without saturating the integrators are smaller than expected. When the integrator outputs become limited, the quantization error increases and the system starts showing nonlinear behavior. Therefore the maximum SNR obtainable is reduced because of limited voltage swing. To solve this problem, the modified sigma delta modulator architecture is shown in Fig. 4.21 and Fig. 4.22 . The signal transfer function and the quantization noise transfer function are

$$G_1 = G_2 = 0.5 \quad \text{in typical design}$$

$$H_S(z) = \frac{0.25z^{-2}}{1 - 1.5z^{-1} + 0.75z^{-2}} \tag{4.67}$$

$$H_Q(z) = \frac{(1 - z^{-1})^2}{1 - 1.5z^{-1} + 0.75z^{-2}} \tag{4.68}$$

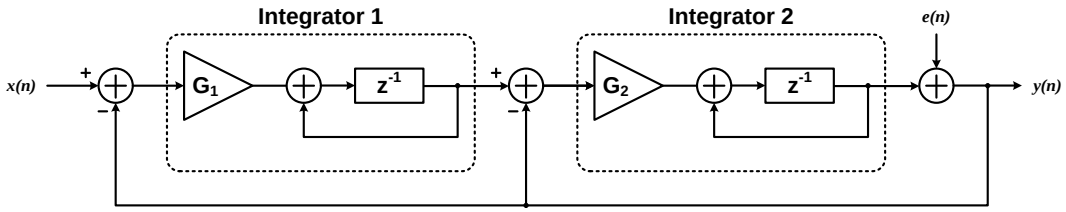

Figure 4.21: Block diagram of the second order sigma delta modulator

This architecture differs from the previous configuration in two aspects: a forward path delay is included in both integrators, thus simplifying the implementation of the modulator with straightforward sampled-data analog circuits, and each integrator is preceded by an attenuation of 0.5. The probability densities of the outputs of the two integrators for Fig. 4.17 and 4.21 are shown in Fig. 4.23. While the signals at the outputs of two integrators extend only slightly beyond the full-scale for the modified modulator design, the signal ranges are comparably larger for the traditional architecture. Therefore, we can increase the maximum input signal level. Before choosing this architecture, there are some values to be decided. First, the IF frequency is chosen for down conversion and avoiding 1/f noise. Based on previous experience for 130nm CMOS process, the IF frequency keeps constant around 10KHz, as LO frequency is adjusted by the frequency synthesizer. Second, the order of modulator and oversampling ratio are decided. We already looked at a modified second order type because it is simple and stable. The only remaining thing to be selected is the oversampling ratio (OSR). Now as we know, the maximum difference between the signal and noise floor is dependent on OSR. In general, an over-sampling ratio of 128 in a 1-bit 2^{nd} order sigma delta ADC provides

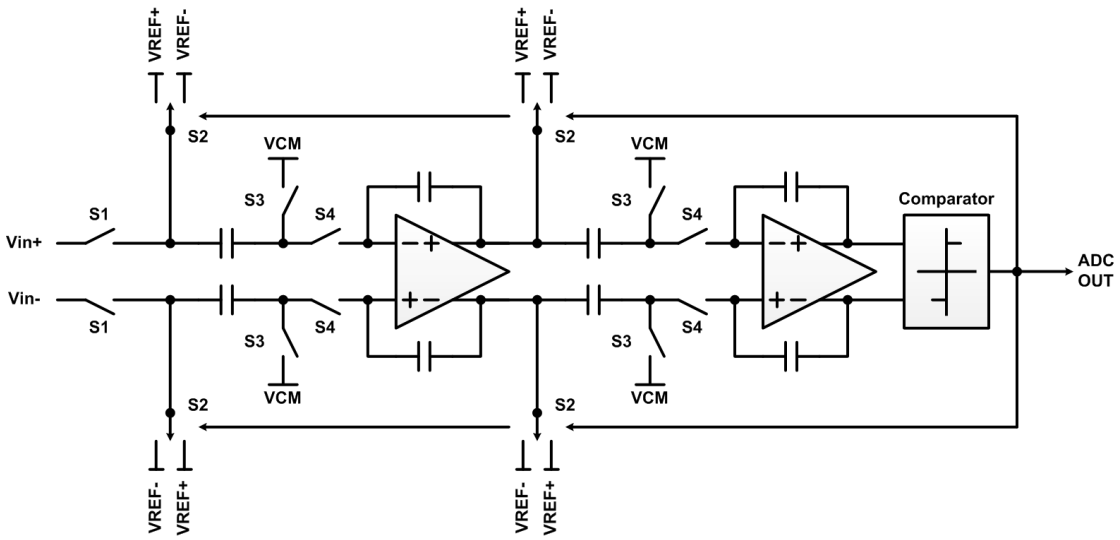

Figure 4.22: Simplified circuits of the designed 1-bit second order sigma delta modulator

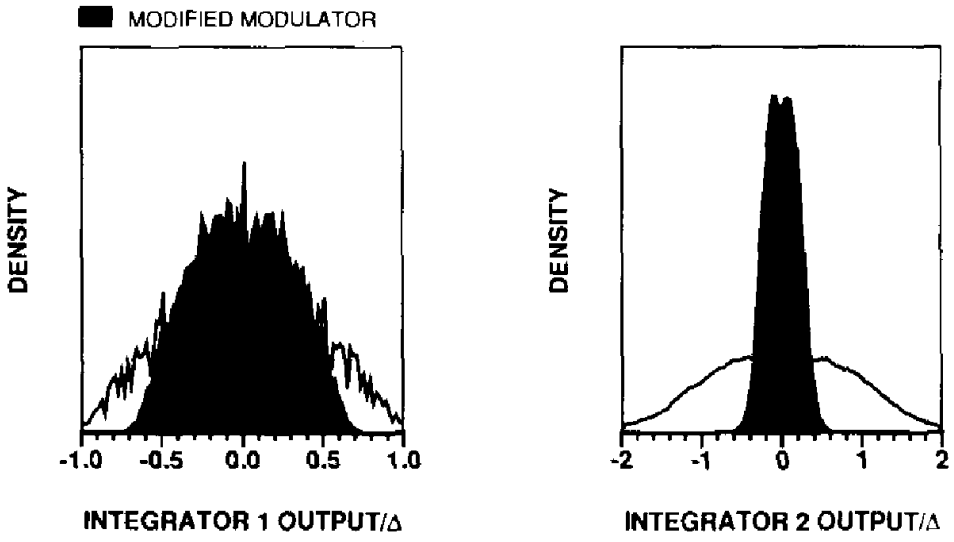

Figure 4.23: Comparison of integrator output probability densities for traditional and modified architectures with sinusoidal input 3dB below full scale [1]

a maximum SNR of 80dB. However, we don't care about this value. For example, the significant frequency contents of ^{1}H NMR spectrum at 5T is distributed within 2 KHz at 212 MHz and those of ^{31}P NMR spectrum at 5T is distributed within 4KHz at 86 MHz. Considering this narrow bandwidth, the real SNR will be a little bit larger than 80dB. In the NMR spectrum, the difference between the signal amplitude and the noise floor is much important than this SNR. In other words, if the meaningful frequency contents are 3dB or 6dB higher than noise floor and enough far away each other to be distinguished, even if the total SNR is lower than 0dB, the NMR spectrometer works fine. Let's review the noise of the ADC. As usual, the quantization noise power of an ADC is $\frac{\Delta^2}{12}$, where Δ is the LSB. Increasing the sampling frequency (f_s) reduces the quantization noise power density to $\frac{\Delta^2}{12 \cdot f_s}$ because the total quantization noise power is constant. This means that quantization noise floor is inversely proportional to the over-sampling frequency. In addition, sigma delta modulation is low-pass filtering signal and noise (different from the quantization noise) at the input of ADC and is ideally suppressing the quantization noise of ADC at low frequencies with the order of sigma delta modulation. In fact, as the operational transconductance amplifier (OTA) does not have infinite gain at low frequency, the quantization noise level at low frequency depends on the total gain of two OTAs in the ADC. The quantization noise floor ($V^2_{q\_floor}(f)/df$) is given by

$$\frac{V^2_{q\_floor}(f)}{df} = \frac{\Delta^2}{12} \cdot \frac{1}{f_s} \cdot \left(\frac{1}{A_1 \cdot A_2} \right)^2 \tag{4.69}$$

where Δ is the quantization level, f_s the over-sampling frequency, and A_1 and A_2 the open loop gains of two OTAs. In Fig. 4.24, this flat noise power level is constant from

dc to f_{c1}, where f_{c1} is the crossover frequency between 1/f noise and the quantization noise floor (4.69) and is given by

$$\begin{aligned} f_{c1} &= \frac{f_s}{2\pi} \ln\left(1 - \frac{1}{A_0 + 2}\right) \\ &\simeq \frac{f_s}{2\pi(A_0 + 2)} \\ A_0 &= A_1 = A_2 \end{aligned} \tag{4.70}$$

where A_0 represents of the dc gain of the OTA when A_1 and A_2 are equal. Equations (4.69) and (4.70) are very important in the case that the spectrum has meaningful frequency components with a large magnitude ratio relative to each other. For instance, in ^{1}H NMR spectrum from a liquid sample there is a 80 - 100 dB magnitude difference within the bandwidth. Typically, the water signal is extremely high and its neighbors are extremely small. In the worst case the water signal from non-homogeneity and phase noise of the frequency synthesizer can hide its neighbors. To avoid this problem, special pulse sequencing is developed to suppress the water signal. If f_{c1} is lower than the IF frequency (10 KHz) (equivalent to if OTA has enough gain), we can ignore equation (4.69). Now let's check the signal to noise level difference. The maximum signal power of this 1-bit 2^{nd} order sigma delta ADC is limited to $\frac{1}{2} \cdot (\frac{\Delta}{4})^2$ because the output of first integrator saturates easily and increases the noise power when the signal power larger than this value [1]. The difference between the maximum signal power and the

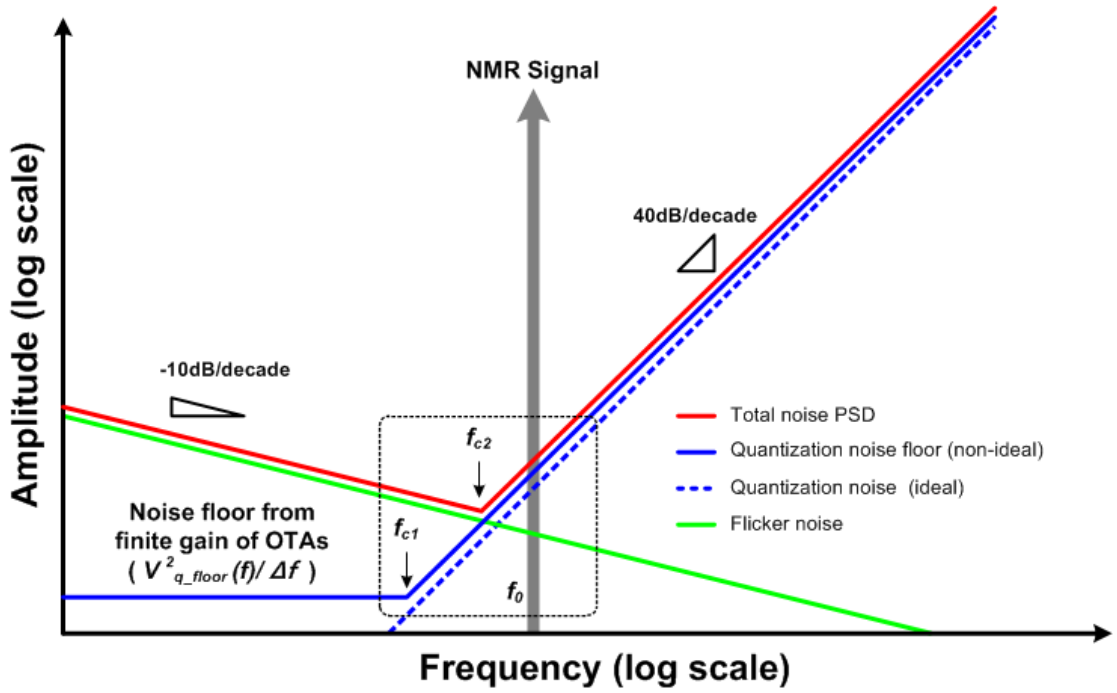

Figure 4.24: NMR FFT spectrum of 1-bit 2^{nd} sigma delta modulator

quantization noise is given by

$$Difference = \frac{\frac{1}{2} \cdot (\frac{\Delta}{4})^2}{\frac{\Delta^2}{12 \cdot f_s} \cdot \mid \frac{(1-z^{-1})^2}{1-1.5z^{-1}+0.75z^{-2}} \mid^2_{at\ f_0}} \tag{4.71}$$

$$G_1 = G_2 = 0.5$$

At 10 KHz (f_0) this difference is 112 dB which is larger than the 100dB required. This level is enough for ^{1}H NMR spectrum. Also we need to consider f_{c2}. MOS devices inherently have 1/f noise due to the impurity on the oxide surface. It depends on the dimension of MOS transistors. f_{c2} is the crossover frequency between 1/f noise and the quantization noise curve. As 1/f noise curve is mainly determined by the input transistors of the first OTA in the ADC, we need to decide carefully their size to make f_{c2} lower

than the IF frequency with sustaining gain and frequency requirements. Accordingly, f_{c1} and f_{c2} must be kept lower than the IF frequency by increasing dc gain of two OTAs and widening of input transistors of first OTA.

4.4 Frequency Synthesizer (PLL)

For wired and wireless communications such as GSM, CDMA, Wireless LAN and serial interfaces, the transmitter and receiver use the same frequency within the allocated band. This frequency is called a channel frequency and is properly controlled according to the data rate and channel capacity. Therefore, both transmitter and receiver generate this well-defined frequency within the band. All of these functions are executed in a frequency synthesizer called as a PLL (phase locked loop). In the same manner, a NMR transceiver needs a frequency synthesizer block to activate nuclei of interest in the sample and receive a NMR signal back from the sample. We can consider the Larmor frequency range (5MHz $\sim$ 300MHz) as a band and each Larmor frequency as a channel in NMR spectroscopy. As mentioned in chapter 3, phase noise is the most critical requirement in communication systems and is also important in our application.

In short, the well-defined LO signal drives the mixer to translate the NMR signal into an IF frequency. This signal is made from the frequency synthesizer and is changeable. The NMR receiver performance is highly dependent on the phase noise of the PLL to discriminate several frequency peaks like a spectrum analyzer. For sensing nuclei of interest within the frequency range 5MHz - 300MHz, a fractional type frequency

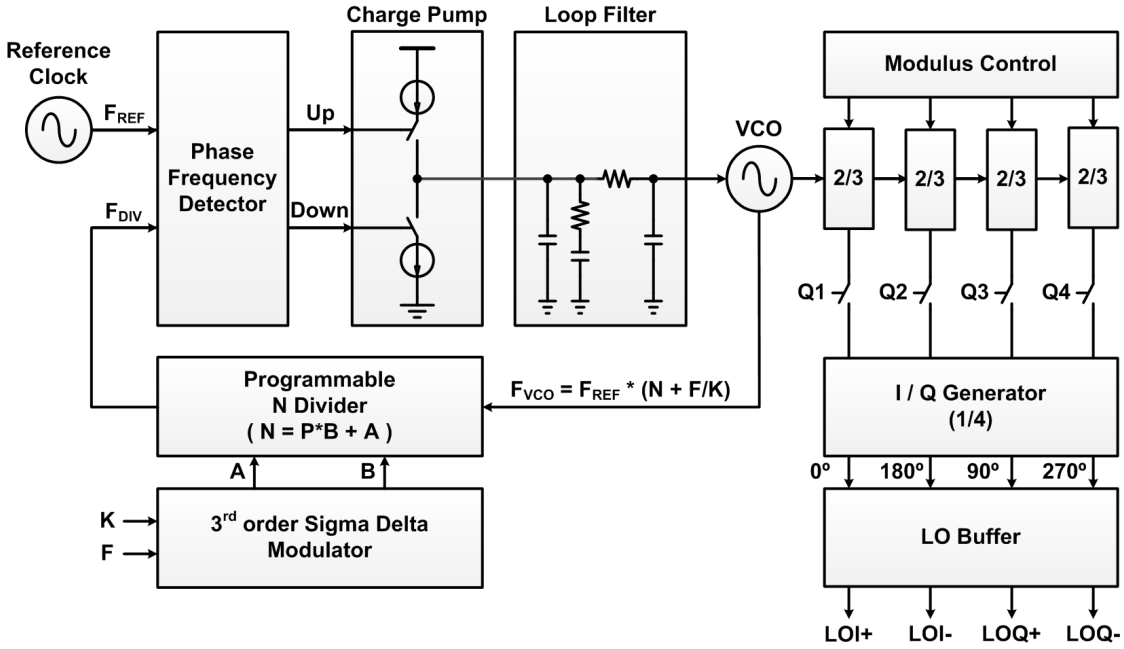

Figure 4.25: Proposed frequency synthesizer

synthesizer with a tiny frequency step should be implemented rather than an integer type. An LC based oscillator is preferred rather than a ring-type oscillator. It has an inherent lower phase noise and is desirable even though it consumes more power and occupies big area due to the inductor. Because huge area is needed to directly generate 5MHz $\sim$ 300MHz from a PLL, the PLL generates a high frequency and the following post multi modulus blocks divide this high frequency to the Larmor frequency. Our proposed frequency synthesizer block diagram is shown in Fig. 4.25.

In this section, the design procedure for a frequency synthesizer is explained in detail together with an analysis of PLL fundamentals. Look at the linear PLL block diagram is shown in Fig. 4.26. This model is based on a charge pump PLL because it is used

commonly in modern frequency synthesizer applications. It includes a reference clock source, a phase frequency detector (PFD), a charge pump (CP), a loop filter (LF), a voltage-controlled oscillator (VCO) and a N-divider. The phase frequency detector detects phase difference between the reference clock and the N divided signal from VCO. This difference is translated to a voltage with an aid of a charge pump circuit. During this period, a constant current charges or discharges an output capacitor of a loop filter. This voltage is typically fluctuating with the same frequency of the reference clock. So the following low pass filter reduces these fluctuations significantly and make an output voltage close to dc. Typically this loop filter has a low-pass filter characteristic with an order of $2 \sim 4$ and is very important for determining PLL loop stability. The following VCO block generates a frequency (not phase) according to input voltage. If the VCO obtains a constant input voltage, it generates a stable fundamental frequency. There are

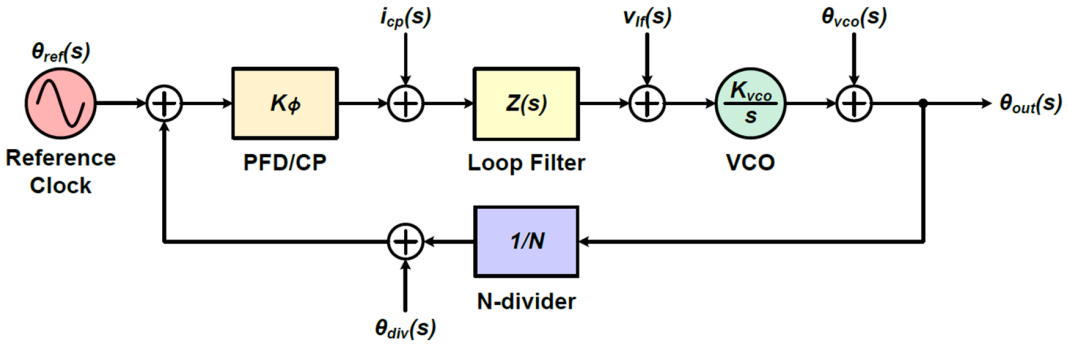

Figure 4.26: Linear model of PLL

some parameters shown in the linear model. All parameter definitions are below.

$\theta_{ref}(s)$: phase noise of the reference clock source

K_ϕ : gain of the phase frequency detector and charge pump

i_{cp} : current noise of the phase frequency detector and charge pump

$Z(s)$: loop filter transfer function

$v_{lf}(s)$: voltage noise of resistors in the loop filter

K_{vco} : gain of VCO

$\theta_{vco}(s)$: phase noise of VCO

N : frequency divider ratio

$\theta_{div}(s)$: phase noise from the N-divider

$\theta_{out}(s)$: phase noise from the PLL

Here are the important things to keep in mind when we design a loop filter. First, the combined gain (K_ϕ) of the PFD and CP is expressed as $\frac{I_{cp}}{2_\pi}$ ($\frac{A}{rad}$), where I_{cp} is a constant

Table 4.1: Phase noise transfer function of PLL

Noise source	Transfer function		
Reference clock	$\frac{\theta_{out}(s)}{\theta_{ref}(s)}$	$N \cdot \frac{T(s)}{1+T(s)}$	Low pass
PFD / CP	$\frac{\theta_{out}(s)}{i_{cp}(s)}$	$\frac{N}{K_\phi} \cdot \frac{T(s)}{1+T(s)}$	Low pass
Loop Filter	$\frac{\theta_{out}(s)}{v_{lf}(s)}$	$\frac{K_{vco}}{s} \cdot \frac{1}{1+T(s)}$	Band pass
VCO noise	$\frac{\theta_{out}(s)}{\theta_{vco}(s)}$	$\frac{1}{1+T(s)}$	High pass
N-divider noise	$\frac{\theta_{out}(s)}{\theta_{div}(s)}$	$-N \cdot \frac{T(s)}{1+T(s)}$	Low pass

current of the charge pump. Second, the gain of the VCO (K_{vco}) uses an unit of $\frac{rad}{V}$ not $\frac{Hz}{V}$ in this analysis. Now, we define the loop gain transfer function $T(s)$ of the PLL as

$$T(s) = \frac{K_\phi \cdot K_{vco} \cdot Z(s)}{N \cdot s} \tag{4.72}$$

Based on this transfer function $T(s)$, all transfer functions from each noise source to the output phase noise of PLL are listed in Table. 4.1. According to this table, the noise from the reference clock source and the N-divider block have the same transfer function characteristics (low pass) with opposite polarity. The phase noise of the VCO is suppressed at low frequencies and is passed into the output at high frequencies.

In fact, while a type-I PLL is inherently stable because it has only one pole at the origin, a charge pump PLL (type-II PLL) has two poles at the origin provided by a VCO and a current-voltage conversion from a combination of a charge pump and a capacitor in

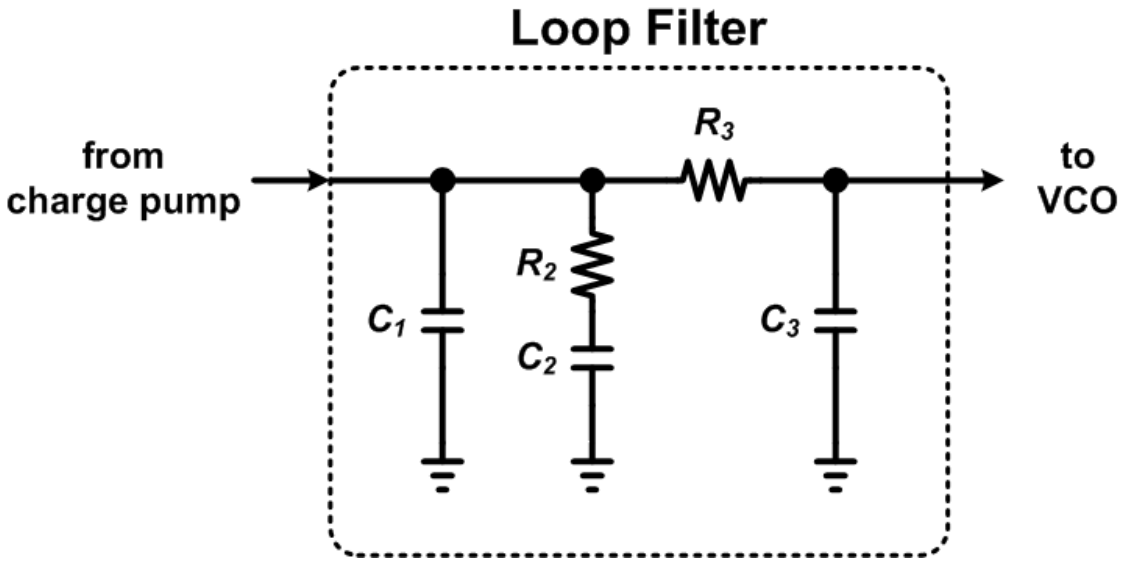

Figure 4.27: Third order loop filter

a loop filter. Therefore the total phase shift in a feedback loop is 360° or 2π and the PLL is definitely unstable without any compensation from a loop filter. In PLL design, most effort should be done toward ensuring a loop filter for the stable operation of the PLL. In our NMR frequency synthesizer, a third order loop filter shown in Fig. 4.27 is designed to reduce the harmonic spurs of the input reference clock frequency and suppress the phase noise at high frequency. Now we will find all values of the capacitors and resistors in a loop filter through mathematical analysis. The transfer function of the loop filter $Z(s)$ is defined simply as

$$Z(s) = \frac{1 + s \cdot T_2}{s \cdot A_0 \cdot (1 + s \cdot T_1) \cdot (1 + s \cdot T_3)} \tag{4.73}$$

$$= \frac{1 + s \cdot T_2}{s \cdot (A_2 \cdot s^2 + A_1 \cdot s + A_0)} \tag{4.74}$$

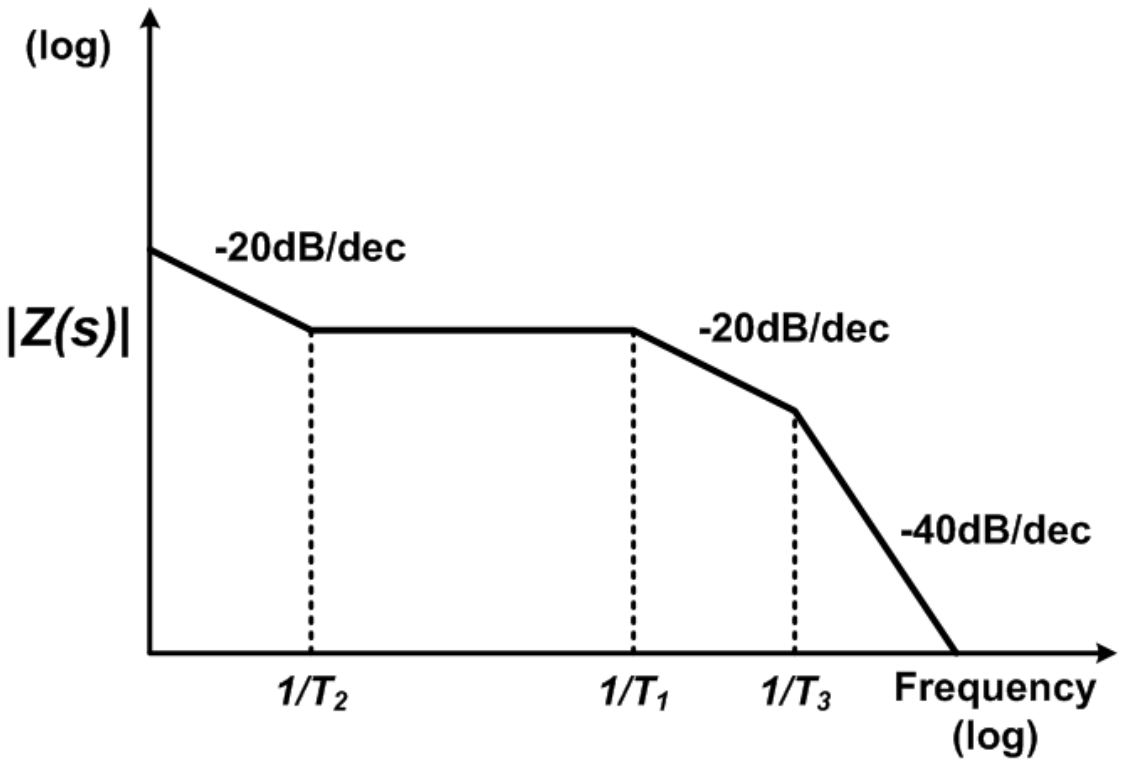

Figure 4.28: Frequency response of third order loop filter

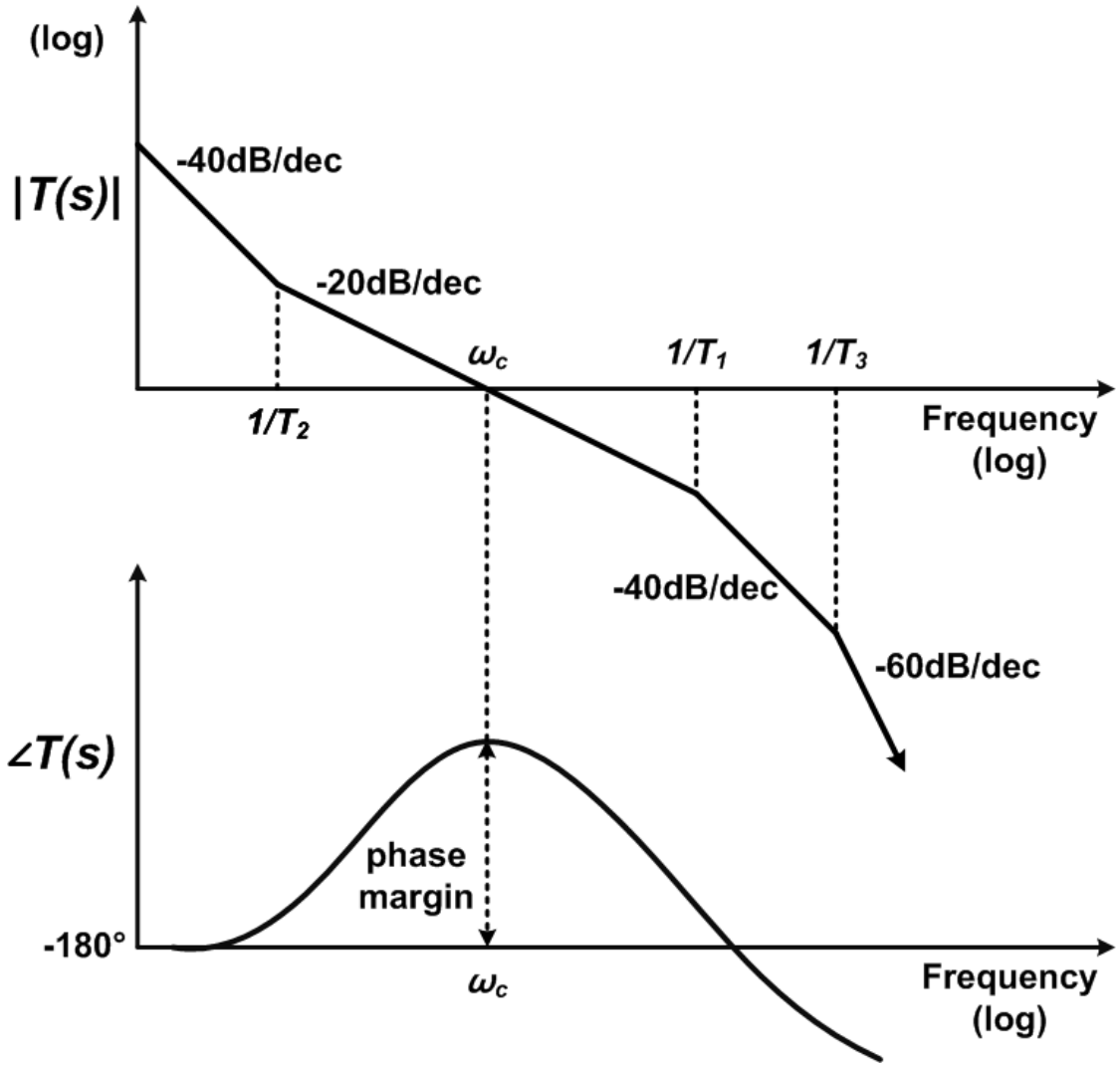

Figure 4.29: Frequency response of loop gain transfer function

, where T_1, T_2, T_3, A_0, A_1 and A_2 are expressed with resistors and capacitors below.

$$A_2 = A_0 \cdot T_1 \cdot T_3 \qquad = C_1 \cdot C_2 \cdot R_2 \cdot C_3 \cdot R_3 \tag{4.75}$$

$$A_1 = A_0 \cdot (T_1 + T_3) \quad = C_2 \cdot C_3 \cdot R_2 + C_1 \cdot C_2 \cdot R_2 + C_1 \cdot C_3 \cdot R_3 + C_2 \cdot C_3 \cdot R_3 \tag{4.76}$$

$$A_0 \qquad = C_1 + C_2 + C_3 \tag{4.77}$$

Again, the loop gain transfer function is expressed as

$$T(s) = \frac{K_\phi \cdot K_{vco}}{N \cdot s} \cdot \frac{1 + s \cdot T_2}{s \cdot A_0 \cdot (1 + s \cdot T_1) \cdot (1 + s \cdot T_3)} \tag{4.78}$$

$$= \frac{K_\phi \cdot K_{vco}}{N \cdot s} \cdot \frac{1 + s \cdot T_2}{s \cdot (A_2 \cdot s^2 + A_1 \cdot s + A_0)} \tag{4.79}$$

The loop filter has one zero at $1/T_2$ and three poles at the origin, $1/T_1$ and $1/T_3$ as shown in Fig. 4.28. With this loop filter function, the frequency response of the loop transfer function $T(s)$ is obtained as shown in Fig. 4.29 when the PLL is stable. Here ω_c is the loop bandwidth of the PLL, which is usually less than one tenth of the reference frequency. Due to the frequency to phase conversion in the VCO, the loop transfer function is -40dB/dec at the origin. The position of zero ($1/T_2$) and pole ($1/T_1$) makes the PLL stable conditionally at ω_c. Because the loop bandwidth determines the setting time of loop, if the loop bandwidth is fixed to satisfy the requirement, how do we calculate the phase margin (ϕ_M)? The phase margin at ω_c from Eqn. 4.78 is defined as

$$\phi_M = \tan^{-1}(\omega_c \cdot T_2) - \tan^{-1}(\omega_c \cdot T_1) - \tan^{-1}(\omega_c \cdot T_3) + 180^\circ \tag{4.80}$$

T_2 is obtained below by setting the derivative of the phase margin at ω_c equal to zero

$$\left(\frac{d\phi}{d\omega}\right)_{at\ \omega=\omega_c} = 0 \tag{4.81}$$

$$T_2 \simeq \frac{\gamma}{\omega_c^2 \cdot (T_1 + T_3)} \tag{4.82}$$

In the above equation, γ is defined as the Gamma Optimization factor. Typically, γ is around 1. T_3 is expressed as with the ratio of T_1

$$T_3 = T_1 \cdot T_{31} \tag{4.83}$$

Finally, T_2 and the phase margin (ϕ) are expressed with T_1 as

$$T_2 \simeq \frac{\gamma}{\omega_c \cdot T_1 \cdot (1 + T_{31})} \tag{4.84}$$

$$\phi_M = \tan^{-1}\left(\frac{\gamma}{\omega_c \cdot T_1 \cdot (1 + T_{31})}\right) - \tan^{-1}(\omega_c \cdot T_1) - \tan^{-1}(\omega_c \cdot T_1 \cdot T_{31}) + 180^\circ \tag{4.85}$$

If the loop band width and the phase margin of the PLL is given, T_1 can be solved numerically or approximately as shown below

$$\tan(x) \simeq x \simeq \tan^{-1}(x) \tag{4.86}$$

$$T_1 \simeq \frac{\sec(\phi) - \tan(\phi)}{\omega_c \cdot (1 + T_{31})} \tag{4.87}$$

Therefore, once T_1 is known, T_2 and T_3 can be easily found. Interestingly, these value are calculated without using (K_ϕ, K_{vco} and N). If these parameters are chosen properly, first we calculate A_0 in 4.77, which is the sum of all capacitances in the loop filter. At

loop bandwidth frequency (ω_c), the loop gain $T(s)$ is equal to one.

$$\mid T(s) \mid_{s=j\omega_c} = \frac{K_\phi \cdot K_{vco}}{N \cdot \omega_c^2 \cdot A_0} \cdot \sqrt{\frac{(1+\omega_c^2 \cdot T_2^2)}{(1+\omega_c^2 \cdot T_1^2) \cdot (1+\omega_c^2 \cdot T_3^2)}} \quad = 1 \tag{4.88}$$

$$A_0 = \frac{K_\phi \cdot K_{vco}}{N \cdot \omega_c^2} \cdot \sqrt{\frac{(1+\omega_c^2 \cdot T_2^2)}{(1+\omega_c^2 \cdot T_1^2) \cdot (1+\omega_c^2 \cdot T_3^2)}} \quad = C_1 + C_2 + C_3 \tag{4.89}$$

If A_0 is obtained, A_1 and A_2 are automatically calculated like

$$A_1 = A_0 \cdot (T_1 + T_3) \tag{4.90}$$

$$A_2 = A_0 \cdot T_1 \cdot T_3 \tag{4.91}$$

Now the first step to get values for the components is to choose C_1. There are many possible choices, but the optimal choice is the one that maximizes C_3. This is desirable because it minimizes the impact of the VCO capacitance and resistor thermal noise due to R_3. Although the choice of C_1 that minimizes R_3 is slightly different than the choice of C_1 that maximizes C_3, these two values are so close, and making C_3 larger attenuates the noise due to R_3 more.

$$C_1 = \frac{A_2}{T_2^2} \cdot \left(1 + \sqrt{1 + \frac{T_2}{A_2} \cdot (T_2 \cdot A_0 - A_1)}\right) \tag{4.92}$$

Combining these equations yield

$$A_1 = T_2 \cdot C_1 - \frac{A_0 \cdot A_2}{T_2 \cdot C_1} - \frac{A_2 \cdot C_3}{T_2 \cdot C_1} \tag{4.93}$$

The above equation can be solved in order to express C_3 in terms of C_1

$$C_3 = \frac{-T_2^2 \cdot C_1^2 + T_2 \cdot A_1 \cdot C_1 - A_0 \cdot A_2}{T_2^2 \cdot C_1 - A_2} \tag{4.94}$$

C_2 and the other components can now be easily found.

$$C_2 = A_0 - C_1 - C_3 \tag{4.95}$$

$$R_2 = \frac{T_2}{C_2} \tag{4.96}$$

$$R_3 = \frac{A_2}{C_1 \cdot C_3 \cdot T_2} \tag{4.97}$$

Now, all resistors and capacitors have been calculated to meet the phase margin requirement of PLL. However, we need to replace these values with the feasible values and then check the loop bandwidth and the stability again.

Next, let's talk about phase noise contribution of each component. First, the noise from the reference clock is low-pass filtered as described in Table. 4.1. In the frequency range below the loop bandwidth, the phase noise of the reference clock will be increasing by $20 \cdot \log(N)$. But, it will decrease at frequencies above bandwidth. Fig. 4.30 shows typical frequency response of an input reference clock in a PLL. As a reference clock source, the voltage controlled temperature compensated crystal oscillator (VCTCXO) is commonly used. However, in military applications requiring extremely high resolution, an ovenized crystal oscillator (OCXO) is used.

Second, the combination of a phase frequency detector and a charge pump add phase noise to the PLL. When the PLL is locked, two up and down switches are on during a certain time duration to eliminate the dead-zone that can make a PLL an open loop. Define the current noise of the charge pump as i_{cp}. As listed in Table. 4.1, we have

$$\frac{\theta_{out}}{i_{cp}}(s) = \frac{\frac{K_{vco}}{s} \cdot Z(s)}{1 + \frac{K_\phi}{N} \cdot \frac{K_{vco}}{s} \cdot Z(s)} = \frac{N \cdot K_{vco} \cdot Z(s)}{N \cdot s + K_\phi \cdot K_{vco} \cdot Z(s)} \tag{4.98}$$

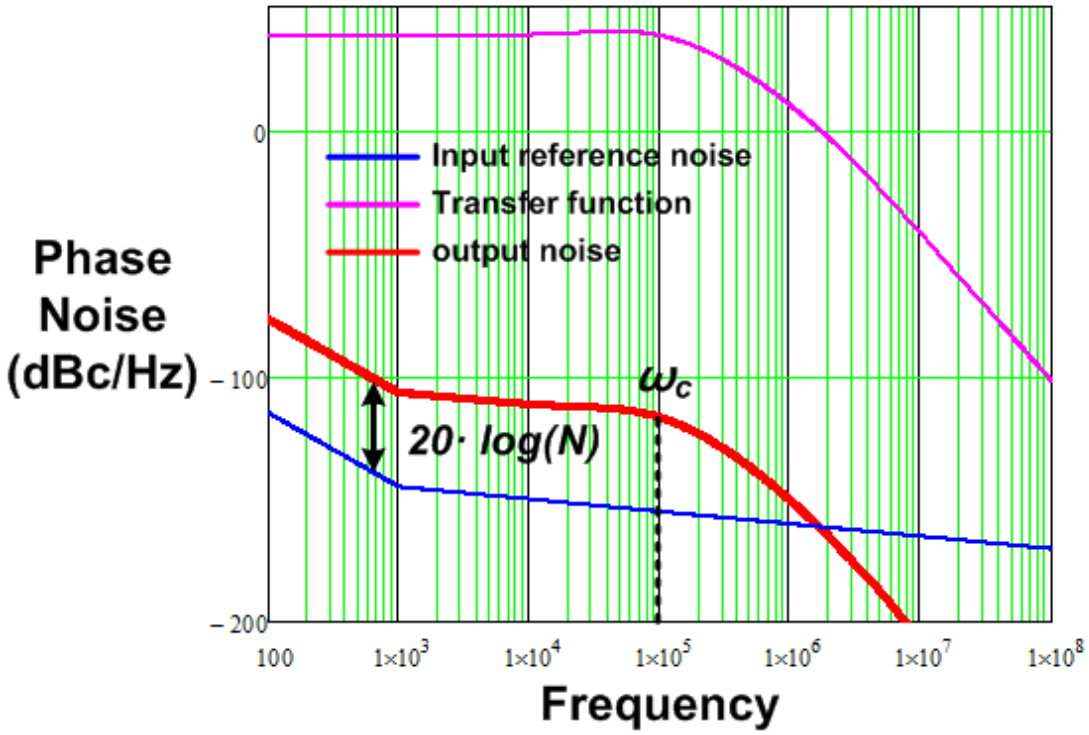

Figure 4.30: Phase noise contribution of the reference clock

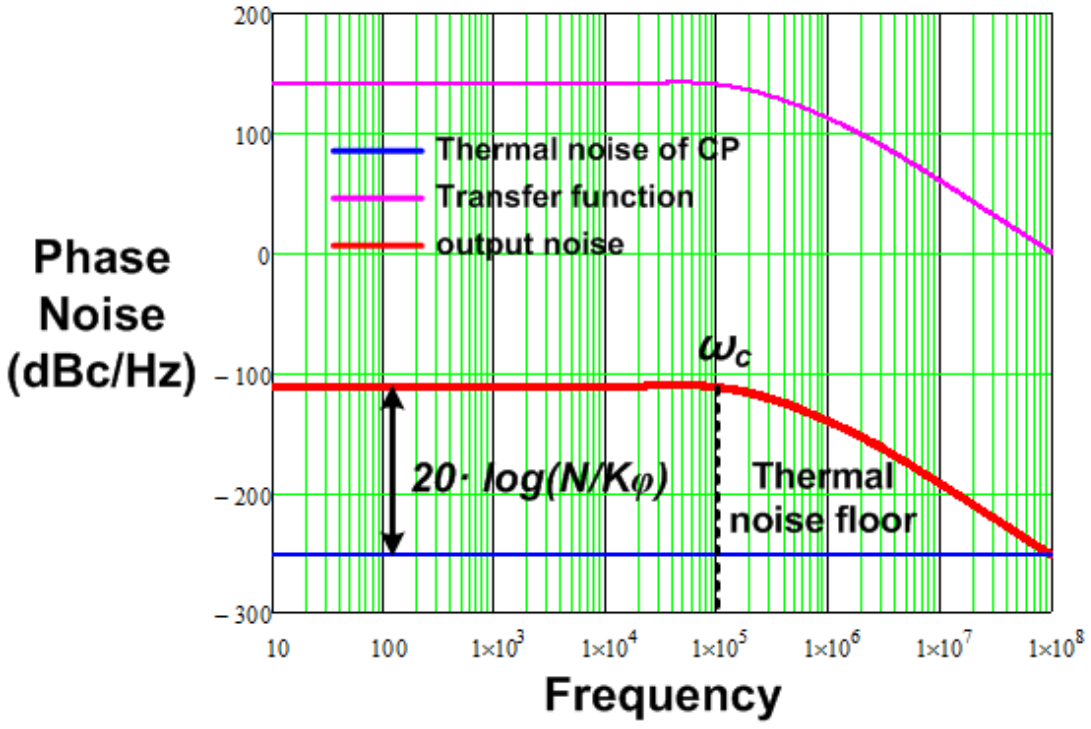

Figure 4.31: Phase noise contribution of the charge pump

Here we only consider the channel thermal noise of constant current source in the charge pump not the flicker noise. The charge pump current noise can be expressed as

$$i_{cp}^2 = 2 \cdot 4kTg_m \cdot \frac{t_{on}}{T_{ref}} = 2 \cdot 4kT \cdot \frac{2I_{CP}}{\Delta V} \cdot \frac{t_{on}}{T_{ref}} \tag{4.99}$$

where t_{on} is the turn-on time of the charge pump, $T_{ref} = \frac{1}{f_{ref}}$ is the period of the reference clock, and ΔV is the gate-to-source overdrive voltage corresponding to $(V_{GS} - V_T)$ of the current source / sink transistor in the charge pump. The frequency response of the input reference noise is plotted in Fig. 4.31.

Third, consider the noise from resistors in the loop filter shown in Fig. 4.27. The voltage transfer functions from the thermal noise of resistors are as follows.

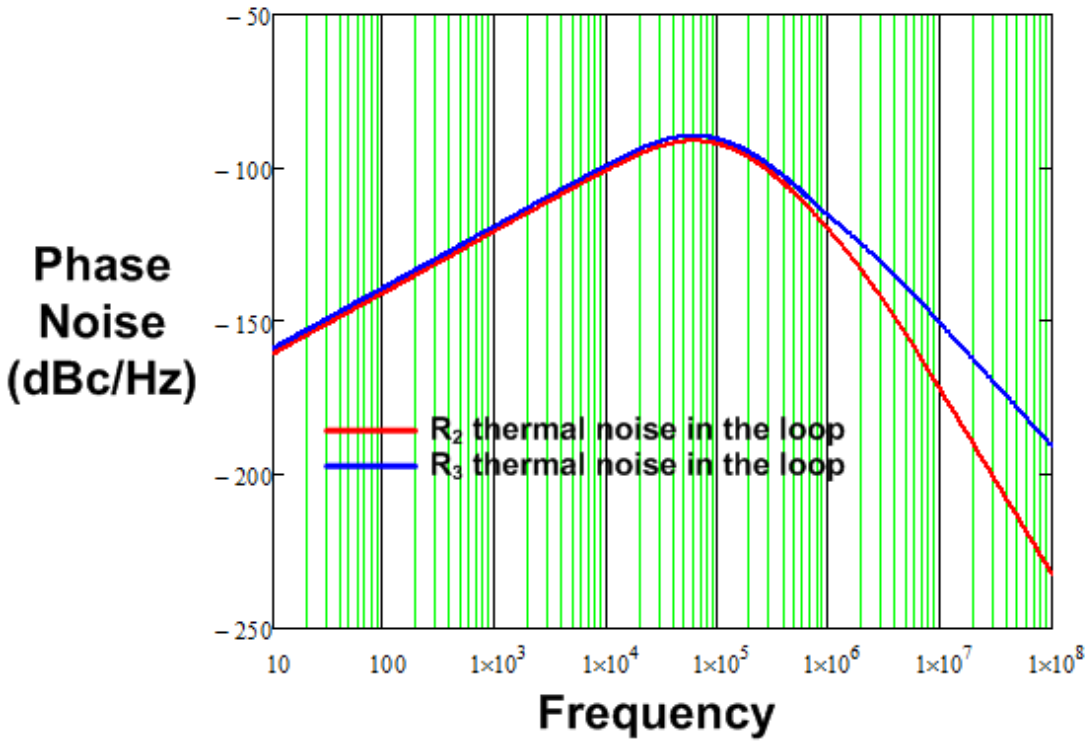

Figure 4.32: Phase noise contribution of resistors in the loop filter

$$\frac{v_{lf}}{v_{nR_1}}(s) = \frac{C_1}{C_1 + C_2 + C_3} \cdot \frac{1}{(1 + s \cdot T_1) \cdot (1 + s \cdot T_3)} \tag{4.100}$$

$$\frac{v_{lf}}{v_{nR_3}}(s) = \frac{C_1}{C_1 + C_2 + C_3} \cdot \frac{1 + s \cdot \left(\frac{R_1 C_1 C_2}{C_1 + C_2}\right)}{(1 + s \cdot T_1) \cdot (1 + s \cdot T_3)} \tag{4.101}$$

As listed in Table. 4.1, the loop filter control voltage noise to the PLL output phase noise transfer function is

$$\frac{\theta_{out}}{v_{lf}}(s) = \frac{\frac{K_{vco}}{s}}{1 + \frac{K_\phi}{N} \cdot \frac{K_{vco}}{s} \cdot Z(s)} = \frac{N \cdot K_{vco}}{N \cdot s + K_\phi \cdot K_{vco} \cdot Z(s)} \tag{4.102}$$

The frequency response of the input reference noise is plotted in Fig. 4.31.

Fourth, the VCO phase noise is calculated from the Leeson's model conceptually [26]. Based on this model, the VCO's single-side phase noise is defined by

$$L(\Delta f) = \frac{2FkT}{P_s} \left[1 + \left(\frac{f_0}{2Q_L \Delta f}\right)^2\right] \left(1 + \frac{\Delta f_{1/f^3}}{\mid \Delta f \mid}\right) \tag{4.103}$$

where F is the noise factor, P_s is the signal power, f_0 is the resonance frequency, Q_L is the quality factor of the tank circuit, Δf is the offset frequency from the resonance frequency, and $\Delta f_{1/f^3}$ is the corner frequency of $1/f^3$ phase noise. This linear time-invariant (LTI) model can be derived by the noise shaping due to the band-pass LC filtering effect. A simple model for the LC oscillator is shown in Fig. 4.33. The impedance for a parallel RLC tank circuit, for $\Delta f \ll f_0$, is

$$Z(f_0 + \Delta f) = R_P \cdot \frac{1}{1 + j2Q_L(\Delta f / f_0)} \tag{4.104}$$

where R_P is the parallel real impedance of the tank circuit at resonance, Q_L is the quality factor of the inductor (as the inductor has lower quality factor than the capacitor). So

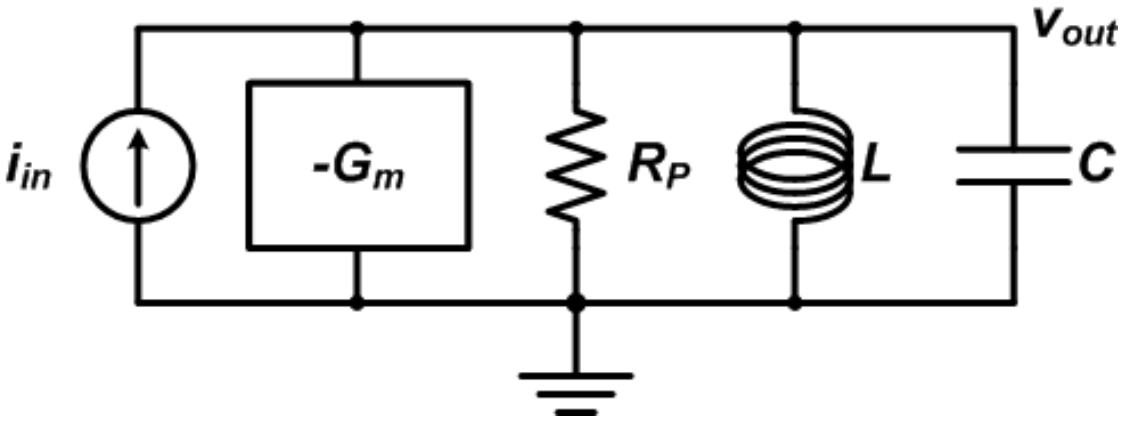

Figure 4.33: Simple LC oscillator noise model

the parallel real impedance (R_P) at resonance is mainly determined by the inductor. To sustain the oscillation, the negative impedance circuit is provided from the active transconductance circuit (called negative G_m) because the oscillation will decay and diminish due to the damping when the negative G_m is not included. The condition for oscillation is given by

$$R_P \geq \mid \frac{1}{G_m} \mid \tag{4.105}$$

For a parallel current source (i_{in}), the transfer function of the oscillator is expressed by the imaginary part of the impedance in (4.107).

$$H(\Delta f) = \frac{v_{out}\left(\frac{\Delta f}{f_0}\right)}{i_{in}\left(\frac{\Delta f}{f_0}\right)} = -jR_L \cdot \frac{f_0}{1 + j2Q_L\Delta f} \tag{4.106}$$

Here we can replace the current source with the current noise of the equivalent parallel resistor is

$$\frac{\bar{i_n^2}}{\Delta f} = 4FkT\frac{1}{R_P} \tag{4.107}$$

, where F is the excess noise factor. Therefore, the phase noise in the $1/f^2$ region is

$$L(\Delta f) = 10\log\left(\frac{\bar{v_n^2}}{\bar{v_s^2}}\right) \tag{4.108}$$

$$= 10\log\left(\frac{\frac{1}{2}\cdot \mid H(\Delta f)\mid^2 \frac{\bar{i_n^2}}{\Delta f}}{\frac{1}{2}V_{max}^2}\right) \tag{4.109}$$

$$= 10\log\left[\frac{2FkT}{P_s}\left(\frac{f_0}{2Q_L\Delta f}\right)^2\right] \tag{4.110}$$

Note that, the $1/f^3$ portion of the phase noise is completely empirical. In reality, both $1/f^3$ and $1/f^2$ phase noise are generated by noise up-conversion due to phase modulation and other nonlinear effects in the VCO instead of noise shaping of LC filtering. [27–29] developed more accurate phase noise model for oscillator. But in this paper, we will skip it. This analysis show how to approach the way of reducing the phase noise of a VCO. Typically PMOS NMOS cross coupled type VCOs are used due to low phase noise and the symmetry. However, we compared several types of VCOs based on a IBM 130nm CMOS process. The inductor used in simulation has an inductance (L) of 3.7nH and the quality factor (Q_L) of 19. According to the comparison in Table. 4.34, a VCO with an NMOS transconductance circuit and a PMOS current source shows the lowest phase noise at 100KHz offset for almost same resonance frequency ($\sim$ 2.5GHz). This type of VCO is chosen for our PLL. The schematic of the VCO is shown in Fig. 4.35. As listed in Table. 4.1, the VCO phase noise to the PLL output phase noise transfer function is

$$\frac{\theta_{out}}{\theta_{vco}}(s) = \frac{1}{1+\frac{K_\phi}{N}\cdot\frac{K_{vco}}{s}\cdot Z(s)} = \frac{N\cdot s}{N\cdot s + K_\phi\cdot K_{vco}\cdot Z(s)} \tag{4.111}$$

The frequency response of the input reference noise is plotted in Fig. 4.31.

	Phase Noise (dBc/Hz) at 100 KHz	Phase Noise (dBc/Hz) at 1 MHz	Vpp (V)	Fvco (GHz)
P-N Coupled	-91.95	-113.8	2.28	2.45942
P-Only (PMOS CS)	-96.41	-118.1	1.99	2.457G
P-Only (NMOS CS)	-89.77	-115.9	2.06	2.46G
N-Only (PMOS CS)	-100.3	-120.8	1.8	2.46G
N-Only (NMOS CS)	-93.15	-118.9	2.33	2.46GHz

Figure 4.34: Comparison of several types of VCO

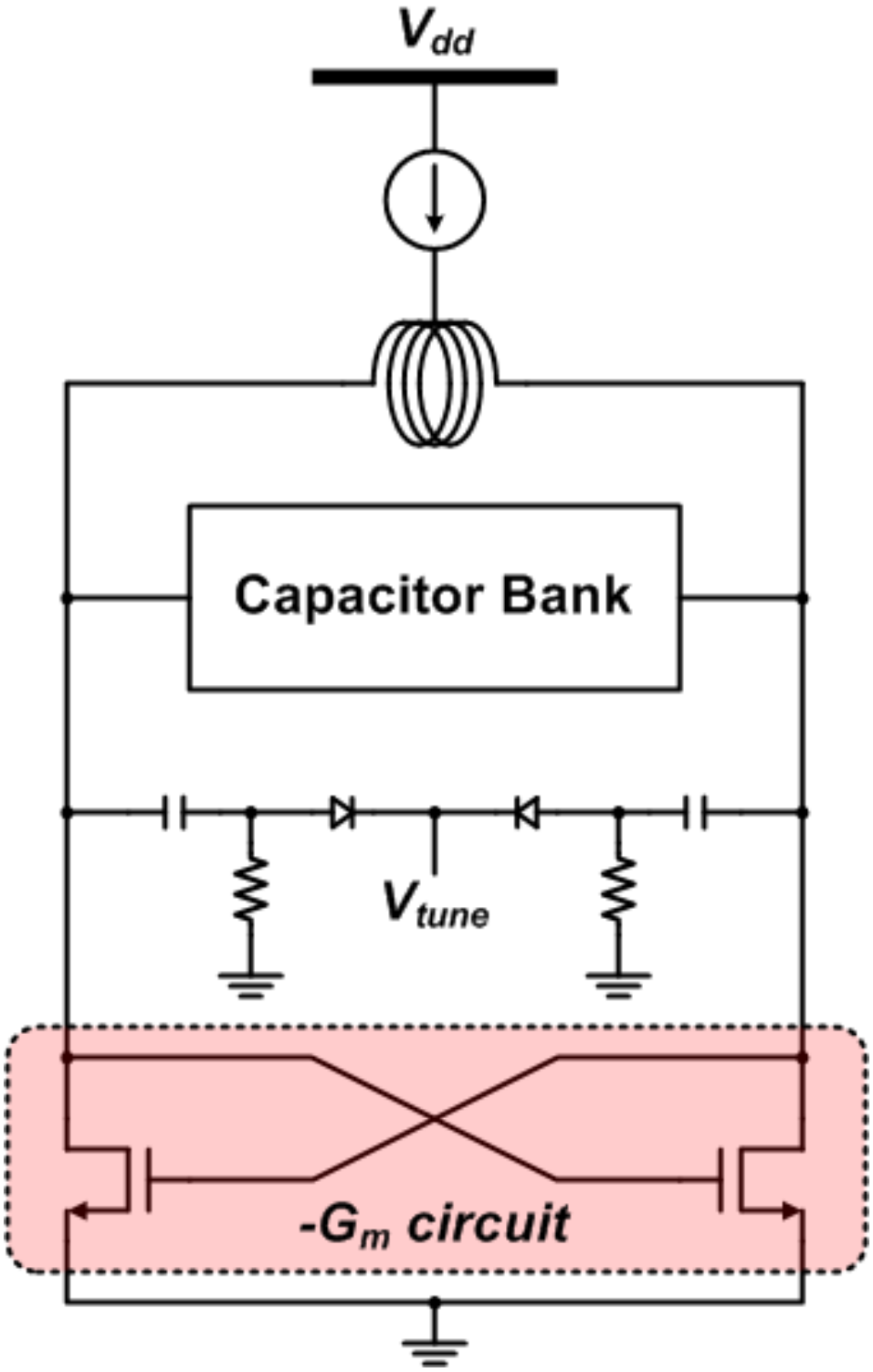

Figure 4.35: VCO with an NMOS transconductance circuit and a PMOS current source

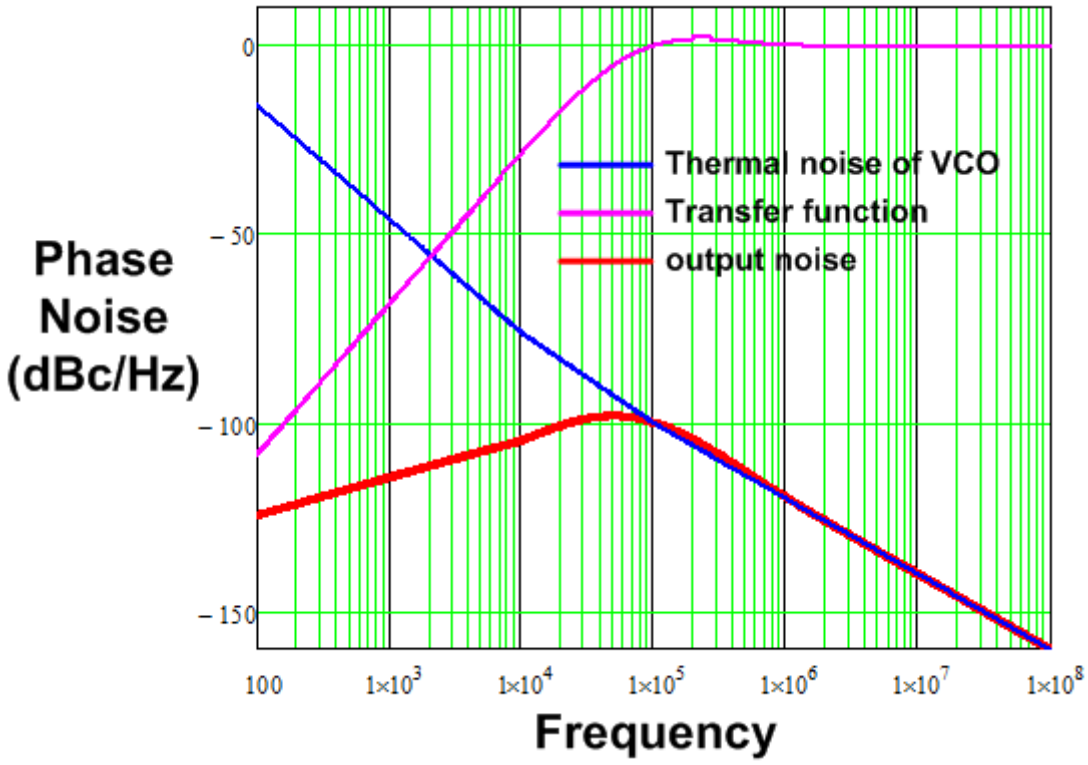

Figure 4.36: Phase noise contribution of VCO

Finally, the noise from the divider circuit is analyzed based on sigma delta modulation (SDM). To generate a fractional divider ratio, the divider changes the divider ratio (N) periodically to N±1, N±2, or N±3 according to the order of the sigma delta modulator. MASH type sigma delta modulation is used commonly but single-line (SL) delta modulation is used in this paper. According to [30], typically MASH type generates wide-spread high-frequency bit patterns, and requires more stringent requirements on the phase frequency detector design. However, SL is optimized for noise shaping function for low-spur frequency synthesis using a 3-b third-order modulator that generates less high-frequency noise and makes the system less sensitive to the substrate noise couping in Fig. 4.37. To calculate the noise, open-loop approximation is used to map the sigma delta quantization noise into PLL output noise [31]. This approach makes an open circuit between the VCO and the frequency divider and assumes that the input to the frequency divider is an ideal signal with the desired frequency $N \cdot f_{ref}$. The phase noise generated by the frequency divider is

$$S_{\theta_{out}}(f) = \left[\frac{f_{ref} \cdot Q_N(f)}{f \cdot N}\right] \qquad rad^2/Hz \tag{4.112}$$

where $Q_N(f)$ is the rms spectral density of the quantization noise of the sigma delta modulator. $Q(f)$ is expressed as

$$Q_N(f) = \sqrt{\frac{\Delta^2}{12 f_{ref}}} \mid H_{NTF}(z) \mid_{z=e^{j2\pi\left(\frac{f}{f_{ref}}\right)}} \tag{4.113}$$

where Δ is the quantization level that is 1 because the fractional number is limited within 0 to 1, and H_{NTF} is the SL transfer function of the quantization noise, which is given

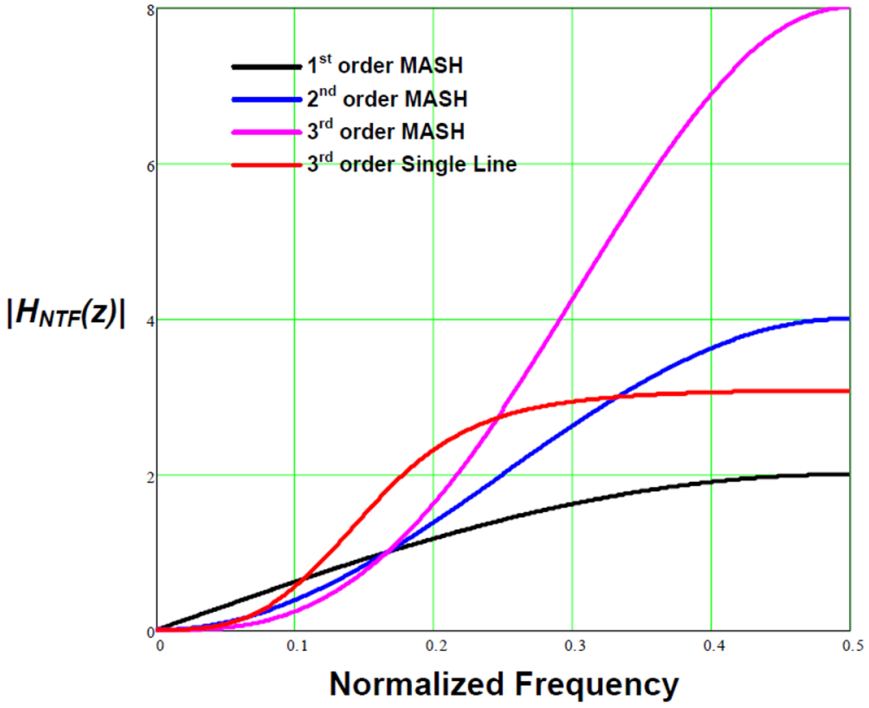

Figure 4.37: Comparison of transfer functions for MASH and SL

by

$$H_{NTF}(z) = \frac{(1-z^{-1})^3}{1-z^{-1}+0.5z^{-2}-0.1z^{-3}} \tag{4.114}$$

Then the power spectral density of phase noise in the SL sigma delta modulator becomes

$$S_{\theta_{div}}(f) = \frac{f_{ref}}{12(Nf)^2} \mid \frac{(1-z^{-1})^3}{1-z^{-1}+0.5z^{-2}-0.1z^{-3}} \mid^2_{z=e^{j2\pi\left(\frac{f}{f_{ref}}\right)}} \qquad rad^2/Hz \tag{4.115}$$

Since the phase noise transfer function from the divider to the PLL output is the same as the one from the reference clock to the output, we can view $S_{\theta_{div}}(f)$ as an equivalent input phase noise and use a closed-loop input-to-output phase transfer function to estimate output phase noise from the sigma delta modulator. As listed in Table. 4.1, the sigma

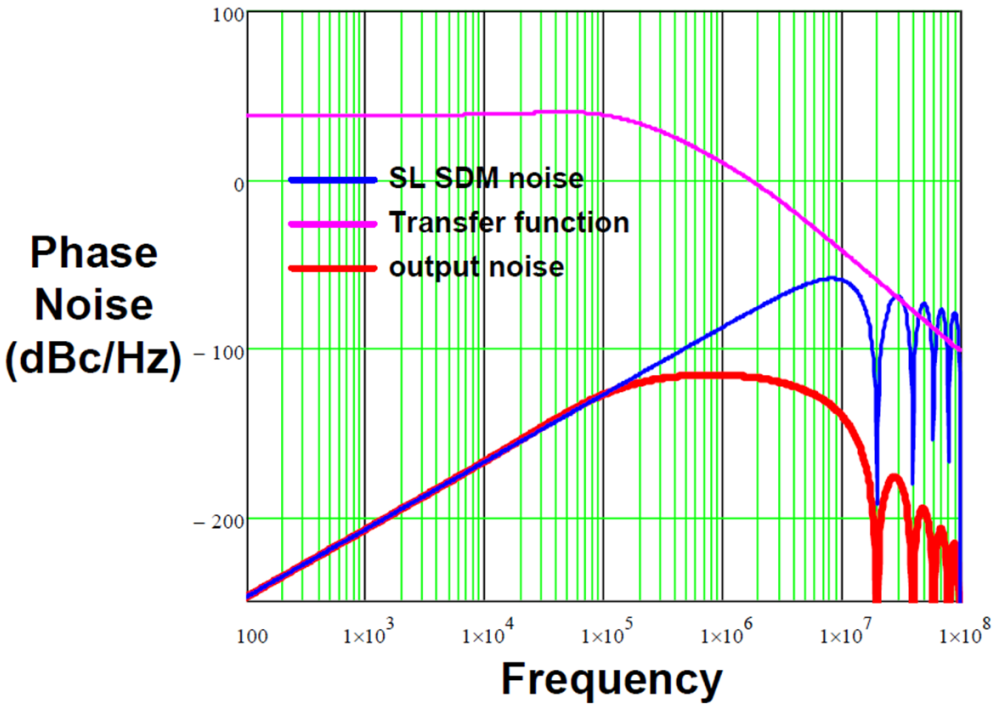

Figure 4.38: Phase noise contribution of SL SDM

delta modulator phase noise to the PLL output phase noise transfer function and the total phase noise due to the divider at PLL output are

$$\frac{\theta_{out}}{\theta_{div}}(s) = \frac{K_\phi \cdot \frac{K_{vco}}{s} \cdot Z(s)}{1 + \frac{K_\phi}{N} \cdot \frac{K_{vco}}{s} \cdot Z(s)} = \frac{N \cdot K_\phi \cdot K_{vco} \cdot Z(s)}{N \cdot s + K_\phi \cdot K_{vco} \cdot Z(s)} \tag{4.116}$$

$$S_{\theta_{out}}(f) = S_{\theta_{div}}(f) \cdot \mid \frac{\theta_{out}}{\theta_{div}}(s) \mid_{s=e^{j2\pi f}} \qquad rad^2/Hz \tag{4.117}$$

The frequency response of the phase noise from the divider is plotted in Fig. 4.38. The total phase noise contribution from each block is shown in Fig. 4.39. In Table. 4.2, all parameters used in PLL design are listed.

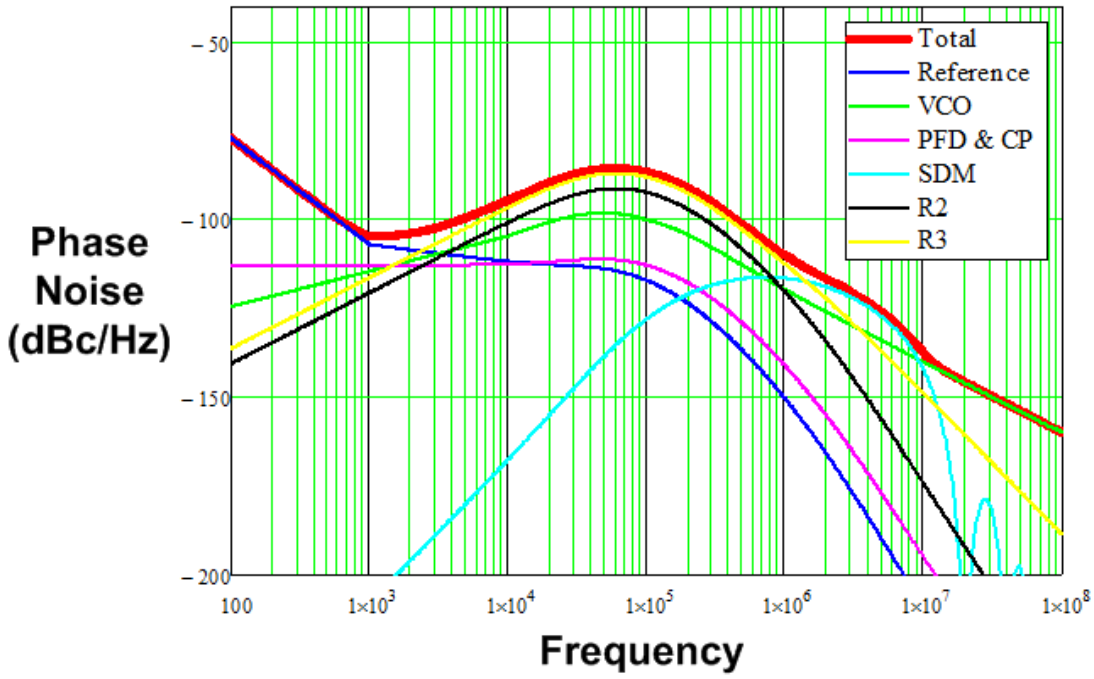

Figure 4.39: Phase noise contribution of all blocks in the PLL

Table 4.2: Design specifications

Symbol	Description	Value	Units
f_{ref}	reference clock frequency	20	MHz
I_{CP}	charge pump current	50	uA
K_{ϕ}	gain of PFD and charge pump	$\frac{I_{CP}}{2\pi}$	A/rad
K_{vco}	VCO gain	20	MHz/V
f_{out}	PLL output frequency	1600	MHz
N	divider ratio	80	none
γ	optimization parameter	1	none
T_{31}	ratio of T3 to T1	0.3	none
ϕ_M	desired phase margin	60	degrees
f_c	loop bandwidth	100	KHz

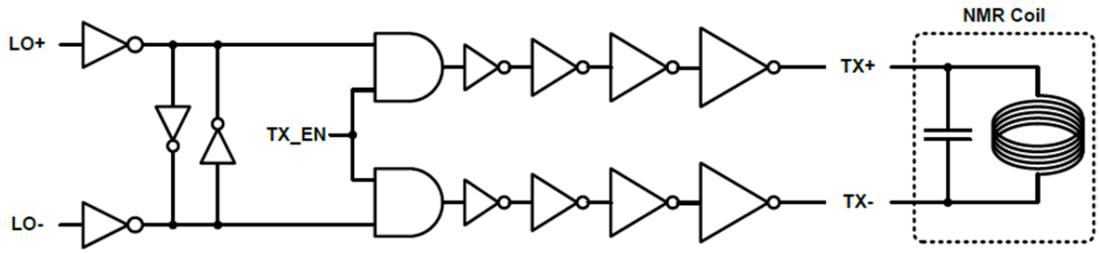

(a) Power amplier

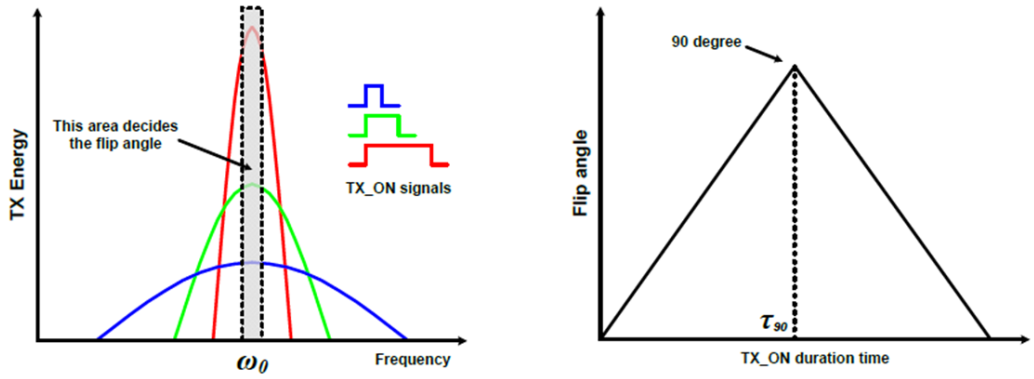

(a) Energy and flip angle versus on time duration

Figure 4.40: Power amplifier (a) and Energy and flip angle versus on time duration

4.5 Power Amplifier

For exciting the net magnetization of a sample, we need a power amplifier. Instead of a class A, B or AB design, a simple h-bridge type power amplifier using 4 inverters drives the NMR coil at resonance shown in Fig. 4.40 (a). It is fully differential to increase voltage swing and efficiency. Transmitting power is adjusted by controlling the on time duration even if a single power supply is provided. Energy that the NMR sample absorbs is the

sum of the gray area of the frequency response of the gated RF signal shown Fig. 4.40 (b). Also the flip angle is proportional to this energy. As we discussed, the phase noise of the frequency synthesizer is very critical to suppress a strong signal and detect NMR signals when there is huge magnitude ratio among them. For the complete NMR transceiver, the shimming function should be includued to reduce the inhomogeneity of magentic field (B_0). The shimming process needs additional coils and power amplifiers to drive them.

Chapter 5

Measurement Results

5.1 1^{st} and 2^{nd} NMR receivers

In the first and second NMR receivers, simple receiver circuits were implemented to check FID signals of phosphorus. Both receivers are the same except that the second has built in ADCs for digital signal processing. The Larmor frequency of Phosphorus is about 86MHz at 5T. A LNA-Mixer hybrid circuit provides a voltage gain of 24dB and down-converts the RF signal to an IF frequency. For generating LO signal for mixing, a simple integer-N type frequency synthesizer is chosen and a ring type VCO is used for low power. As a reference clock frequency, 1MHz is chosen for implantable applications. Measured phase noise at 100KHz offset is -86 dBc when the frequency synthesizer is locked at the phosphorus Larmor frequency. The first NMR receiver occupies 0.1 mm^2 and draws 650μA from 1.5V power supply. The second NMR receiver takes the area of 0.2 mm^2 due to additional 1-bit 2^{nd} order sigma delta ADC blocks and consumes 2.3mA

from a 1.5V power supply.

For the receiver test, we used the transmitter and the shimming function of a large commercial NMR system to maximize T_2^*. The test setup is shown in Fig. 5.1. To find the Larmor frequency and use the shimming function, external NMR system measures the sample first to get max a T_2^* with the right Larmor frequency then the receiver path is switched to our NMR receiver using a transmitter/receiver switch. The external receiver coil is matched to 50Ω. This creates signal voltage loss compared to the method we suggest passive multiplication. To compensate for this voltage loss, a preamplifier was used in front of our NMR receiver. With this help from the test setup, all receiver tests are completely done. The two NMR receivers designed are shown in Fig. 5.4.

In the first NMR receiver, we saw free-induction decay and the spectrum of a phosphorus signal (85% H_3PO_4) down-converted to 500Hz and also saw free-induction decay and the spectrum of α-, β- and γ- ATP from an ATP sample at 1KHz as shown in Fig. 5.2. T_2^* is about 6 ms and the closest distance among frequency peaks is about 500Hz. For obtaining an SNFR of 20dB, the frequency synthesizer works fine if the in-phase phase noise floor is smaller than -60dBc. The 1^{st} and 2^{nd} receivers have -86 dBc of in-band phase noise up to a 100KHz offset.

In the second NMR receiver, we just tested the ATP sample. Compared with the results from the 1^{st} receiver, the 2^{nd} shows better results because the internal ADC and LabVIEW® can save many data points and increase the FFT lengths. In the first NMR receiver, the number of data points was dependent on the memory size of DSO (digital

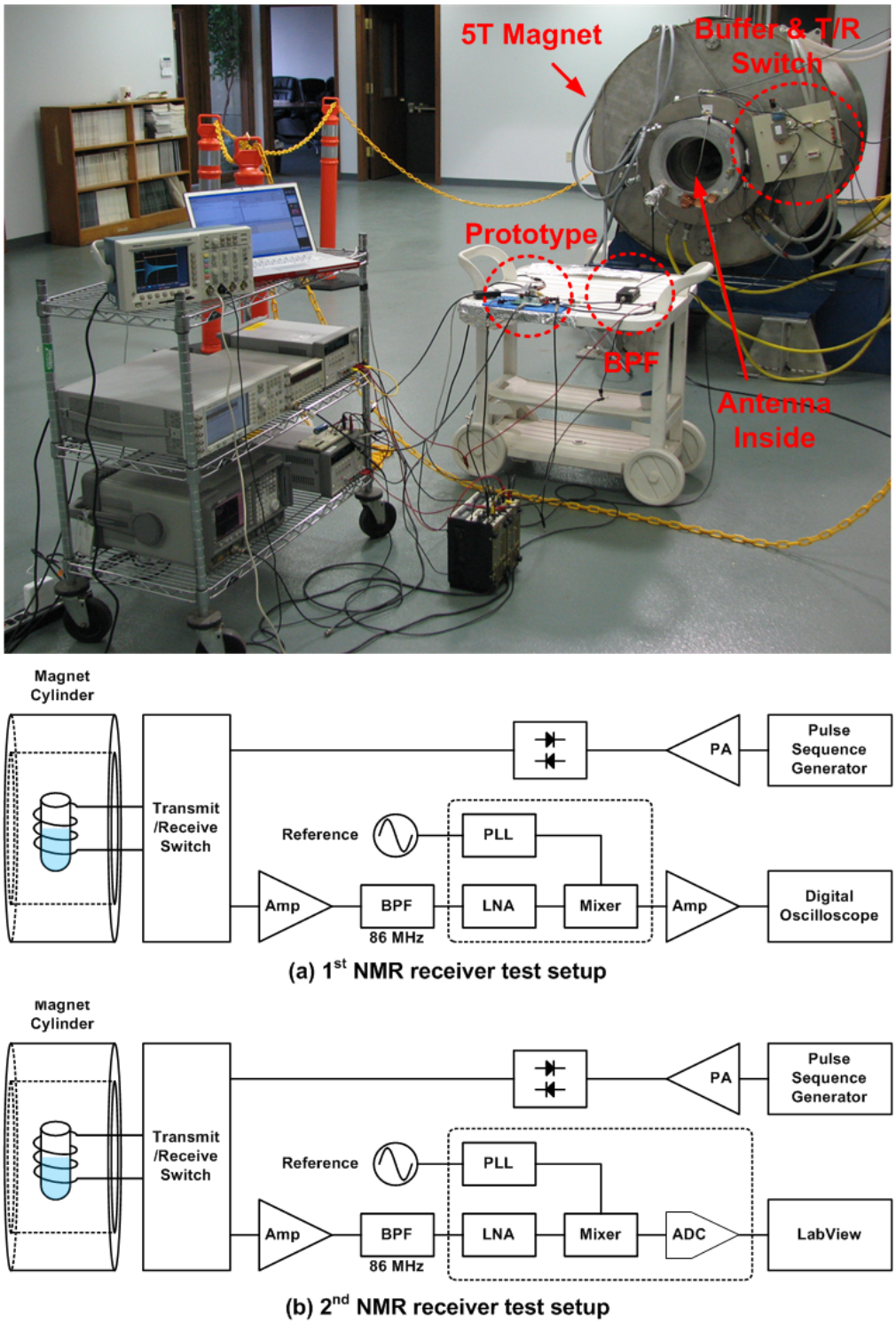

Figure 5.1: Test setup for 1^{st} and 2^{nd} NMR receivers

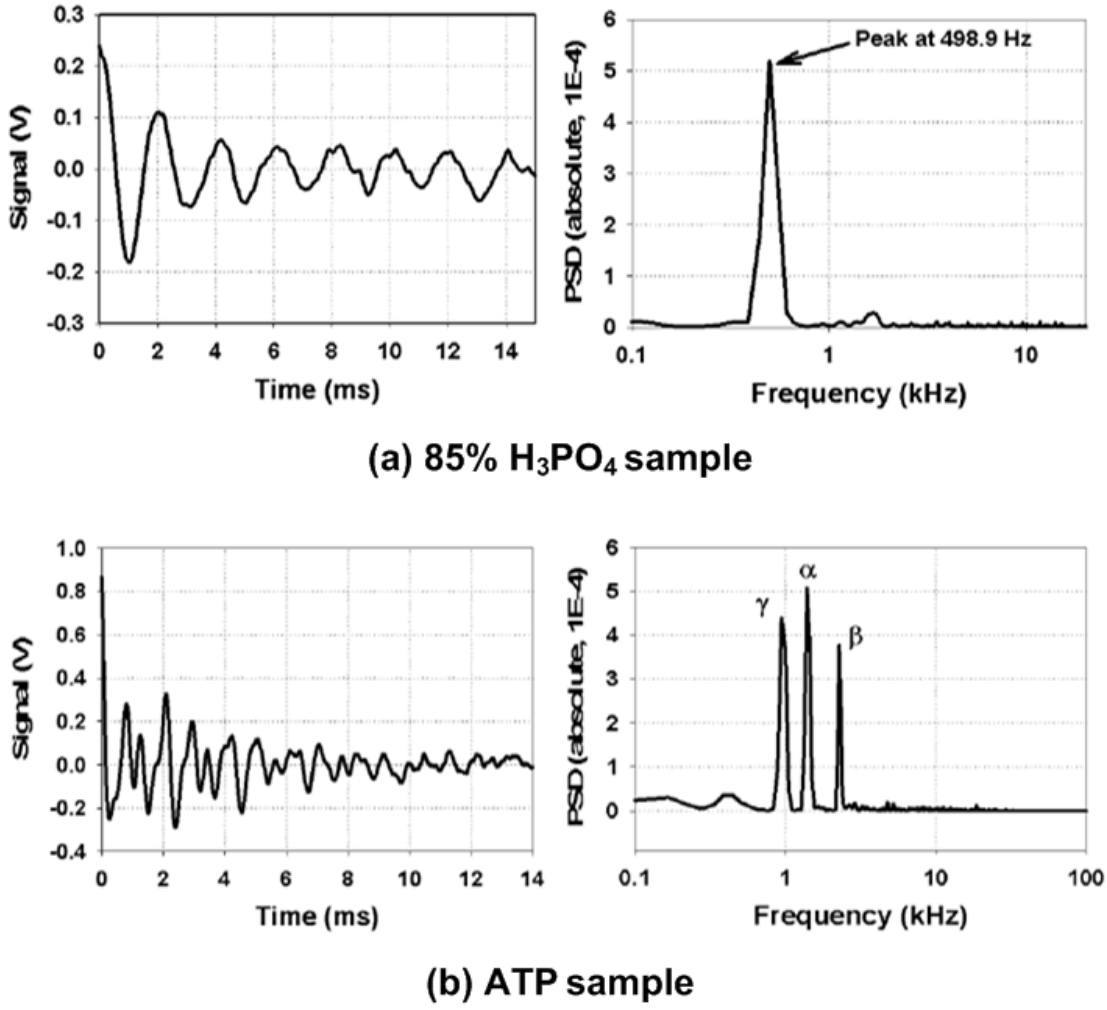

Figure 5.2: Measurement results from 1^{st} NMR receiver

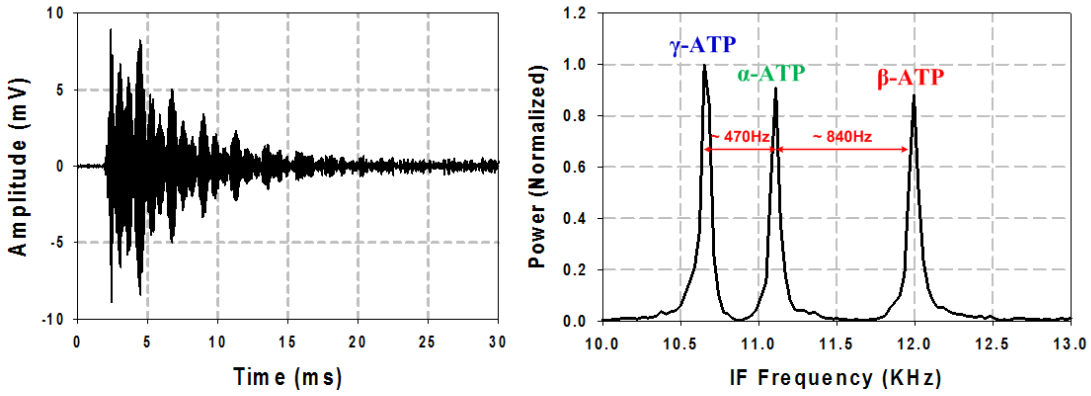

(a) 10mL 0.9 Molar ATP sample (at B_0 = 5T)

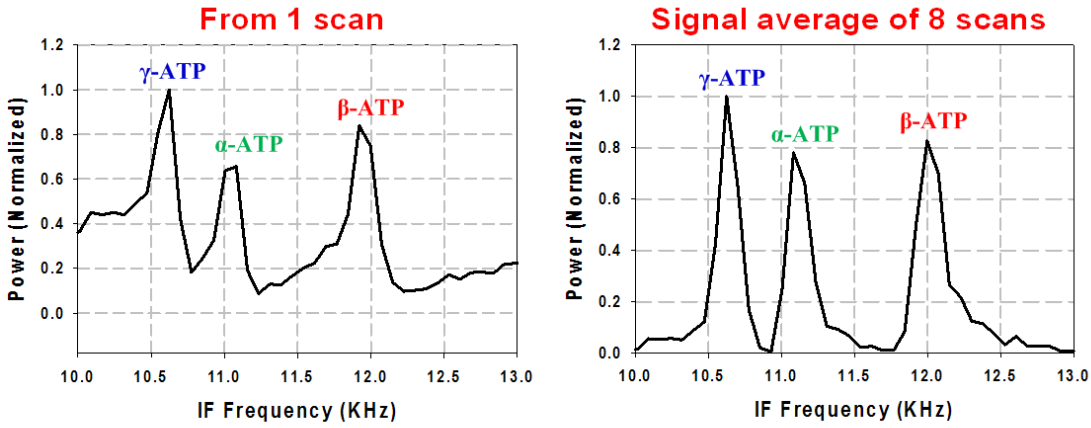

(b) 3mL 0.1 Molar ATP sample (at B_0 = 5T)

Figure 5.3: Measurement results from 2^{nd} NMR receiver

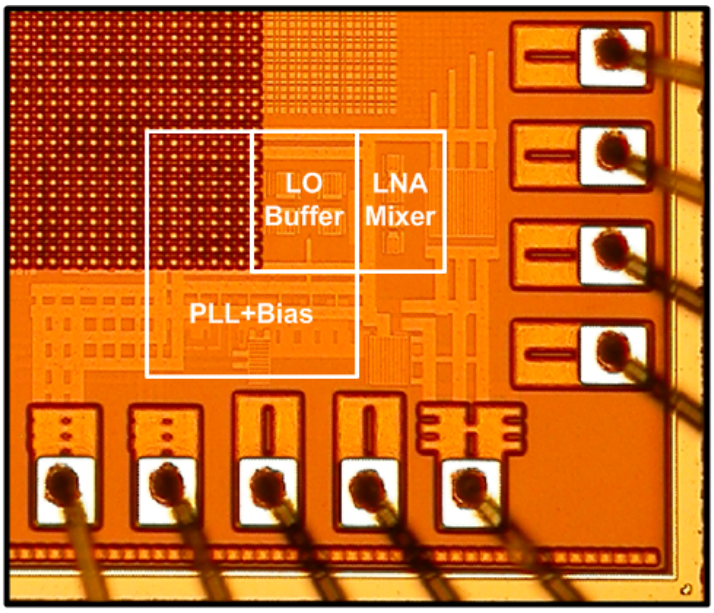

(a) 1st NMR receiver

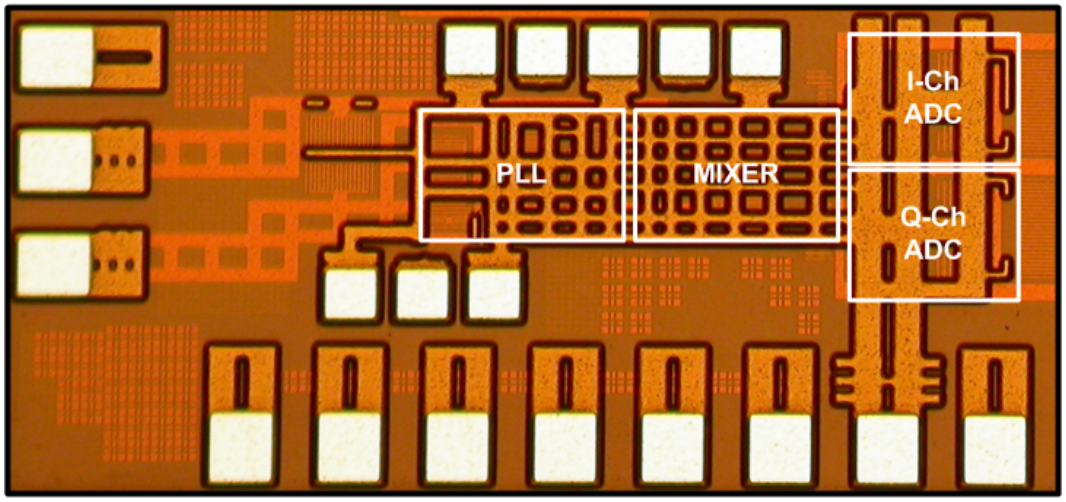

(b) 2nd NMR receiver

Figure 5.4: 1^{st} and 2^{nd} NMR receivers

oscilloscope). Fig. 5.3 (a) shows an FID signal and its spectrum from 10mL of 0.9 Molar ATP sample only in one-scan. Fig. 5.3 (b) shows the NMR spectrum from a low density sample (3mL 0.1 Molar ATP sample) where we can see their existence. However, a clearer spectrum is obtained through signal averaging from 8 scans. Traditional NMR systems sometimes use 1000 scan averages.

5.2 3^{rd} NMR transceiver

For testing the NMR transceiver, we verified the receiver functionality in advance. To check the receiver path including LNA, mixer, VGA and ADC, down conversion processing with a well-defined Larmor frequency according to the chemicals of interest from the frequency synthesizer should be confirmed first. To determine the values of resistors and capacitors in the loop filter for PLL, the VCO frequency is measured. In Fig. 5.6, the measured VCO frequency range is shown when fixed voltage (0.25V and 1.25V, where up and down currents of the charge pump are matched) is applied to the input of VCO. Each line covers a small frequency range according to value of the capacitor bank (64 unit capacitor cells) because it is difficult to cover the desired frequency range (1.5GHz $\sim$ 2.5GHz) and reduce the phase noise and spur level due to high K_{vco} if only one varactor is used without a capacitor bank. Also, to guarantee continuity within the frequency range, at least 3 curves are overlapped. The overall frequency range is 1.435GHz $\sim$ 2.686GHz and similar to the desired frequency range. The LC VCO oscillates at a higher frequency and the post modulus block shown in Fig. 4.25 divides the VCO fre-

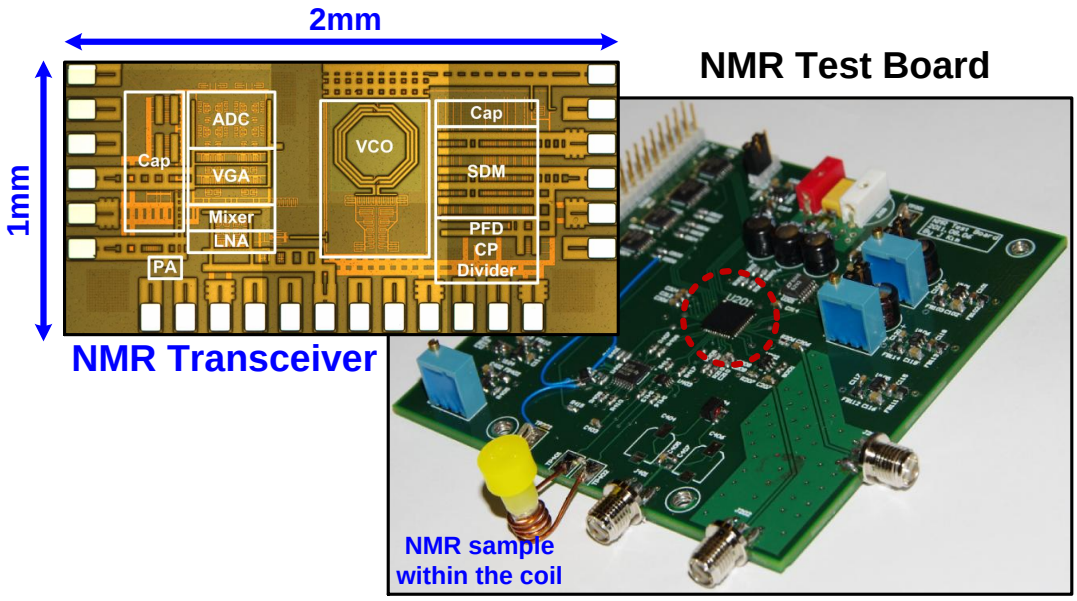

Figure 5.5: 3^{rd} NMR receiver and its testboard

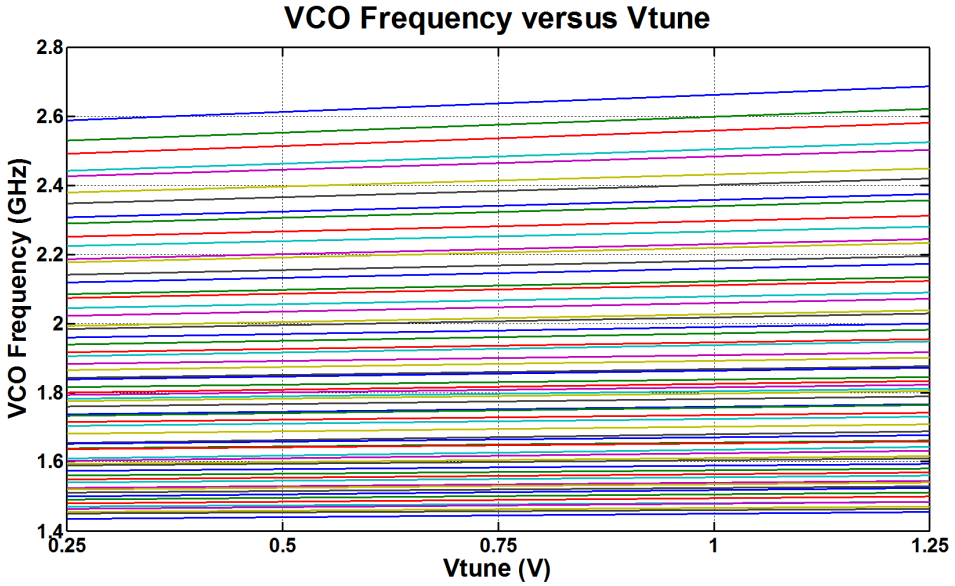

Figure 5.6: VCO Frequency versus Vtune

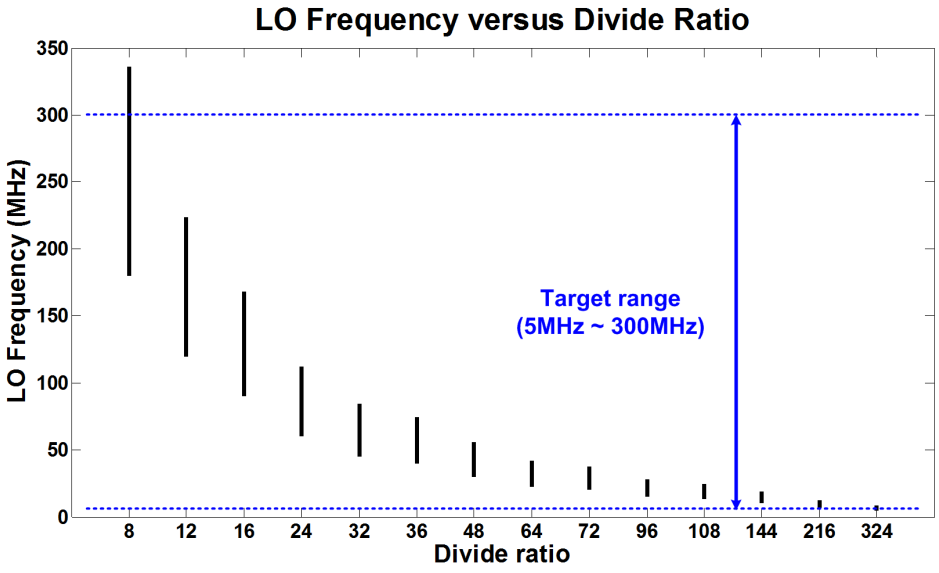

Figure 5.7: LO Frequency versus Divider Ratio

quency down to the Larmor frequency (as LO frequency) according to the chemicals of interest for B_0 between 0.5T and 5T. After divided in the post modulus block, the VCO signal is applied to another divider block (divider ratio =1/4) to generate I/Q signals. The final I/Q frequency range, for the mixer LO frequency, is 4.429MHz $\sim$ 335.8MHz and covers the desired range (5MHz $\sim$ 300MHz) shown in Fig. 5.7.

For PLL locking, we designed the loop filter based on the specifications listed in Table. 4.2. When the LO frequency is 5.45MHz (Larmor frequency of the carbon at 0.5T), the phase noise is reduced by the divider ratio of the post modulus according to the phase noise relationship even though the PLL is locked at higher frequency and has higher phase noise. For the worst case phase noise measurement, we locked the PLL at 1.7037GHz (equivalent to 212.966MHz $\times$ 8) because ^{1}H at 5T has its Larmor frequency

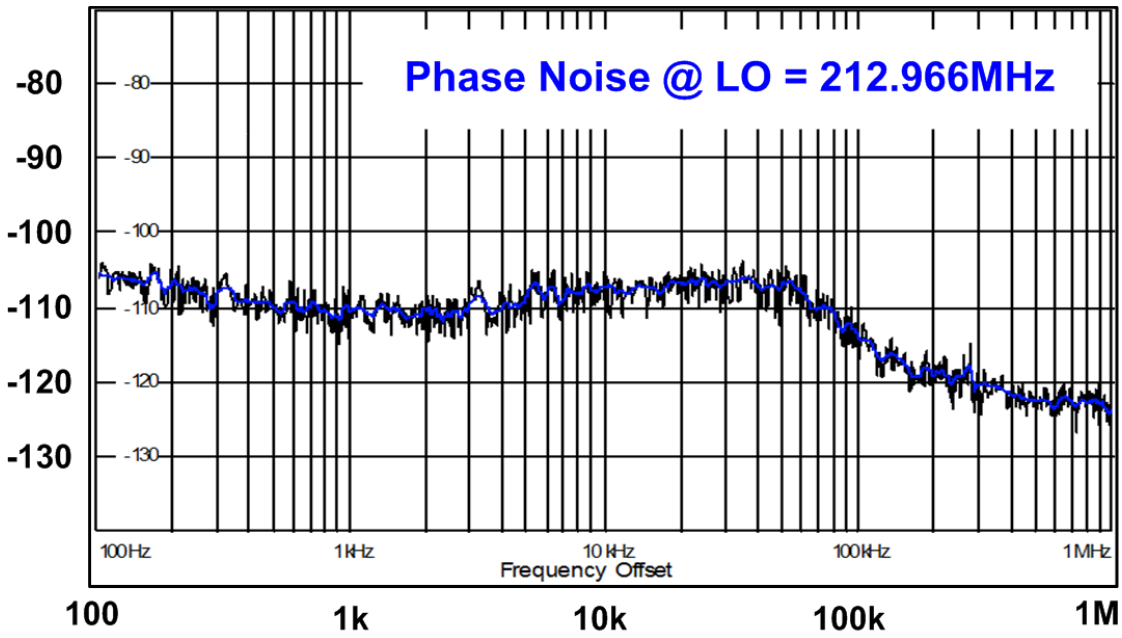

Figure 5.8: Phase noise at LO frequency = 212.966MHz

at 212.966MHz. The measured phase noise at 10KHz shown in Fig. 5.8 is $\sim$ -110dBc. At 5MHz, we can expect lower phase noise than at 212.966MHz, but the measured phase noise at 5MHz is similar to the phase noise at 220.966MHz. The reason for this that the measurable phase noise at lower frequencies is limited by the noise floor the frequency synthesizer used. Here we used a RODHE & SCHWARZ FSP $\cdot$ SPECTRUM ANALYZER $\cdot$ 9KHz $\sim$ 40GHz as the spectrum analyzer for measuring the phase noise for our NMR transceiver.

With this frequency synthesizer, the NMR receiver tests were performed on ^{1}H, ^{13}C and ^{31}P based samples only in a 5T magnet (because we do not have a 0.5T magnet but, it is enough to show the frequency synthesizer and dynamic range of the receiver)

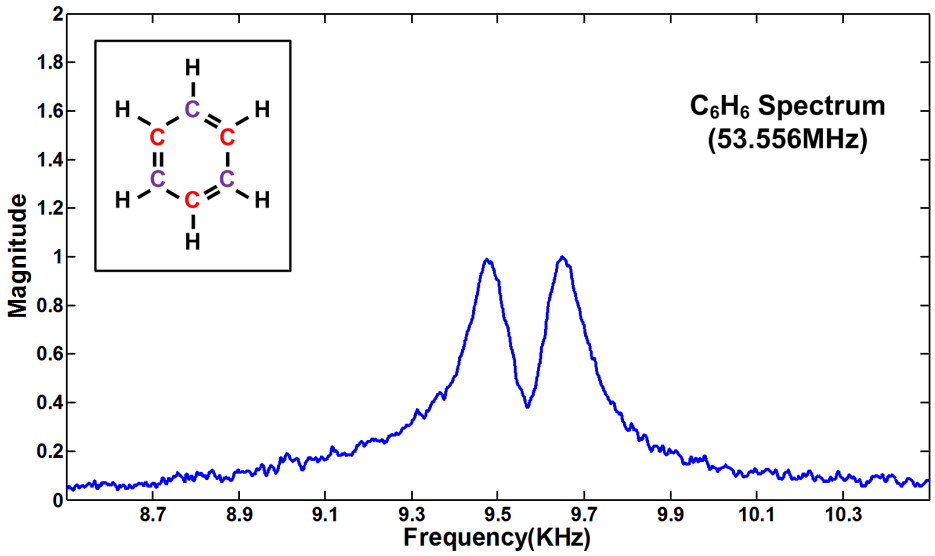

Figure 5.9: ^{13}C spectrum of Benzene (C_6H_6)

with the help of an external NMR coil. This 5T magnet is made by Tegmag Apollo®, Houston, TX.

According to the Larmor frequency, we tried carbon (^{13}C) based samples (2ml Benzene C_6H_6) first because carbon has the lowest frequency 53.566MHz. Fig. 5.9 shows ^{13}C NMR spectrum for the single-scan FID signal of benzene and two clear frequency peaks are distinguishable with the J-coupling ($J_{C-H} = 150$Hz).

Using an 1ml 0.1Molar Adenosine Tri-Phosphaste (ATP) sample based on phosphorus (^{31}P) having a Larmor frequency of 86.208MHz, the measured ^{31}P NMR spectrum is shown in Fig. 5.10. This spectum is also acquired from the FFT of a single-scan FID. The α-, β- and γ-ATP peaks are clearly shown with chemical shifts proportional to the magnetic field B_0 (around a few hundred Hz away each other at 5T).

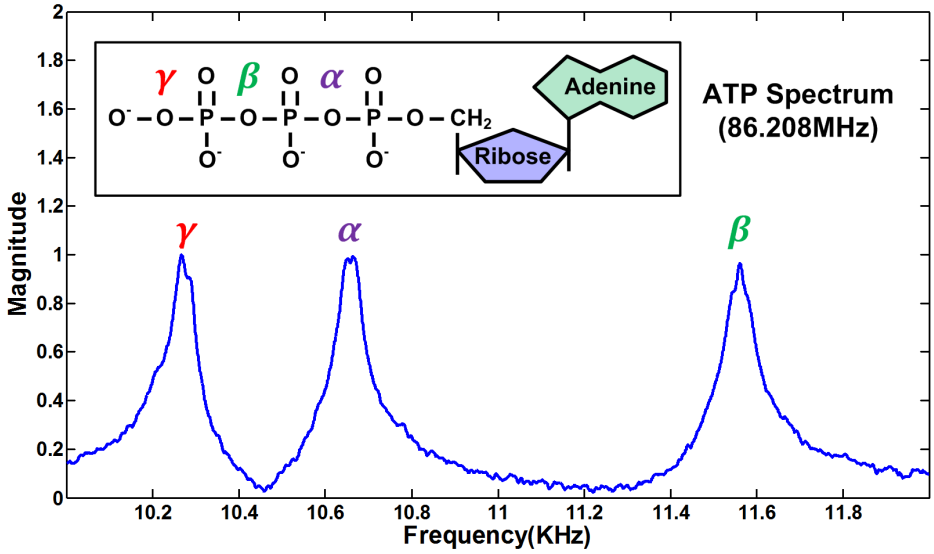

Figure 5.10: ^{31}P spectrum of Adenosine Tri-Phosphaste (ATP)

For our ^{1}H NMR spectrum test, 1.4ml Ethanol (CH_3CH_2OH) is used. Shown in Fig. 5.11, the Ethanol ^{1}H NMR spectrum is obtained from a single-scan FID as well. Zoomed-in spectra in Fig. 5.11, shows clearly the hydroxyl (OH), methylene (CH_2) and methyl (CH_3) groups that represents the scalar spin-spin coupling (J-coupling J_{H-H}) of approximately 7Hz. The excellent phase-noise of the on-chip frequency synthesizer allows for this fine spectrum resolution. Through the above tests with real NMR samples, the functionality of the receiver path is validated.

To test the function of the NMR transceiver, we chose a pure water (H_2O) sample. Unlike the conventional NMR systems, our NMR transceiver does not have the shimming function to compensate for the inhomogeneity of the magnetic field. Without shimming, the signal loss is unavoidable, but ^{1}H signal in the water is inherently high so it is good

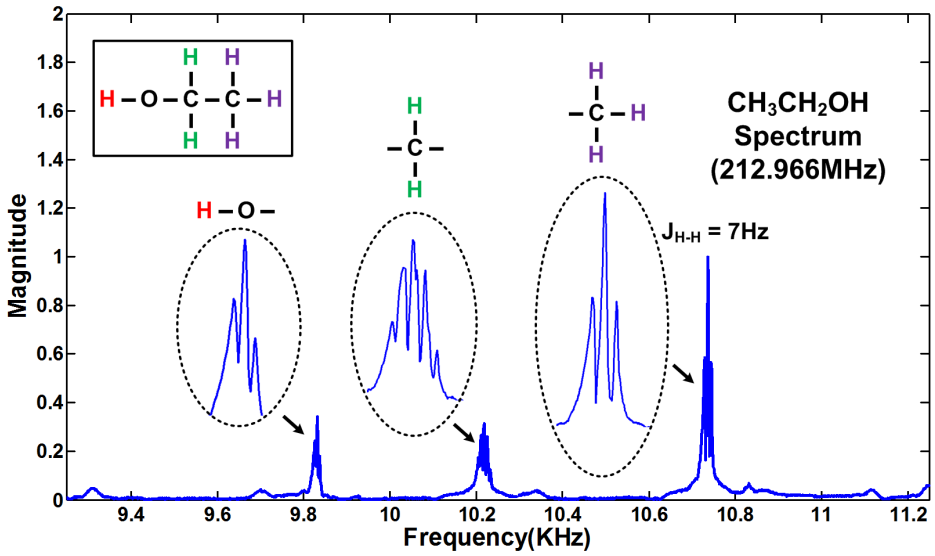

Figure 5.11: ^{1}H spectrum of Ethanol (CH_3CH_2OH)

for checking the function of the transceiver. Fig. 5.12 shows the FID signals from a 0.3ml H_2O sample after a 100us excitation pulse that is 3KHz away from the Larmor frequency using the internal TX power amplifier shown in Fig. 4.40 (a). This FID signal has a time constant (T_2^*) $\sim$ 1.5ms which is smaller (usually $\sim$100ms after shimming) due to no shimming process, but we are simply interested in the functionality of transmitter here. The full NMR transceiver functionality is verified from this test.

All tests including the receiver only and the transceiver show that it is possible to build a mini-size NMR spectrometer and MRI systems for sensing small objects and to expand to the implantable systems in the future.

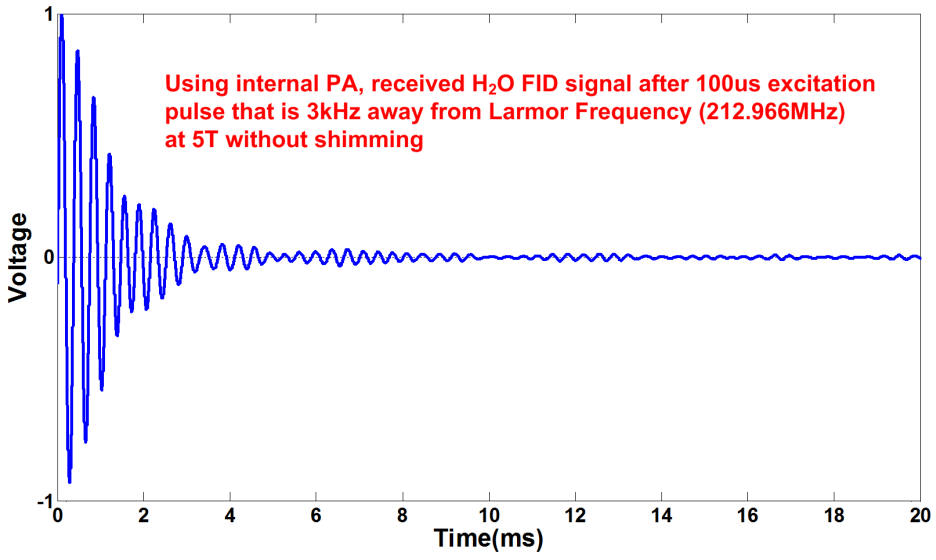

Figure 5.12: ^{1}H FID signal from the excitation of internal PA

Chapter 6

Conclusion and Future work

6.1 Conclusion

Through these works, we shows the feasibility of low power, low cost fully integrated CMOS NMR transceivers for the purpose of implantable and portable NMR applications (for example, high throughput drug discovery). Our final NMR transceiver, including a low noise amplifier (LNA), a double balanced quadrature mixer, an on chip fractional-N frequency synthesizer (PLL), a variable gain amplifier (VGA), a sigma delta analog-to-digital converter (ADC) and a power amplifier (PA), consumes 12 mA from a single 1.5V power supply and occupies an active area of 2 mm^2 in a 130nm IBM CMOS process. Direct digital synthesizers (DDS) are used in conventional NMR and MRI systems commonly for making arbitrary pulse waveforms. For example, AD9852 series made in Analog Devices are easily seen in NMR systems. In comparison with DDS based NMR systems, our NMR transceiver power consumption including transmitter and receiver

paths is 3 orders of magnitude smaller because AD9852 uses $\sim$ 500mA from 3.3V power supply. As shown in Table.2, our NMR transceiver has the highest integration and the best performance amongst prior works. The power is slightly higher than in our previous design (only receiver for phosphorus applications) [19] due to the low LNA noise and the use of an LC oscillator for lower phase noise in expense of the area. The additional power is justified by the higher sensitivity, excellent frequency selectivity and higher integration of the current design.

6.2 Future work

We understood fundamentals of NMR in Chapter. 2, considered the effects from T_2^* and the phase noise of frequency synthesizer in Chapter. 3, and designed the partially complete NMR transceiver in Chapter. 4. As seen through a range of measurement results in Chapter. 5, it is possible to design a complete implantable and portable mini NMR system. As a future work, we need to think of how to integrate and implement circuits for shimming additional coils to reduce inhomogeneity of B_0. Also we found the drawback of the Fourier Transform for FID NMR signal because it can hide its neighbors due to its Lorentzian if it is stronger than others. Carefully we suggest time domain analysis method to distinguish small neighbors even if a strong signal hides them.

Table 6.1: Comparison with prior works

	[32]	**[11]**	**[33]**	**[19]**	**This work**
Application	^{1}H	^{1}H	^{1}H	^{31}P	Multinuclei
Relaxometer Spectrometer	√ ·	√ ·	· √	· √	· √
Frequency (MHz)	21.3	250	300	86.2	5 ∼ 300
Transceiver Integration	TX+RX	TX+RX	RX	RX	TX+RX
PLL Integration	Yes	–	–	Yes	Yes
ADC Integration	–	–	–	Yes	Yes
Total Power (mW)	–	71.5	59.4	3.45	18
Area (mm^2)	3.8	0.9	1.02	0.215	2
Technology	180nm CMOS	120nm BiCMOS	350nm CMOS	130nm CMOS	130nm CMOS

Bibliography

[1] B.E. Boser and B.A. Wooley, "The design of sigma-delta modulation analog-to-digital converters," *IEEE JSSC*, December 1988.

[2] Juan Perlo, Vasiliki Demas, Federico Casanova, Carlos A. Meriles, Jeffrey Reimer, and Alexander Pinesand Bernhard Blmich, "High-Resolution NMR Spectroscopy with a Portable Single-Sided Sensor," *Sicence*, p. 1279, 2005.

[3] Perlo J, Casanova F, and Blmich B, "3D imaging with a single-sided sensor: an open tomograph," *Journal of Magnetic Resonance*, pp. 228–235, 2004.

[4] Andrew Webb, *Introduction to Biomedical Imaging*, Jon Wiley and Sons, Inc.

[5] D.I Hoult and R.E.Richards, "The Signal-to-Noise Ratio of the Nuclear Magnetic Resonance Experiment," *Journal of Magnetic Resonance*, pp. 71–85, 1976.

[6] D.I Hoult and Paul C. Lauterbur, "The Sensitivity of the Zeugmatographic Experiment Involving Human Samples," *Journal of Magnetic Resonance*, pp. 425–433, 1979.

[7] Thomas W Redpath and Christopher J Wiggins, "Estimating achievable signal-to-noise ratios of MRI transmit-receive coils from radiofrequency power measurements: applications in quality control," *Physics in Medicine and Biology*, pp. 217–227, 2000.

[8] T.L. Peck, R.L. Magin, and P.C. Lauterbur, "Design and Analysis of Microcoils for NMR Microscopy," *Journal of Magnetic Resonance*, pp. 114–124, 1995.

[9] A.Abragam, *The Principles of Nuclear Magnetism*, Claren Press.

[10] Robin A. De Graaf, *In Vivo NMR Spectroscopy*, Jon Wiley and Sons, Ltd.

[11] Yong Liu, Nan Sun, R. Weissleder, and Donhee Ham, "CMOS Mini Nuclear Magnetic Resonance System and its Application for Biomolecular Sensing," *IEEE ISSCC*, pp. 140–141, February 2008.

[12] Nan Sun, Yong Liu, R. Hakho Lee andWeissleder, and Donhee Ham, "CMOS RF Biosensor Utilizing Nuclear Magnetic Resoanance," *IEEE JSSC*, pp. 1629–1643, May 2009.

[13] P.J Hore, "Solvent Suppression in Fourier Transform Nuclear Magnetic Resonance," *Journal of Magnetic Resonance*, pp. 283–300, 1983.

[14] Z. Starcuk., Z. Starcuka, V. Mlynarikb, M. Rodenc, J. Horki, and E. Moser, "Low-Power Water Suppression by Hyperbolic Secant Pulses with Controlled Offsets and Delays (WASHCODE)," *Journal of Magnetic Resonance*, pp. 168–178, 2001.

[15] Pierre Plateau and Maurice Gueronr, "Exchangeable proton NMR without base-line distorsion, using new strong-pulse sequences," *Journal of the American Chemical Society*, pp. 7310–7311, 1982.

[16] A.S. Altieri and R.A. Byrd, "Randomization Approach to Water Suppression in Multidimensional NMR Using Pulsed Field Gradients," *Journal of Magnetic Resonance*, pp. 260–266, 1995.

[17] R. Olsson and K. Wise, "A Three-Dimensional Neural Recording Microsystem With Implantable Data Compression Circuitry," *IEEE ISSCC Digest of Technical Papers*, pp. 558–559, February 2005.

[18] S. O'Driscoll, A. S. Y. Poon, and T. H. Meng, "A mm-Sized Implantable Power Receiver with Adaptive Link Compensation," *IEEE ISSCC Digest of Technical Papers*, pp. 294–295, February 2009.

[19] Jaehyup Kim, Bruce Hammer, and Ramesh Harjani, "A Low Power CMOS Receiver for a Tissue Monitoring NMR Spectrometer," *IEEE VLSI*, June 2010.

[20] Jackson Harvey and Ramesh Harjani, "Analysis and Design of an Integrated Quadrature Mixer with Improved Noise, Gain, and Imgae Rejection," *IEEE ISCAS*, pp. 786–789, 2001.

[21] Leonard A. MacEachern and Tajinder Manku, "A Charge-Injection Method for Gilbert Cell Biasing," *IEEE Canadian Conference on Electrical and Computer Engineering*, pp. 365–368, 1998.

[22] S.-G.Lee and J.-K.Choi, "Current-Reuse Bleeding Mixer," *Electronic Letter*, pp. 696–697, 2000.

[23] Keng Leong Fong and Robert G. Meyer, "Monolithic RF Active Mixer Design," *IEEE Transactions on Circuits and Systems*, pp. 231–239, March 1999.

[24] Hooman Darabi and A. Abidi, "Noise in RF-CMOS Mixers : A Simple Physical Model," *IEEE JSSC*, pp. 15–25, January 2000.

[25] A Sripad and D Snyder, "A Necessary and Sufficient Condition for Quantization Errors to be Uniform and White," *IEEE Transactions on Acoustics Speech and Signal Processing*, pp. 442–448, 1977.

[26] D. Leeson, "A Simple Model of Feedback Oscillator Noise Spectrum," *Proceedings of IEEE*, pp. 329–330, 1966.

[27] Ali Hajimiri and Thomas H. Lee, "A General Theory of Phase Noise in Electrical Oscillators," *IEEE JSSC*, pp. 179–194, February 1998.

[28] Ali Hajimiri, Sotirios Limotyrakis, and Thomas H. Lee, "Jitter and Phase Noise in Ring Oscillators," *IEEE JSSC*, pp. 790–804, June 1999.

[29] Behzad Razavi, "A Study of Phase Noise in CMOS Oscillators," *IEEE JSSC*, pp. 331–343, March 1996.

[30] Woogeun Rhee, Bang-Sup Song, and Akbar Ali, "A 1.1-GHz CMOS Fractional-N Frequency Synthesizer with a 3-b Third-Order Modulator," *IEEE JSSCC*, pp. 1453–1460, 2000.

[31] Tom A. D. Riley, Miles A. Copeland, and Tad A. Kwasniewski, "Delta-Sigma Modulation in Fractional-N Frequency Synthesis," *IEEE JSSCC*, pp. 553–559, 1993.

[32] Arjang Hassibi, Aydin Babakhani, and Ali Hajimiri, "A Spectral-Scanning Nuclear Magnetic Resonance Imaging (MRI) Transceiver," *IEEE JSSC*, pp. 1805–1813, June 2009.

[33] J. Anders, P. SanGiorgio, and G. Boero, "An Integrated CMOS Receiver Chip for NMR-Applications," *IEEE CICC*, pp. 471–474, 2009.